UC Berkeley
UC Berkeley Electronic Theses and Dissertations

Title
Structural and Functional Characterization of the Proteasomal Deubiquitinase Rpn11

Permalink
https://escholarship.org/uc/item/2138s3gn

Author
Worden, Evan Josiah

Publication Date
2016

Peer reviewed|Thesis/dissertation

eScholarship.org Powered by the California Digital Library
University of California

Structural and Functional Characterization of the Proteasomal Deubiquitinase Rpn11

By

Evan Josiah Worden

A dissertation submitted in partial satisfaction of the

requirements for the degree of

Doctor of Philosophy

in

Molecular and Cell Biology

in the

Graduate Division

of the

University of California, Berkeley

Committee in charge:

Professor Andreas Martin, Chair
Professor Susan Marqusee
Professor Eva Nogales
Professor David Wemmer

Summer 2016

Abstract

Structural and Functional Characterization of the Proteasomal Deubiquitinase Rpn11

by

Evan Josiah Worden

Doctor of Philosophy in Molecular and Cell Biology

University of California, Berkeley

Professor Andreas Martin, Chair

The 26S proteasome is responsible for selective protein degradation in eukaryotic cells. Polyubiquitin chains mark proteins for degradation by the proteasome, but before degradation can occur, ubiquitin chains must be removed by the intrinsic proteasomal deubiquitinase Rpn11. My graduate work primarily focused on understanding how Rpn11 is regulated so it only removes ubiquitin chains from substrates that have been committed to degradation. To answer this question, I developed an Rpn11 purification strategy and solved the crystal structure of Rpn11 alone and in complex with ubiquitin. These structures revealed several features that control the activity of Rpn11 toward ubiquitin substrates. I showed that Rpn11 is promiscuous in its activity toward different ubiquitin substrates, which explained how the enzyme is able to remove ubiquitin molecules from the wide range of proteasome substrate proteins. Comparison of our ubiquitin-bound and ubiquitin-free structures revealed that a critical loop changes conformation when ubiquitin binds to Rpn11 to form a catalytically active state and that substrate translocation may accelerate this transition, thereby activating the enzyme.

Rpn11 is part of a proteasome sub-complex called the lid. In the isolated lid Rpn11 is inhibited to reduce off pathway deubiquitination prior to proteasome assembly, but the mechanism of Rpn11 inhibition in the lid was not understood. We used cryo-EM to determine the atomic structure of the isolated lid which explained how Rpn11 is inhibited and how it becomes activated when incorporated into the proteasome. Our structure revealed that Rpn11 is held in a conformation that fully occludes its active site and prevents the enzyme from accessing ubiquitin substrates. Mutagenesis of inhibitory residues in the lid release Rpn11 from its inhibited state and activate the enzyme. Similarly, when the lid incorporates into the proteasome, Rpn11 is released from its inhibited state and adopts a fully extended, open conformation seen in the 26S proteasome.

Table of contents

Table of figures

1. Introduction

1.1 Selective degradation of proteins maintains the proteome

The end product of gene expression is the synthesis of protein. Proteins are the primary molecular effectors of life and have many diverse functions in the cell including the catalysis of nearly all biochemical reactions, transduction and propagation cellular signals, cell motility, gene expression, the physical organization of genomic material and DNA replication. Due to the central role proteins play in every aspect of cellular life, it is vital that the cell maintains a healthy proteome. However, proper proteome maintenance is a complicated task because many proteins are only needed for a very brief period in the life of a cell and can be detrimental to the cell if they persist beyond their useful lifespan. Additionally, when proteins become damaged or misfolded they can aggregate, forming inclusions within the cell. These protein aggregates are toxic to the cell, alter cell physiology are thought to be a causative factor in several human neurodegenerative diseases(Ross & Poirier 2004). To get around these problems, life has developed intricate systems for the targeted removal of proteins from the cell through selective degradation. In eukaryotes, this system of selective protein degradation is called the Ubiquitin Proteasome System (UPS).

1.2 The ubiquitin proteasome system regulates protein turnover

The first step in targeted protein degradation is selecting the protein to be degraded. In eukaryotic cells this is accomplished through the covalent modification of condemned proteins with a small protein molecule called ubiquitin in a process termed ubiquitination. I will focus first on the mechanism of ubiquitination and how proteins become fated for degradation by the 26S proteasome.

1.2.1 Mechanism of protein ubiquitination

Ubiquitin is a small, 76 amino acid protein that is conserved across all eukaryotic life. In the process of ubiquitination, the C terminus of ubiquitin becomes covalently attached to the ε-amino group of a lysine residue on a substrate protein (Pickart 2001). The resulting amide bond is referred to as an isopeptide bond due to its chemical similarity to the peptide bonds which link amino acids together in a protein (Hershko et al. 1980; Asquith et al. 1974). The process of ubiquitination can be subdivided into three biochemical reactions that are carried out sequentially by E1, E2 and E3 enzymes (Figure 1.1). In the first (and only ATP-dependent) reaction an activating (E1) enzyme hydrolyzes ATP and forms a covalent thioester linkage between the C terminus of a ubiquitin molecule and a cysteine in the enzyme's active site. In the second reaction the E1 transfers its covalently attached ubiquitin to a conjugating (E2) enzyme, which itself forms a thioester linkage with the C terminus of the activated ubiquitin. Finally, the E2 binds to a ubiquitin ligase (E3) which facilitates (either directly or indirectly) the covalent attachment of ubiquitin from the E2 to the ε-amino group of a lysine residue on a substrate protein.

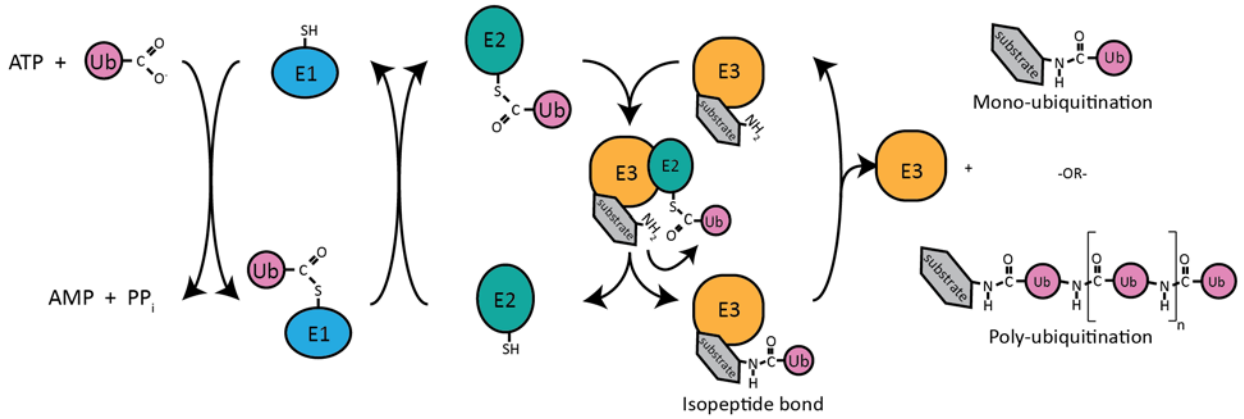

Figure 1.1: Mechanism of ubiquitination
The enzymatic cascade responsible for protein ubiquitination is diagramed above. In the first step, E1 reacts with ATP and mono-ubiquitin to form AMP, pyrophosphate and a covalent E1-ubiquitin complex linked though a thioester between the C-terminus of ubiquitin and a cysteine in the E1 active site. In the second step, the E1 passes the activated ubiquitin to an E2 enzyme which also forms a covalent E2-ubiquitin complex linked though a thioester. In the final step of ubiquitination, the E2-ubiqutin complex binds to an E3/substrate complex which positions a lysine on the substrate to attack the activated E2-ubiquitin complex. This reaction forms an isopeptide linkage between the C-terminus of ubiquitin and a lysine on the substrate protein.

Ubiquitination can occur either non-processively or processively. In non-processive ubiquitination a lysine on the substrate protein becomes covalently modified with a single ubiquitin, a process termed mono-ubiquitination. Mono-ubiquitination is the simplest type of ubiquitin modification and is important for various signaling pathways including DNA repair and endocytosis (Hicke 2001; Sadowski et al. 2012; Komander & Rape 2012). In processive ubiquitination a lysine residue on a substrate-conjugated ubiquitin is used to attach another ubiquitin molecule. This can occur multiple times to produce polymeric ubiquitin chains of different linkage types that are characterized by the specific lysine used to connect the ubiquitin molecules in the chain (Komander & Rape 2012). These chains can be relatively short and contain only 2 ubiquitin molecules, or be very long with 10 or more ubiquitin molecules present in a single chain. Because ubiquitin has seven lysine residues and an N terminus that can accept ubiquitin modifications, a total of eight distinct ubiquitin chain types can be produced by polyubiquitination.

1.2.2 Deubiquitinases reverse ubiquitination

The isopeptide linkages formed during ubiquitination can be severed by enzymes called deubiquitinases (DUBs). The human genome contains about 83 DUBs which are divided into 5 families: ubiquitin-specific hydrolases (UCH), ubiquitin-specific proteases (UBP), ovarian tumor proteases (OTU), MIU-containing novel DUB family (MINDY), josephin DUBs and JAB1/MPN/MOV34 (JAMM) metalloenzymes (Komander et al. 2009; Arif et al. 2016) (Figure1.2A). UCH, UBP, OTU, MINDY and josephin deubiquitinases are cysteine proteases that share an active-site geometry and catalytic mechanism with the canonical cysteine protease papain. The JAMM family of DUBs, however, are metalloproteases that

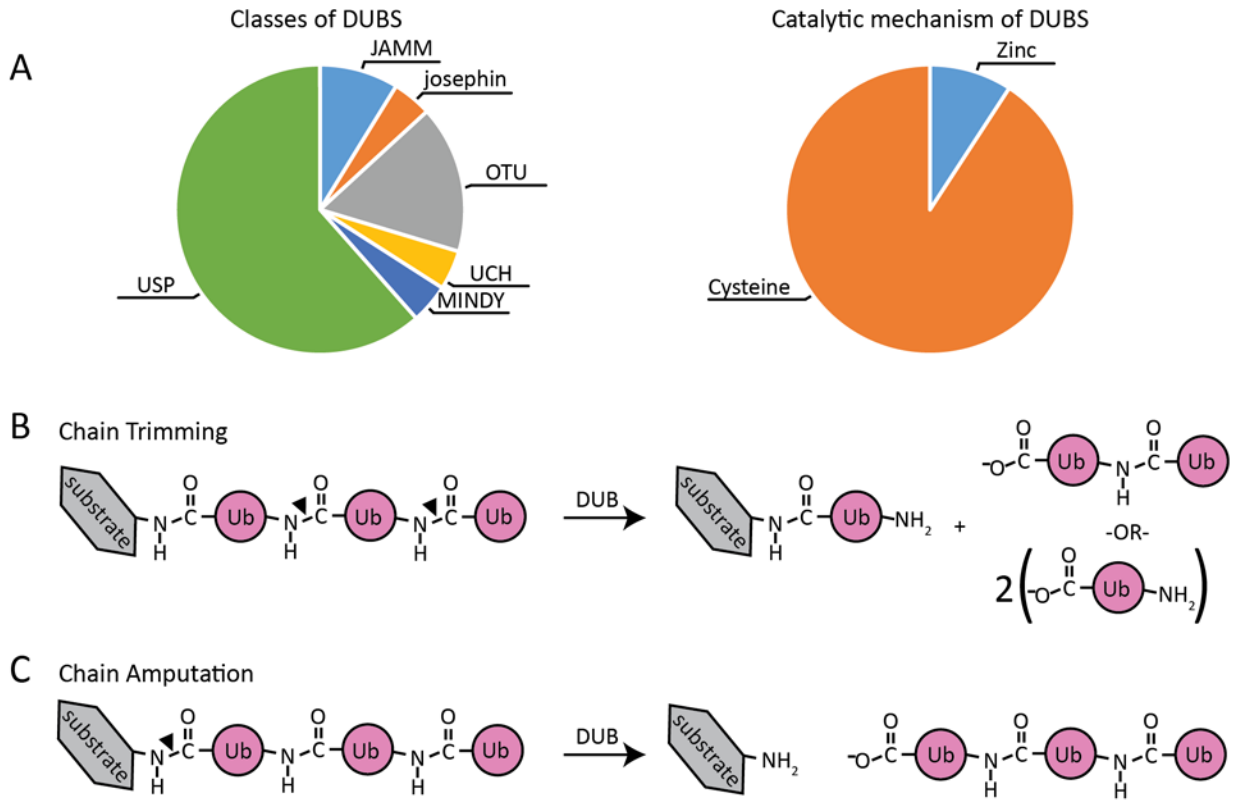

Figure 1.2: Deubiquitination
(**A**) All human deubiquitinases are depicted as a pie chart according to their respective families (left) or the catalytic mechanism employed for isopeptide bond cleavage (right). (**B**) The chain trimming activity of DUBs requires that the enzyme cuts in between ubiquitin molecules. The end product of a DUB that exhibits chain trimming activity is either short ubiquitin chains or mono-ubiquitin. (**C**) DUBs that have chain amputation activity cut between a substrate protein and the first ubiquitin in a chain and produce un-ubiquitinated substrate and free ubiquitin chains.

utilize a Zn^{2+} cofactor for isopeptide bond cleavage in a mechanism shared with the zinc-dependent protease thermolysin (Sato et al. 2008).

DUBs oppose protein ubiquitination and catalyze isopeptide bond hydrolysis in one of two ways. Firstly, many DUBs cut isopeptide linkages between ubiquitin molecules in a chain which produces shorter ubiquitin chains or mono-ubiquitin (Figure 1.2B). Cutting within a chain is thought to attenuate ubiquitin signaling by shortening the length of a substrate-attached ubiquitin chain. However, DUBs that act in this manner can also exhibit chain editing activities where ubiquitin chain shortening then allows for a new chain of a different linkage type to be built. This chain-editing activity is exemplified by the OTU DUB A20 which removes lys63-liked ubiquitin chains and replaces them with lys48-linked chains (Wertz et al. 2004). Secondly, DUBs can cleave between ubiquitin and a substrate protein, producing un-ubiquitinated protein and a free ubiquitin or ubiquitin chain (Figure 1.2C). This chain amputation activity results in complete reversal of the ubiquitin signal and is typically utilized only after a signaling event has concluded or committed the ubiquitin-attached protein to some downstream fate.

1.2.3 Polyubiquitin signals are decoded by ubiquitin binding domains

An important consequence of polyubiquitination is that ubiquitin chains linked through different lysine residues adopt distinct 3-dimentional topologies. The structural differences between ubiquitin chain types allow ubiquitin-binding domains (UBDs) to discriminate between the different ubiquitin linkages and make UBDs specific for their corresponding chain type (Komander & Rape 2012; Ikeda et al. 2010). These UBDs decode information stored in the 3-dimentional structure of a ubiquitin chain and elicit some function through their interaction with the ubiquitin chain. For instance, many DUBs are recruited to specific ubiquitin chain types via UBDs in their primary sequences, making the DUB specific for the linkage encoded in its UBD (Komander et al. 2009). So far at least 200 UBD-containing proteins have been identified (Ikeda et al. 2010; Dikic et al. 2009) which allow the cell to ascribe broad functions to different chain types. In short, ubiquitin chains linked through ubiquitin's N terminus, Lys6, Lys27, Lys29, Lys33 or Lys63 are used for non-degradative signaling processes, while proteins attached to ubiquitin chains linked though Lys11 or Lys48 are destined for destruction by the 26S proteasome.

1.3 Structure of the 26S proteasome

The 26S proteasome is a very large (2.5MDa), highly complex molecular machine responsible for the ATP-dependent degradation of proteins marked with Lys11 or Lys48 polyubiquitin chains. The minimal assembly of the 26S proteasome contains 33 distinct proteins, including 6 ATPases, 3 proteases and 1 deubiquitinase (Figure 1.3A, Table 1.1). The proteasome can be biochemically and structurally divided into 2 main sub-complexes: the core particle (CP) and regulatory particle (Finley 2009). The core particle is composed of four stacked heptameric rings that form an axially gated, proteolytic chamber responsible for the protein degradation activity of the proteasome. The regulatory particle associates with the CP by binding to one or both of CP's apical surfaces and thus controls access of protein substrates to the core particle's central proteolytic chamber. The regulatory particle itself can be subdivided into two more sub-complexes termed base and lid. The base is a protein unfoldase and contains 6 distinct AAA+ (*A*TPases *a*ssociated with cellular *a*ctivities) ATPases, 2 large scaffolding protein and 2 intrinsic ubiquitin receptors. The lid contains the essential deubiquitinase of the proteasome, a third intrinsic ubiquitin receptor and 8 scaffolding subunits.

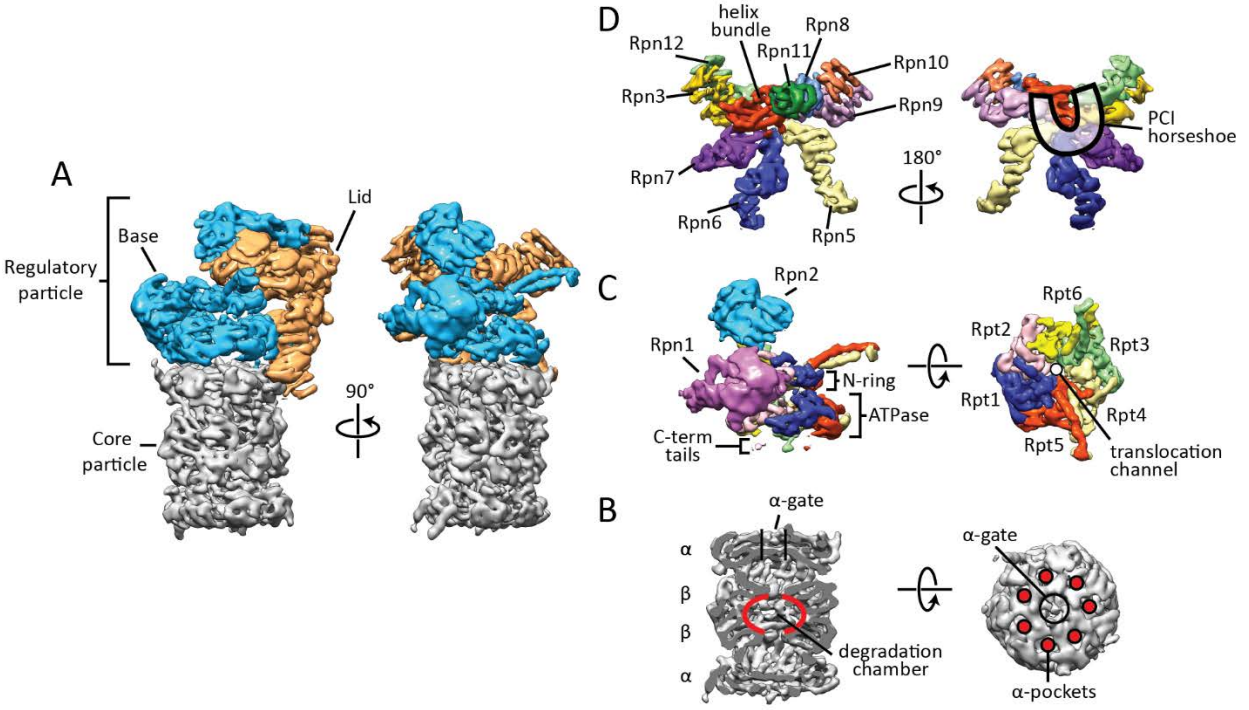

Figure 1.3: Molecular architecture of the 26S proteasome
(**A**) Cryo-electron microscopy reconstruction of the yeast 26S proteasome actively degrading substrate EMD:5669 (Matyskiela et al. 2013). Core particle, base and lid are colored gray, blue and tan respectively. (**B**) Core particle is depicted in cutaway (left) and from the top (right) to emphasize the α- and β-rings, central degradation chamber, α-gate and α-pockets. (**C**) Individual subunits of the base are shown segmented and colored for clarity. The C-terminal tails, AAA+ ATPase ring and N-ring are clearly visible (left). The base seen from the top with Rpn1 and Rpn2 removed (right) shows the hexameric nature of the motor and the central translocation channel formed from the ATPase domains and N-ring. (**D**) The lid was segmented and colored as in C. The lid viewed from the front (left) clearly shows the C-terminal helix bundle formed from the C-termini of each lid subunit (red) and the Rpn11-Rpn8 MPN dimer (green and blue, respectively). From the back of the lid (right) the PCI-domain horseshoe is highlighted and the TPRs of Rpn3, 5, 6, 7, 9, and 12 can be seen projecting out from the center of the complex like fingers.

1.3.1 The core particle

The core particle is assembled out of four stacked α and β heptameric rings in the arrangement $\alpha_{1\text{-}7}$-$\beta_{1\text{-}7}$- $\beta_{1\text{-}7}$-$\alpha_{1\text{-}7}$ (Figure 1.3B). Three of the β subunits (β1, β2, and β5) contain a threonine-dependent proteolytic active site oriented toward the central protein degradation camber (Groll et al. 1997). Each of the three catalytic β-subunits is classified by its broad activity where β1 exhibits caspase-like, β2 exhibits trypsin-like and β5 exhibits chymotrypsin-like cleavage specificity (Finley 2009). Because the β-subunit active sites face the interior of the core particle, their activity is limited to polypeptides which can gain access to the degradation chamber. Substrate access to the interior of the core is regulated by the α-subunits. The N termini of each α-subunit coalesce to form an axial "α-gate" that blocks the central channel leading into the proteolytic chamber and thereby controls access of substrates into the core particle(Groll et al. 2000; Groll et al. 1997). Additionally, the α-ring

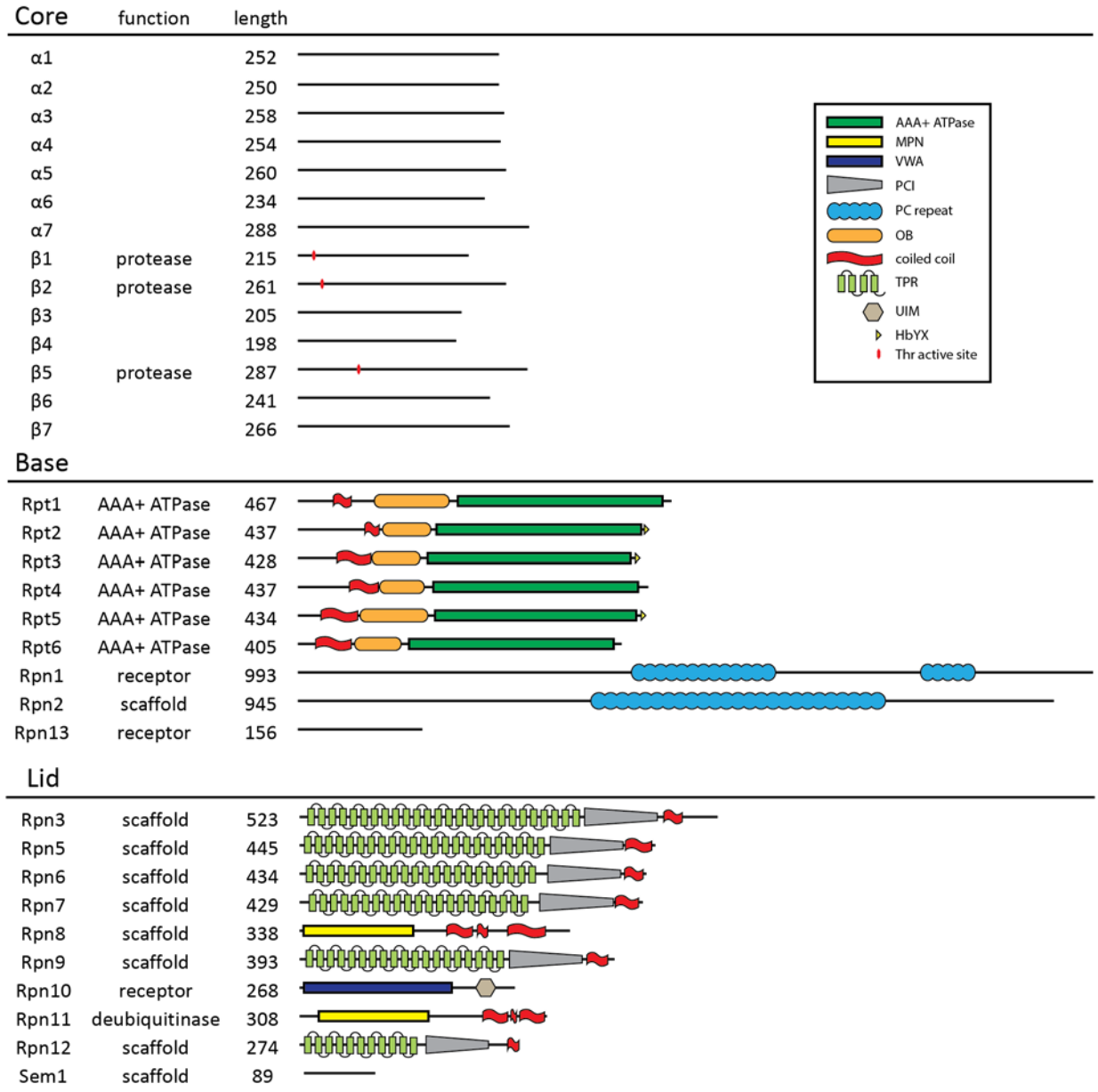

Table 1.1: Protein domains of the 26S proteasome
Coiled coil regions were determined using the coils server (Lupas et al. 1991) and the atomic coordinates of the sub-nanometer proteasome model PDB:4CR2 (Unverdorben et al. 2014). Domain boundaries of the OB and AAA+ ATPase domains were determined from sequence alignments with PAN (Zhang, Zhang, et al. 2009) and the proteasome model (Unverdorben et al. 2014). PCI domains were annotated based on sequence alignments in (Hofmann & Bucher 1998) and the atomic structure of the lid PDB:3JCK (Dambacher et al. 2016). Boundaries of the PC repets, VWA, UIM and MPN domains are based on the primary Uniprot sequence entry for the corresponding proteins.

contains a series of pockets in its apical surface that form between the interfaces of the each α-subunit. These pockets control the conformation of the α-gate and serve as binding sites for the base ATPases in the regulatory particle(Rabl et al. 2008; Smith et al. 2007). Thus, when the regulatory particle binds to the CP through interactions with the α-pockets, the

axial gates are opened allowing condemned proteins to access the proteolytic active sites of the core.

1.3.2 The base

In all known ATP-dependent proteases, the hydrolysis of ATP is coupled to protein degradation through the activity of AAA+ ATPases, which mechanically unfold and translocate substrates into an associated compartmental peptidase for degradation. The unfoldase activity of the 26S proteasome is found in the base sub-complex in the form of six distinct AAA+ ATPases termed Rpt1-Rpt6 (*r*egulatory *p*article *t*riple-A ATPase). Each of the base AAA+ ATPases have a similar domain architecture, with an N-terminal domain containing a coiled-coil helix followed by an OB (*o*ligosaccharide-*b*inding) motif, and a C-terminal domain composed of the AAA+ ATPase followed by C-terminal tail extensions (Figure 1.3C, Table 1.1). In the assembled base sub-complex the coiled-coil helices of Rpt1/Rpt2, Rpt3/Rpt6, and Rpt4/Rpt5 dimerize with each other, and the AAA+ ATPase and OB domains of each Rpt subunit form two stacked hexameric rings that coaxially align with the entrance to the core particle in an arrangement similar to the related archaeal ATPase motor, PAN (Zhang, Zhang, et al. 2009). The ring formed by the N-terminal OB domains of each Rpt subunit (the "N-ring") marks the entrance of the central channel leading into the proteasome. The internal surface of the AAA+ ATPase ring is lined with loops that project into the center of the channel and contact the unfolded substrate polypepide, serving to couple the ATP-driven conformational changes of the AAA+ ATPase domains to unfolding and translocation of substrates (Martin et al. 2008). Cryo-electron microscopy (Cryo-EM) studies of the 26S proteasome from yeast revealed that these loops are arranged in a steep spiral staircase arrangement which is believed to help facilitate substrate entry and translocation by the base (Lander et al. 2012; Beckwith et al. 2013; Beck et al. 2012). In the assembled proteasome, the C-terminal tails of each Rpt subunit project down toward the core particle. Importantly, the C-termini of Rpt2, Rpt3 and Rpt5 contain the consensus sequence motif HbYX (hydrophobic/tyrosine/any residue), which is sufficient to dock into the α-pockets of the core particle. Docking of the HbYX motifs into the α-pockets opens the α-gate of the core and forms the primary point of contact between the base the core particle (Smith et al. 2007; Beckwith et al. 2013).

The largest subunits of the proteasome, Rpn1 and Rpn2 (*r*egulatory *p*article *n*on-ATPase), both contain PC (*p*roteasome/*c*yclosome) repeats and associate with the AAA+ ATPase domains of Rpt1/Rpt2 and the coiled coils of Rpt3/Rpt6, respectively (Lander et al. 2012). Rpn1 contains two binding sites on its surface, termed T1 and T2, that allow Rpn1 to serve as a recruitment platform for ubiquitinated substrates, substrate delivery proteins and the deubiquitinase Ubp6 (Shi et al. 2016; Bashore et al. 2015; Aufderheide et al. 2015). Rpn2 is primarily thought to serve as a scaffolding subunit by making numerous contacts between the base and lid sub-complexes in the fully assembled proteasome (Lander et al. 2012; Beck et al. 2012). Additionally, Rpn2 also plays a role in ubiquitin recruitment by binding Rpn13, a proteasomal ubiquitin receptor(Lander et al. 2012; Beck et al. 2012).

1.3.3 The lid

The lid is composed of ten distinct subunits including six scaffolding subunits (Rpn3, Rpn5-9 and Rpn12), one ubiquitin receptor (Rpn10), and a deubiquitinase, (Rpn11) (Figure 1.3D). Except for the ubiquitin receptor Rpn10, all lid subunits contain C-terminal α-helices that come together in a large helical bundle. Association of all the C-terminal helices into the bundle is required for proper lid assembly, and mutations within their C-terminal helices lead to large lid assembly defects (Estrin et al. 2013). Six of the lid subunits (Rpn3, 5-7, 9 and 12) contain a series of N-terminal TPR (*T*etratrico*p*eptide *R*epeat) motifs followed by a PCI (*P*roteasome, *C*OP9, *I*nitiation factor 3) domain. As their name suggests, PCI domains are not only found in the proteasome lid, but also in the COP9 signalosome and eIF3 (Hofmann & Bucher 1998). In all of these complexes, winged-helix motifs within the PCI domains assemble to form a horseshoe-shaped structure that may be important for templating the overall organization of the PCI-containing subunits (Lander et al. 2012; Lingaraju et al. 2014; des Georges et al. 2015). The lid also contains two MPN-domain (*M*pr1/*P*ad1/*N*-terminal) containing proteins, Rpn11 and Rpn8. Rpn11 contains the deubiquitinase activity of the lid and forms a heterodimeric complex with Rpn8 via their MPN domains (Beck et al. 2012; Matyskiela et al. 2013; Worden et al. 2014; Pathare et al. 2014). The heterodimeric organization of the MPN-containing subunits is also mimicked in the COP9 signalosome and eIF3 (Lingaraju et al. 2014; des Georges et al. 2015). In the context of the assembled proteasome, Rpn11's active site is positioned directly above the N-ring of the base, allowing Rpn11 to remove ubiquitin chains from proteasome substrates *en bloc* (Lander et al. 2012; Matyskiela et al. 2013; Verma 2002; Yao & Cohen 2002).

1.4 Trajectory of protein degradation by the 26S proteasome

Protein degradation by the 26S proteasome is a complex process involving numerous steps that must be well coordinated to allow efficient substrate turnover. Many structural and biochemical studies have shed light on the individual steps of protein turnover and, when taken together, paint a picture of the mechanism of substrate degradation by the 26S Proteasome (Figure 1.4). Prior to encountering a substrate, the proteasome resides in a ground state (apo-state) where the central channel of the base is highly constricted and misaligned with the α-gate in the core (Figure 1.4A). In this conformation the pore loops of the ATPases adopt a steep spiral staircase arrangement with Rpt3 occupying the highest position (Lander et al. 2012; Beck et al. 2012). Importantly, prior to encountering substrate, Rpn11's active site is positioned beside the opening of the N-ring and is occluded behind the Rpt4/Rpt5 N-terminal coiled-coil. The first step in substrate degradation is the recruitment of a protein that has been tagged with lys11 or lys48-lined ubiquitin chains (Figure 1.4B). Three subunits of the proteasome are known to bind ubiquitin: Rpn13, Rpn10 and Rpn1. Rpn13 interacts with ubiquitin through a PRU (*p*lextrin-like *r*eceptor for *u*biquitin) domain,

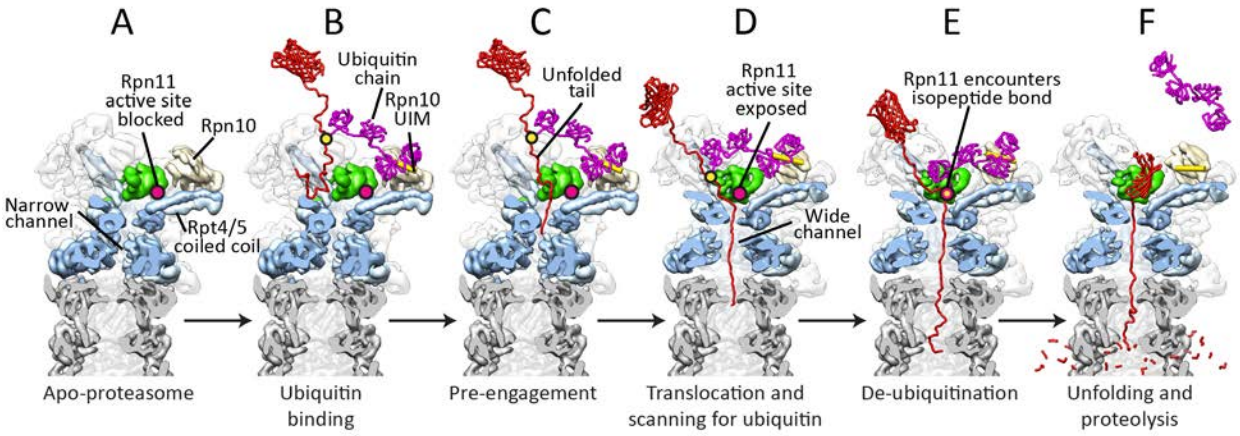

Figure 1.4: Trajectory of protein degradation by the 26S proteasome
Cryo-electron microscopy reconstructions of the apo-proteasome, EMD:5668 (**A-C**) and the substrate-engaged proteasome, EMD-5669 (**D-F**) are shown in cutaway view. (**A**) Apo-proteasome without substrate. The translocation channel in the ATPases is constricted and the active site of Rpn11 is occluded behind the Rpt4/Rpt5 coiled coil. (**B**) Substrate binds to one of the proteasomes 3 ubiquitin receptors, Rpn10 is depicted. (**C**) An unstructured sequence on the substrate protein encounters the central translocation channel and gets engaged by the ATPase motor. (**D**) After engagement, the proteasome switches into a translocation competent state. The translocation channel widens and Rpn11 moves over the channel to scan for ubiquitin modifications. When Rpn11 encounters ubiquitin it removes the chain *en bloc* (**E**) and allows unfolding and proteolysis to continue (**F**). Adapted from (Matyskiela et al. 2013).

Rpn10 binds ubiquitin though a UIM (*U*biquitin *i*nteracting *m*otif) and Rpn1 recruits ubiquitin through its T1 site (Husnjak et al. 2008; Schreiner et al. 2008; Wang et al. 2005; Shi et al. 2016). After binding to the proteasome via its ubiquitin tag, the substrate protein becomes engaged by the base AAA+ ATPases (Figure 1.4C). Efficient engagement requires an unstructured region in the substrate protein of relatively high sequence complexity and substrate proteins lacking an unstructured region are degraded very slowly (Prakash et al. 2004; Fishbain et al. 2015). Additionally, each base ATPase seems to contribute unequally to engagement as mutations in subunits that occupy the highest position of the spiral staircase, where incoming substrates first encounter the ATPases, cause very strong degradation defects (Beckwith et al. 2013). Once a substrate has become engaged by the AAA+ ATPases of the base the proteasome goes through a large conformational change that is thought to bring the proteasome into a translocation-competent state (Matyskiela et al. 2013) (Figure 1.4D). In this conformational change, the central translocation channel of the base widens and aligns coaxially with the α-gate of the core, providing translocating substrates with a direct conduit into the degradation chamber of the core. Additionally, repositioning of the base ATPases results in the inter-subunit contacts between the AAA+ ATPase domains becoming more symmetric and adopting a conformation that more easily supports processive substrate translocation (Matyskiela et al. 2013). Importantly, Rpn11 moves from its partially occluded position behind the Rpt4/Rp5 coiled-coil beside the central translocation channel to sit over the N-ring, positioning its active site directly over the entrance to the proteasome. Because Rpn11 sits directly over the translocation channel, it is optimally positioned to scan for ubiquitin modifications along substrates being actively fed into the proteasome by the action of the base (Figure 1.4E). When Rpn11 encounters a

ubiquitin chain, it cuts the isopeptide linkage between the first ubiquitin in the chain and the substrate, amputating the entire ubiquitin chain from the substrate protein all at once (Matyskiela et al. 2013; Yao & Cohen 2002; Verma 2002). Finally, with the ubiquitin modifications removed, the proteasome can complete degradation by unfolding and translocating the rest of the substrate protein into the core (Figure 1.4F).

1.5 Conserved features of JAMM deubiquitinases

Rpn11 is a member of the JAMM family of DUBs. JAMM DUBs are unique in that, compared to all other known DUB families, they are the only class which utilize a zinc cofactor for catalysis. Additionally, deubiquitinases within the JAMM family contain distinctive structural features that influence their interactions with ubiquitin substrates. At the beginning of my PhD, most of what was known about the JAMM family of DUBs came from studies of AMSH-LP (*a*ssociated *m*olecule with *SH*3 domain of STAM-*l*ike *p*rotease) (Sato et al. 2008). AMSH-LP is a Lys63 specific deubiquitinase that is not involved in protein degradation, but instead plays an important role in ESCRT (*e*ndosomal *s*orting *c*omplex *r*equired for *t*ransport) signaling. Crystal structures AMSH-LP bound to Lys63 linked di-ubiquitin revealed that two insertion sequences, termed insert-1 (Ins-1) and insert-2 (Ins-2), intimately interact with the bound ubiquitin substrate, are required for efficient catalysis (k_{cat}), and determine the linkage specificity of AMSH-LP as a Lys63 DUB (Figure 1.5) (Sato et

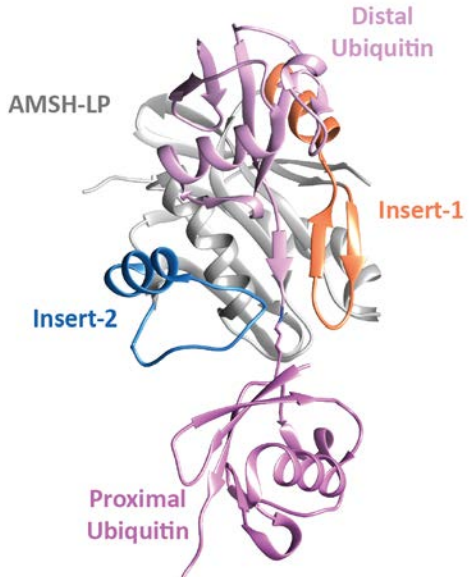

Figure 1.5: AMSH-LP is a quintessential member of the JAMM family of DUBS
The crystal structure of AMSH-LP bound to Lys63 di-ubiquitin is shown (PDB:2ZNV, Sato et al. 2008). The C-terminal α-helix of insert-1 (orange) is responsible for binding to the distal ubiquitin, and the N-terminal region of insert-1 forms a β-sheet with the C-terminus of the distal ubiquitin, positioning the Isopeptide bond in the active site. Insert-2 (blue) makes numerous contacts with the surface of the proximal ubiquitin surrounding Lys63.

al. 2008). Conservation between Rpn11 and AMSH-LP suggested that Rpn11 interacted with ubiquitin substrates in a similar manner as AMSH-LP, and it had even been reported that Rpn11 was a Lys63 specific DUB (Cooper et al. 2009).

However, comparisons between Rpn11 and AMSH-LP could not provide answers to many outstanding questions regarding Rpn11's role in proteasomal protein degradation. How is the activity of Rpn11 regulated in the proteasome and proteasome sub-complexes? How is Rpn11 able to remove ubiquitin chains from the huge variety of proteasome substrates? Why is Rpn11 specific for the isopeptide linkage between the substrate and the first ubiquitin in a chain? What structural features influence Rpn11's activity? How is the activity of Rpn11 tied to substrate translocation? During my PhD it was my ambition to answer these core questions and in the following chapters I will present data that begins to shed light on Rpn11's central role in protein degradation by the 26S proteasome.

2. Structure of the Rpn11-Rpn8 dimer reveals mechanisms of substrate deubiquitination during proteasomal degradation

A portion of the work presented in this chapter has been previously published as part of the following paper: Worden, E.J., Padovani C. and Martin, A. Structure of the Rpn11-Rpn8 dimer reveals mechanisms of substrate deubiquitination during proteasomal degradation. Nat. Struct. Mol. Biol. 21:220-7, 2014.

2.1 Introduction

The ubiquitin proteasome system is responsible for strictly regulated ATP-dependent protein degradation in all eukaryotic cells (Finley 2009; Glickman & Ciechanover 2002). In this process, damaged, misfolded or obsolete proteins are marked for degradation by condensation of one or several of their lysine side chains with the C terminus of ubiquitin to form an isopeptide linkage (Pickart 2001). Polyubiquitination, which is required for degradation by the 26S proteasome, occurs when additional ubiquitin moieties are attached to any of the seven lysine residues within ubiquitin itself, to form chains with different linkage types. Ubiquitin chains linked through Lys11, Lys48 and potentially Lys63 target substrate proteins to the 26S proteasome (Xu et al. 2009; Saeki et al. 2009; Thrower et al. 2000), where before degradation the ubiquitin chains are removed by deubiquitinases (DUBs) that cleave the isopeptide bonds.

The 26S proteasome is a 2.5-MDa molecular machine composed of at least 34 different proteins, 11 of which have enzymatic activities (Matyskiela & Martin 2013). It can be biochemically separated into three subcomplexes: the core peptidase, the base and the lid (Saeki et al. 2012). The core peptidase consists of four stacked heptameric rings that form a proteolytic chamber with sequestered active sites accessible only to unfolded polypeptides through gated axial pores (Groll et al. 1997; Groll et al. 2000). The base is made from nine subunits, six of which are AAA+ ATPases that form a heterohexameric ring and constitute the molecular motor of the proteasome (Glickman et al. 1998). This ATPase ring binds to the axial surface of the core and translocates protein substrates into the degradation chamber after mechanically unraveling their folded structures (Smith et al. 2007; Beckwith et al. 2013; Erales et al. 2012; Zhang, Wu, et al. 2009; Peth et al. 2013). The lid sits on one side of the base and is composed of ten subunits, including the only essential DUB of the proteasome, Rpn11 (Verma 2002; Yao & Cohen 2002; Lander et al. 2012). During degradation, condemned proteins are tethered by their polyubiquitin modification to an intrinsic ubiquitin receptor within the lid or the base, before a flexible segment of their structure is engaged by the translocation machinery of the base ATPase ring (Inobe et al. 2011). Removal of attached ubiquitins by Rpn11 is then required for efficient substrate translocation through the narrow axial pore into the peptidase (Verma 2002).

Rpn11 is a Zn^{2+}-dependent DUB of the JAMM- and MPN-protein family (Verma 2002; Yao & Cohen 2002). Many MPN-domain proteins have highly divergent insertion sequences, termed Insert-1 (Ins-1) and Insert-2 (Ins-2), which intervene in the core MPN fold (Sato et al. 2008). The Ins-1 region of JAMM DUBs has been suggested to function in both recognizing the distal ubiquitin in a diubiquitin substrate and correctly positioning the distal-ubiquitin C terminus over the DUB active site for isopeptide-bond cleavage (Figure 2.1A). In contrast,

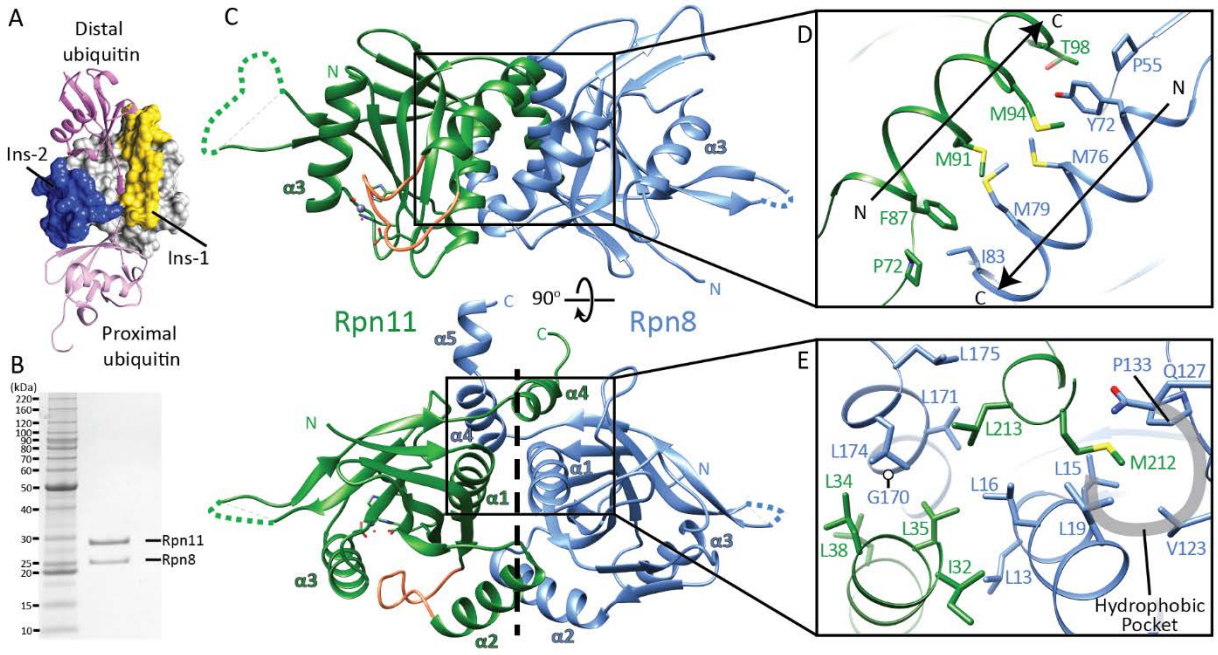

Figure 2.1: Rpn11 and Rpn8 form a heterodimer through two distinct interfaces
(**A**) Structure of the Rpn11-related DUB AMSH-LP, highlighting the proximal and distal moieties of a bound Lys63-linked diubiquitin substrate as well as the Ins-1 and Ins-2 segments involved in binding. Distal refers to the moiety whose C-terminal glycine forms the isopeptide linkage with the lysine in the proximal moiety. (**B**) Coomassie-stained SDS-PAGE gel of the purified Rpn11– Rpn8 heterodimer. Rpn11 gave reproducibly better staining despite its 1:1 stoichiometry with Rpn8. (**C**) Structure of the Rpn11–Rpn8 heterodimer, shown in two orientations rotated by 90° with respect to each other. Rpn11 and Rpn8 are colored green and blue, respectively, and the Ins-1 loop of Rpn11 is colored orange. Zn^{2+}-coordinating residues of the Rpn11 active site are shown in stick representation. The α-helices in Rpn11 and Rpn8 are labeled α1–α4 and α1–α5, respectively (with α5 formed by four additional residues left behind after PreScission cleavage of the purification tag). In the bottom image, the dashed line indicates the pseudo–two-fold axis of rotation between Rpn11 and Rpn8. (**D**) Close-up view showing the structure of Rpn11–Rpn8 dimerization interface 1. Hydrophobic interactions are shown by orange dashed lines. The helices of interface 1 are arranged in an antiparallel orientation denoted by the black arrows. (**E**) Close-up view showing the structure of interface 2. Hydrophobic interactions are indicated with orange dashed lines. A gray horseshoe emphasizes the hydrophobic pocket in Rpn8 that accommodates Met212 of Rpn11.

the Ins-2 region seems to determine the DUB specificity for a certain ubiquitin linkage type by interacting with the proximal ubiquitin. For instance, in the Rpn11-related DUB AMSH-LP the Ins-2 region contacts the proximal moiety of Lys63-linked diubiquitin (Sato et al. 2008). Throughout this thesis, I will refer to the moieties on either side of a scissile isopeptide bond as 'distal' and 'proximal'. The distal moiety presents its C-terminal glycine to the DUB active site, and the proximal moiety is bound through its isopeptide-linked lysine (Figure 2.1A).

Cryo-EM studies of the proteasome holoenzyme revealed that Rpn11 forms a dimer with Rpn8, the only other proteasomal MPN-domain protein, and is located directly above the central pore leading into the N-terminal-domain ring (N ring) of the base ATPases (Beck et al. 2012; Matyskiela et al. 2013; Lander et al. 2012). Owing to steric restrictions imposed by this proximity to the base N ring, Rpn11 may be prevented from cleaving between ubiquitin moieties. The enzyme in the proteasome context seems to remove chains *en bloc* by hydrolyzing the isopeptide bond between a substrate lysine and the C terminus of the first ubiquitin(Yao & Cohen 2002), but it remains unknown whether cleavage can also occur

between ubiquitin moieties or whether the enzyme exhibits any linkage-type specificity (Cooper et al. 2009).

Deubiquitination by Rpn11 has been shown to depend on ATP hydrolysis by the base and may thus be tightly linked to the other degradation steps of substrate engagement, unfolding and translocation (Verma 2002; Yao & Cohen 2002). One model predicts that the ATPase-driven translocation of a protein substrate pulls the isopeptide bonds of attached ubiquitin modifications into the Rpn11 active site for cleavage. However, this complicated set of coupled processes has so far strongly hindered detailed mechanistic studies of this DUB in the proteasome context. Furthermore, Rpn11 has proven over many years to be extremely recalcitrant to purification, thus making biochemical and structural studies of the isolated enzyme impossible. These obstacles have also prevented the development of potent inhibitors for Rpn11, which is an attractive drug target for attenuation of proteasomal degradation.

To obtain high-resolution structural and mechanistic insights, we optimized the Rpn11–Rpn8 heterodimer from *S. cerevisiae* for crystallization and functional characterization *in vitro*. Here we present the 2.0-Å-resolution crystal structure of this heterodimer. Unexpectedly, the structure reveals that the Rpn11 catalytic groove lacks several features that are conserved in related DUBs and were predicted to be critical for ubiquitin binding or stabilization of the isopeptide bond for cleavage. Rpn11 is missing an important aromatic residue thought to contact the hydrophobic Ile44 patch of ubiquitin, and it uses a flexible Ins-1 loop to position the C terminus of the distal ubiquitin moiety for cleavage. Furthermore, Ins-2 is not involved in stabilizing the isopeptide bond above the active site but instead contacts the non-ATPase subunit Rpn2 of the base and thereby probably anchors Rpn11 within the proteasome complex. Rpn11 thus differs substantially from related DUBs in its mode of ubiquitin interaction, consistent with Rpn11 deubiquitination occurring concomitantly with substrate translocation.

2.2 Results

2.2.1 Purification of the Rpn11-Rpn8 heterodimer

It had been suggested by our lab and other labs that Rpn11 and Rpn8 form a dimer within the proteasome lid and that this dimerization occurs through an interface between the MPN domains of the two proteins (Beck et al. 2012; Estrin et al. 2013). Furthermore, we have shown previously that the lid subcomplex is assembled through the formation of a large helical bundle consisting of the C-terminal helices of all lid subunits including Rpn8 and Rpn11 (Estrin et al. 2013; Echalier et al. 2013). We thus reasoned that the numerous previous attempts to purify Rpn11 in isolation were unsuccessful because its MPN dimerization surface was unsaturated and its C-terminal helices were not paired with others in the helical bundle. To get around this problem, we coexpressed C-terminally truncated variants of Rpn11 (residues 2–239) and Rpn8 (residues 1–179), which contained only their respective MPN domains (hereafter referred to as Rpn11 and Rpn8) and affinity tags for purification. Using this coexpression construct, we were able to purify DUB-active Rpn11–Rpn8 heterodimers to high purity and yield (Figure 2.1B).

2.2.2 Structure of the Rpn11-Rpn8 heterodimer

We obtained crystals of the Rpn11–Rpn8 heterodimer complex from proteins purified under conditions in which the catalytic Zn^{2+} ion was stripped from Rpn11, which thus formed an apoenzyme complex. We collected X-ray diffraction data not only on these apoenzyme crystals but also on the active Zn^{2+}-bound complex, after soaking crystals in Zn^{2+}-containing mother liquor (Table 2.1). We accomplished molecular replacement by using Csn5 (PDB 4F70) (Echalier et al. 2013) and Mov34 (PDB 2O95) (Sanches et al. 2007) as search models for Rpn11 and Rpn8, respectively. Apart from the appearance of electron density for Zn^{2+} in the Rpn11 active site (Figure 2.2), the structure of the Zn^{2+}-bound Rpn11–Rpn8 heterodimer did not show any major structural differences when compared to the apoenzyme complex. In addition, residues around the active site of Rpn11, both in the apo and Zn^{2+}-bound states, are nicely superimposable with the structure of the related DUB AMSH-LP with bound diubiquitin, thus further confirming that our Rpn11 structure represents an active, functionally relevant conformation.

Table 2 1: Data collection and refinement statistics

	Zn^{2+}-bound Rpn11-Rpn8	Zn^{2+}-free
Data collection		
Space group	$P4_32_12$	$P4_32_12$
Cell dimensions		
a, *b*, *c* (Å)	70.296 70.296 198.912	70.405 70.405 198.887
α, β, γ (°)	90 90 90	90 90 90
Resolution (Å)	48.23-1.991 (2.02 - 1.99)	40.615-1.950 (1.98-1.950)
R_{sym}	0.076 (0.710)	0.075 (n.a)
I / σI	20.62 (3.40)	20.99 (3.62)
Completeness (%)	99.33 (98.31)	92.56 (72.00)
Redundancy	8.1 (8.3)	11.9 (12.0)
Refinement		
Resolution (Å)	48.23 - 1.991	40.615-1.950
No. reflections	34915	37562
R_{work} / R_{free}	0.161 / 0.1951	0.1626 / 0.2094
No. atoms	3082	3069
Protein	2702	2714
Ligand/ion	125	84
Water	255	271
B-factors		
Protein	35.50	27.20
Ligand/ion	55.60	44.90
Water	44.00	34.70
R.m.s. deviations		
Bond lengths (Å)	0.013	0.014
Bond angles (°)	1.33	1.39

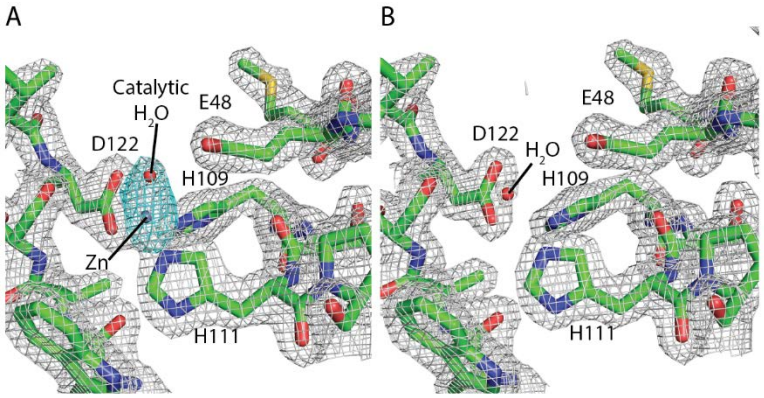

Figure 2.2: Electron density of the Rpn11 active site in the apo and Zn^{2+}-bound states
(**A**) The 2|Fo|-|Fc| electron density map of the Zn^{2+}-bound active site is shown in grey and contoured at 1.5σ. Depicted in cyan is the |Fo|-|Fc| difference electron density map contoured at 5σ, calculated from the final coordinates after three rounds of ADP and reciprocal space XYZ refinement with the Zn^{2+} ion and the catalytic water omitted. (**B**) 2|Fo|-|Fc| electron density map of the Rpn11 active site in the apo state, contoured at 1.5σ. Also included is the corresponding |Fo|-|Fc| difference electron density map contoured at 5σ, which does not show any peaks at this contouring level.

MPN domains in multiprotein complexes generally show a high propensity for dimer formation (Echalier et al. 2013; Sanches et al. 2007). However, available crystal structures of MPN dimers exhibit considerable variation in the mode of dimerization, and it has remained unclear which of the observed interactions, if any, are physiologically relevant. The structure of the Rpn8–Rpn11 heterodimer presented here now reveals an interaction in which the two MPN domains are rotated relative to each other around a pseudo–two-fold axis, in a manner reminiscent of the Rpn8 homodimer structure (Sanches et al. 2007) (Figure 2.1C). The dimerization of Rpn11 and Rpn8 is primarily based on interactions between α-helices that form two distinct interfaces, interface 1 and interface 2, which have a combined buried surface area of ~4,100 $Å^2$ (Figure 2.1C-E). Interface 1, located between Rpn11 α2 and Rpn8 α2, is formed around a cluster of four methionines: Met91 and Met94 of Rpn11 and Met79 and Met76 of Rpn8. Flanking this methionine cluster are other hydrophobic interactions: the γ carbon of Rpn11 Thr98 interacts with the aliphatic side chains of Rpn8 Pro55 and Tyr72, and the ε carbon of Rpn8 Ile83 interacts with Rpn11 Phe87 and Pro72 (Figure 2.1D). Interestingly, the helices of interface 1 pack in an antiparallel orientation, and the interacting residues are closely matched between the two proteins, thus emphasizing the overall pseudo–two-fold symmetry of the entire complex.

Interface 2 primarily consists of a four-helix bundle formed between α1 and α4 of Rpn11 and α1 and α4 of Rpn8. In a swap-like arrangement, α4 of Rpn11 and α4 of Rpn8 reach across the interface, and each interacts tightly with the MPN domain of the other protein (Figure 2.1C, E). The four-helix bundle has a tightly packed hydrophobic core rich in leucine residues. In particular, Leu35 and Leu213 of Rpn11 and Leu174 and Leu16 of Rpn8 are involved in numerous hydrophobic contacts and compose the center of the hydrophobic core (Figure 2.1E). Interestingly, Rpn11 Met212 packs into a very tight hydrophobic pocket formed by Rpn8 Pro133, Gln127, Val123, Leu19, Leu15 and Leu16. The residue in Rpn8 corresponding to Rpn11 Met212 (related by the pseudo–two-fold symmetry of the complex) is Gly170, which packs very tightly against Rpn11 Leu34, Leu35 and Leu38 (Figure 2.3). This

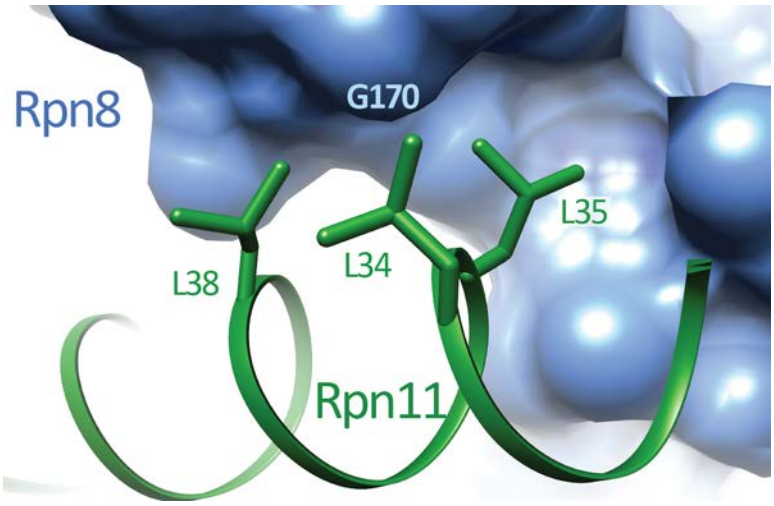

Figure 2.3: Specific interface residues facilitate Rpn11–Rpn8 heterodimer formation
Close-up view of interactions between Rpn11 (green) and Rpn8 (blue, surface representation) at interface 2. Rpn8 Gly170 packs against Rpn11 Leu34, Leu35, and Leu38 (shown in stick representation). For the interaction of the corresponding residue Rpn11 Met212 with Rpn8 see Figure 2.1.

substantial size difference between corresponding residues at the interface probably facilitates heterodimer formation and may explain why homodimers of only Rpn8 and not Rpn11 are observed as byproducts of the coexpression. The hydrophobic pocket that accommodates Rpn11 Met212 in the heterodimer with Rpn8 would not exist in an Rpn11 homodimer. Packing of this residue against Rpn11 Leu34, Leu35 and Leu38 would therefore lead to major steric clashes that preclude Rpn11-homodimer formation.

Five multiprotein complexes in humans that contain pairs of JAMM- or MPN-domain proteins have so far been identified: the lid of the 26S proteasome, the COP9 signalosome, eIF3, BRISC and BRCA1-A (Cooper et al. 2010; Hofmann & Bucher 1998; Wang et al. 2007; Sobhian et al. 2007). An increasing body of evidence suggests that the MPN-domain proteins in these complexes have an intrinsic ability to form dimers. Furthermore, sequence alignments of Rpn11 and Rpn8 with their cognate JAMM- and MPN-domain counterparts in these complexes reveal that the residues making up the hydrophobic cores of the dimer interfaces 1 and 2 are chemically well conserved, despite a strong divergence in primary sequence. It thus seems likely that the Rpn11-Rpn8 interaction represents a general mode of dimerization that may be recapitulated in at least a subset of other JAMM- and MPN-domain containing complexes and may have a role in positioning the respective subunits for their catalytic or scaffolding functions. After publication of this work (Worden et al. 2014) structures of the COP9 signalosome, eIF3 and the MPN dimer of the BRISC complex were published. As predicted, the MPN dimerization interface of the COP9 signalosome and eIF3 were structurally conserved with the Rpn11-Rpn8 heterodimer (Lingaraju et al. 2014; des Georges et al. 2015), but the MPN heterodimer within the BRISC complex utilizes a different dimerization interface (Zeqiraj et al. 2015).

2.2.3 Rpn11 lacks predicted residues for binding ubiquitin

Previous structural studies on the related DUB, AMSH-LP, revealed that its interface for binding to the hydrophobic patch around Ile44 of ubiquitin is composed of two surface

residues, Val328 and Phe332 (Sato et al. 2008). These residues seemed to align well with Rpn11 Val83 and Phe87, respectively, and on the basis of this apparent conservation it had been proposed that Rpn11 binds the Ile44 patch of ubiquitin in a manner very similar to that of AMSH-LP (Figure 2.4A). However, our structure-based alignment between Rpn11 and AMSH-LP revealed that Rpn11 displays Asp85 and Ala89, rather than Val83 and Phe87, at the positions predicted to be critical for ubiquitin binding (Figure 2.4A, B). Strikingly, Phe87 is involved in forming interface 1 with Rpn8, thus making this residue completely inaccessible for ubiquitin binding (Figure 2.4B).

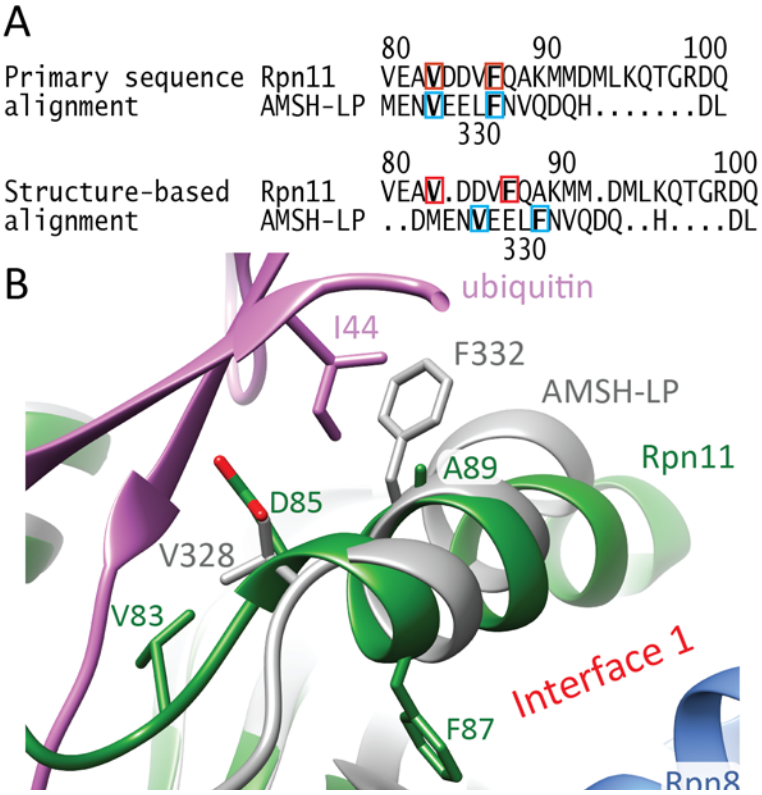

Figure 2.4: Rpn11 is missing a conserved binding site for the Ile44 patch of ubiquitin
(**A**) Sequence alignments between the helical Ins-1 region of Rpn11 and AMSH-LP. Top, primary-sequence alignment, with the ubiquitin- interacting residues of AMSH-LP highlighted in blue and the previously proposed corresponding residues of Rpn11 highlighted in red. Bottom, structure-based alignment showing a two-residue offset between Rpn11 and AMSH-LP. (**B**) Structure of the predicted ubiquitin-binding surface of Rpn11. Rpn11 and Rpn8 are shown in green and blue, respectively. The crystal structure of ubiquitin-bound AMSH-LP20 (PDB 2ZNV; AMSH-LP in gray, ubiquitin in pink) is superimposed with the structure of Rpn11. AMSH-LP residues involved in the binding of the ubiquitin Ile44 patch are shown in stick representation. Residues at the corresponding positions in Rpn11 as well as residues previously predicted to bind ubiquitin are also shown as sticks.

On the basis of the observed sequence differences, we predicted Rpn11's K_m for diubiquitin cleavage to be much higher than that of AMSH-LP. Surprisingly, using a gel-based assay for the cleavage of Lys48-linked diubiquitin, we found that Rpn11 has a K_m of ~120 μM, which is only 70% higher than the K_m of ~72 μM for AMSH-LP (Table 2.2 and Figure 2.5). Because Rpn11 appeared to lack hydrophobic residues conserved in AMSH-LP to bind the Ile44 patch of ubiquitin, we sought to characterize its mode of ubiquitin binding in more detail. If Rpn11 binds ubiquitin in a similar orientation as does AMSH-LP, reconstructing an

AMSH-LP-like binding surface in Rpn11 would be expected to lower the K_m for diubiquitin cleavage. To test this hypothesis, we generated the mutants Rpn11(A89F) and Rpn11(D85V). The A89F mutation decreased the K_m 3.4-fold (Table 2.2), indicating that wild-type Rpn11 indeed binds the distal ubiquitin in a similar orientation as does AMSH-LP, but it lacks hydrophobic residues thought to be required for tight interaction with the Ile44 hydrophobic patch. In contrast, the D85V mutation led to a 1.7-fold increase in K_m relative to that of wild type, suggesting that a valine residue in this position of Rpn11 does not favorably contribute to ubiquitin binding. Moreover, this mutation decreased the k_{cat} for diubiquitin cleavage to 27% (Table 2.2), possibly by affecting the orientation of the distal ubiquitin and thus the positioning of the isopeptide bond in the Rpn11 active site. Consistently with our data, this valine residue is not well conserved among JAMM DUBs or even within the AMSH family of proteins (Sato et al. 2008; Davies et al. 2011), despite being implicated in AMSH-LP binding to the Ile44 patch of ubiquitin.

Table 2.2: Kinetic parameters for isopeptide bond cleavage by wild-type or mutant Rpn11 in context of the Rpn11–Rpn8 heterodimer

ND, not detectable. K_m and k_{cat} values for diubiquitin hydrolysis by wild-type (WT) or mutant Rpn11 were determined by Michaelis–Menten analyses, with 5 μM of Rpn11–Rpn8 and a gel-based assay to follow cleavage. The K_d value for diubiquitin binding to the catalytically inactive Rpn11^{V80A} was measured by the change in tryptophan fluorescence. K_m and k_{cat} values for ubiquitin-lysine-TAMRA cleavage were determined with a fluorescence-polarization assay with Rpn11–Rpn8 at 250 nM and 1.25 μM and ubiquitin-lysine-TAMRA concentrations ranging from 1 to 10 μM. All reported values are the average of three measurements ± s.d. (n = 3 technical repeats).

Rpn11 (in Rpn8 context)	Ub2 linkage type	K_m (μM)	k_{cat} (min^{-1})
WT	48	120 ± 28	0.29 ± 0.11
WT	63	299 ± 52	0.38 ± 0.05
WT	11	147 ± 43	0.74 ± 0.20
WT	Ubiquitin-lysine-TAMRA	20 ± 1	0.95 ± 0.02
A89F	48	36 ± 7	0.25 ± 0.06
D86V	48	205 ± 43	0.08 ± 0.01
L132A	48	320 ± 36	0.07 ± 0.01
V78A	48	142 ± 41	0.20 ± 0.07
S79A	48	218 ± 50	0.13 ± 0.01
V80A	48	(K_d = 67 ± 35)	ND
E81A	48	515 ± 96	0.11 ± 0.01
Δ78-81	48	ND	ND
78-81 AAAA	48	ND	ND

Together, these results indicate that Rpn11 and AMSH-LP bind ubiquitin in a similar orientation but differ considerably in their interactions with the Ile44 hydrophobic patch. Ubiquitin-binding affinity of Rpn11 can therefore be increased by the reengineering of a critical phenylalanine present at the equivalent position in AMSH-LP. In contrast to the lack of this phenylalanine, Rpn11 contains other conserved or highly similar residues that have been shown to mediate ubiquitin binding in AMSH-LP. For instance, Rpn11 displays Leu132 in the same position as AMSH-LP Met370, the latter of which makes important interactions

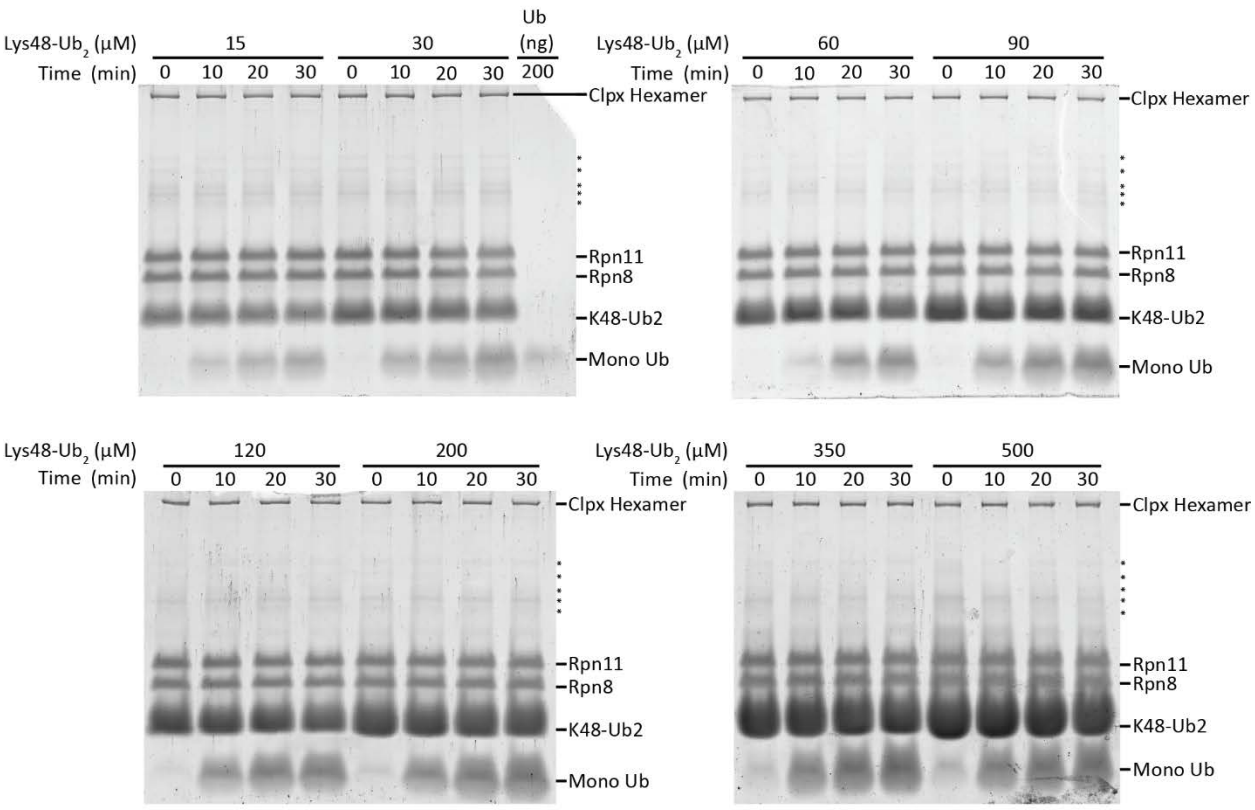

Figure 2.5: Example gels for the Lys48-linked diubiquitin cleavage assay of Rpn11
Shown are the gels for one Michealis-Menten experiment analyzing the 30-minute time courses of Lys48-linked di-ubiquitin cleavage by wild-type Rpn11-Rpn8 (5 μM) at substrate concentrations between 15 and 500 μM. Bands indicated by asterisks are due to contaminating proteins that co-purify at low abundance with Rpn11 and Rpn8 heterodimers. Covalently linked ClpX hexamer was used for normalization of staining and enzyme concentrations across different gels, which were all processed in parallel.

with the hydrophobic pocket formed by Ile36, Leu69 and Leu71 of ubiquitin. Indeed, the Leu132A mutation in Rpn11 leads to a 2.6-fold increase in K_m and a 5.4-fold decrease in k_{cat} for diubiquitin cleavage, results indicating that this residue is important for both ubiquitin binding and isopeptide-bond hydrolysis (Table 2.2).

2.2.4 Ins-2 of Rpn11 is not involved in ubiquitin binding

Rpn11 contains both Ins-1 and Ins-2, but Ins-2 is not ordered in our structure of the isolated Rpn11–Rpn8 dimer. The absence of a defined conformation may be caused by the lack of Zn^{2+}-coordinating residues in the Ins-2 of Rpn11. In AMSH-LP, these Zn^{2+}-binding residues appear to structure Ins-2 and allow its interaction with the proximal ubiquitin (Sato et al. 2008). Docking of the Rpn11 crystal structure into the EM density of the substrate-bound proteasome holoenzyme (Matyskiela et al. 2013) indicates that Ins-2, together with the Rpn11 N terminus, interacts with Rpn2 and helps position Rpn11 above the proteasome pore (Figure 2.6). Thus, the role of the Ins-2 region in Rpn11 seems completely distinct from that in AMSH-LP. Because a defined conformation of the Rpn11 Ins-2 may depend on its

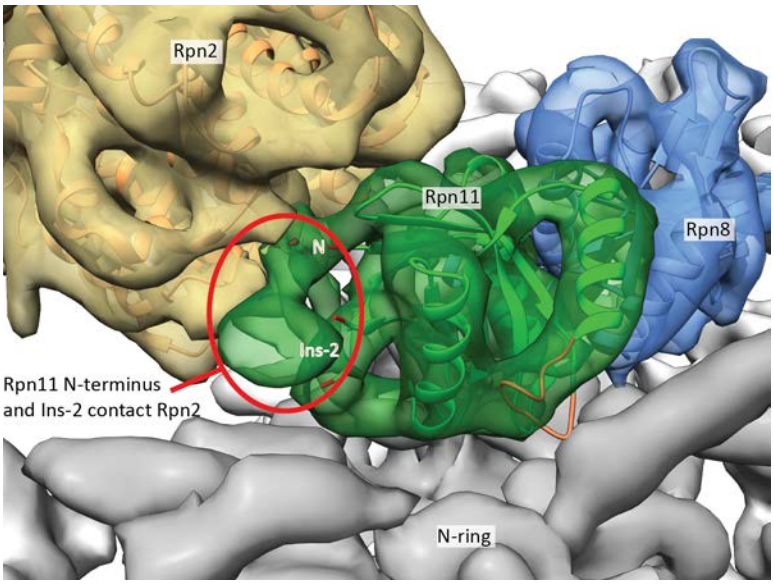

Figure 2.6: The N terminus and Ins-2 region of Rpn11 contact Rpn2
Crystal structures of the Rpn11-Rpn8 dimer and Rpn2 (PDB ID: 4ADY), with Rpn11 in green, Rpn8 in blue and Rpn2 in orange, are docked into the segmented EM 3D-reconstruction of the substrate-bound 26S proteasome (Matyskiela et al. 2013) (EMDB ID: EMD-5669). The Ins-1 loop of Rpn11 is colored gold. The N-terminal residue of Rpn11 as well as the residues flanking its unstructured Ins-2 region are colored red and labeled. Extra electron density not accounted for by the crystal structures of Rpn11-Rpn8 and Rpn2, and presumably corresponding to the Ins-2 region of Rpn11, is circled.

interactions with Rpn2, it is not surprising that this segment is unresolved in the structure of the isolated Rpn11–Rpn8 dimer.

Our crystal structure, in combination with the proteasome EM reconstruction, clearly indicates that Rpn11 lacks the interfaces for contacting the proximal moiety of a bound diubiquitin, an interaction that would be required to confer linkage specificity. Docking of diubiquitin into Rpn11, with the scissile isopeptide bond placed at the active site, shows that the proximal ubiquitin is completely exposed (Figure 2.7A). Using the diubiquitin cleavage assay (Figure 2.7B and Figure 2.5), we accordingly found that Rpn11 does not exhibit linkage specificity in its deubiquitination activity. Isolated Rpn11 efficiently cleaves all seven ubiquitin linkage types (Figure 2.7B). Lys11-, Lys48- and Lys63-linked diubiquitins are cleaved with k_{cat} values of 0.74, 0.29 and 0.38 min^{-1}, respectively, and K_m values of 147, 120 and 299 μM, respectively (Table 2.2). The relatively small differences in K_m and k_{cat} are presumably a consequence of the different linkage types forming variable compact ubiquitin-chain conformations that make the isopeptide bond transiently inaccessible. It has been shown previously that these conformations 'breathe' and expose the isopeptide bond with different frequencies, thus leading to variations in DUB cleavage rates (Ye et al. 2012). Moreover, depending on the linkage type, steric clashes between the proximal ubiquitin and Rpn11 may influence the K_m. Another factor that is likely to affect K_m and k_{cat} for cleavage of isolated diubiquitin is the extent of nonproductive binding, in which the first, proximal moiety interacts with the distal site of the Rpn11-binding groove and thus competitively inhibits isopeptide-bond cleavage between ubiquitin moieties. Because a modification on Lys63 of a distally bound ubiquitin probably leads to fewer steric clashes with Rpn11 than does a modification on Lys48 or Lys11, the proximal ubiquitin of isolated Lys63-linked

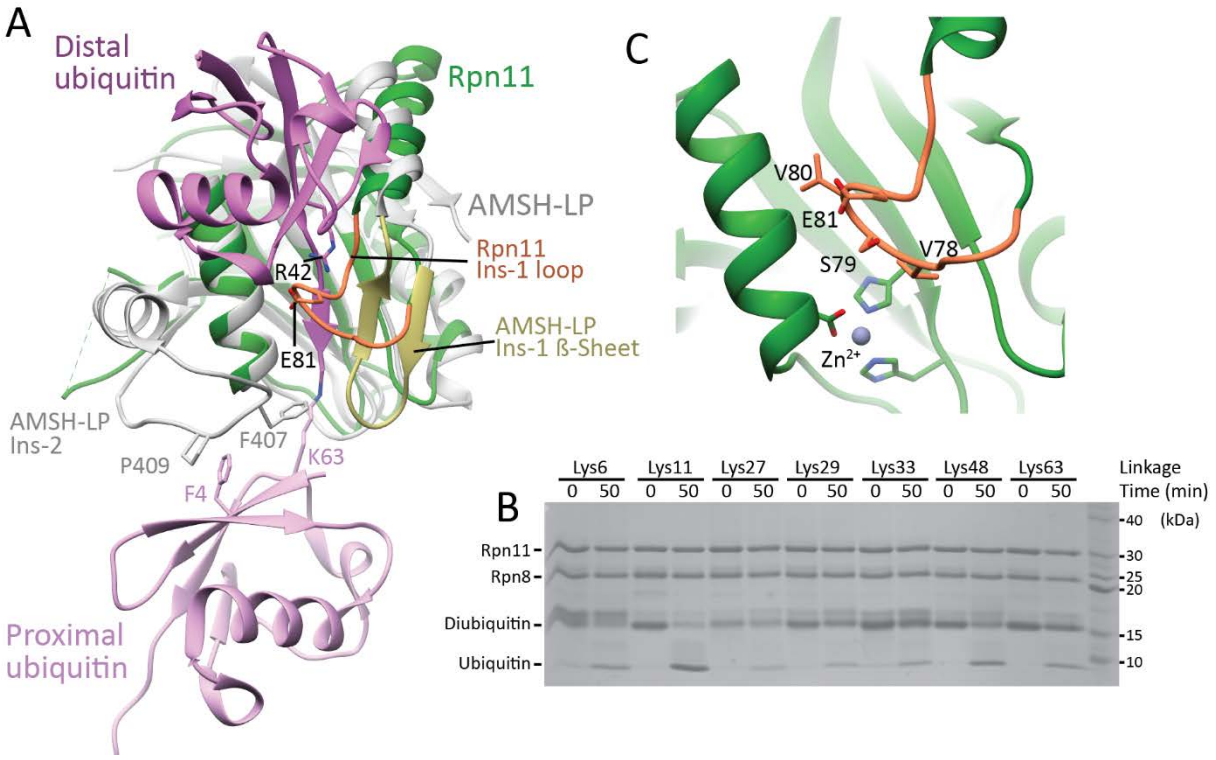

Figure 2.7: Missing proximal contacts allow Rpn11 cleavage promiscuity
(**A**) Superimposition of the crystal structures for ubiquitin-bound AMSH-LP (gray; PDB 2ZNV) and Rpn11 (green). The Ins-1 segments involved in stabilizing the ubiquitin C terminus in the catalytic groove are shown in orange for Rpn11 and yellow for AMSH-LP. Residues that mediate the interaction between AMSH-LP Ins-2 and the proximal ubiquitin are shown as sticks. In Rpn11, Ins-2 is relocated away from the proximal ubiquitin to interact with Rpn2. Potentially interacting residues between the Rpn11 Ins-1 loop and the distal ubiquitin (Glu81 and Arg42) are also shown in stick representation. (**B**) Rpn11 cleavage of multiple diubiquitin linkage types. Shown is a Coomassie-stained SDS-PAGE gel detailing Rpn11 cleavage of Lys6-, Lys11-, Lys27-, Lys29-, Lys33-, Lys48- and Lys63-linked diubiquitin. (**C**) Structure of the Rpn11 catalytic site, oriented as in **A**. The Ins-1 loop (colored orange) covers the binding groove and is shown with individually mutated residues in stick representation. The Zn^{2+}-coordinating residues of Rpn11 are also in stick representation.

diubiquitin may be a better competitive inhibitor than the proximal ubiquitin in other linkage types. This could explain the higher K_m for Lys63-linked diubiquitin despite its reportedly less compact and more extended conformation. Importantly, for deubiquitination during proteasomal degradation such competitive inhibition would not exist because the ubiquitin chain would be attached to a protein substrate as the proximal moiety.

To assess whether the identity or folding state of the moiety proximal to the isopeptide bond affects K_m as well as k_{cat}, we measured Rpn11 cleavage of ubiquitin-lysine-TAMRA (Table 2.2 and Figure 2.8A–C). The determined K_m of ~20 µM is 6- to 15-fold lower than the K_m values for Lys11-, Lys48- or Lys63-linked diubiquitin, a result consistent with our model that a globular structure on the proximal side of the isopeptide bond leads to some steric hindrance in Rpn11 binding. Therefore, Rpn11 apparently does not make favorable interactions with a proximal ubiquitin, and this is in agreement with the observed lack of cleavage within ubiquitin chains. The k_{cat} of 1 min^{-1} for ubiquitin-lysine-TAMRA is very similar to the k_{cat} values for diubiquitin. This similarity indicates that in its catalysis Rpn11

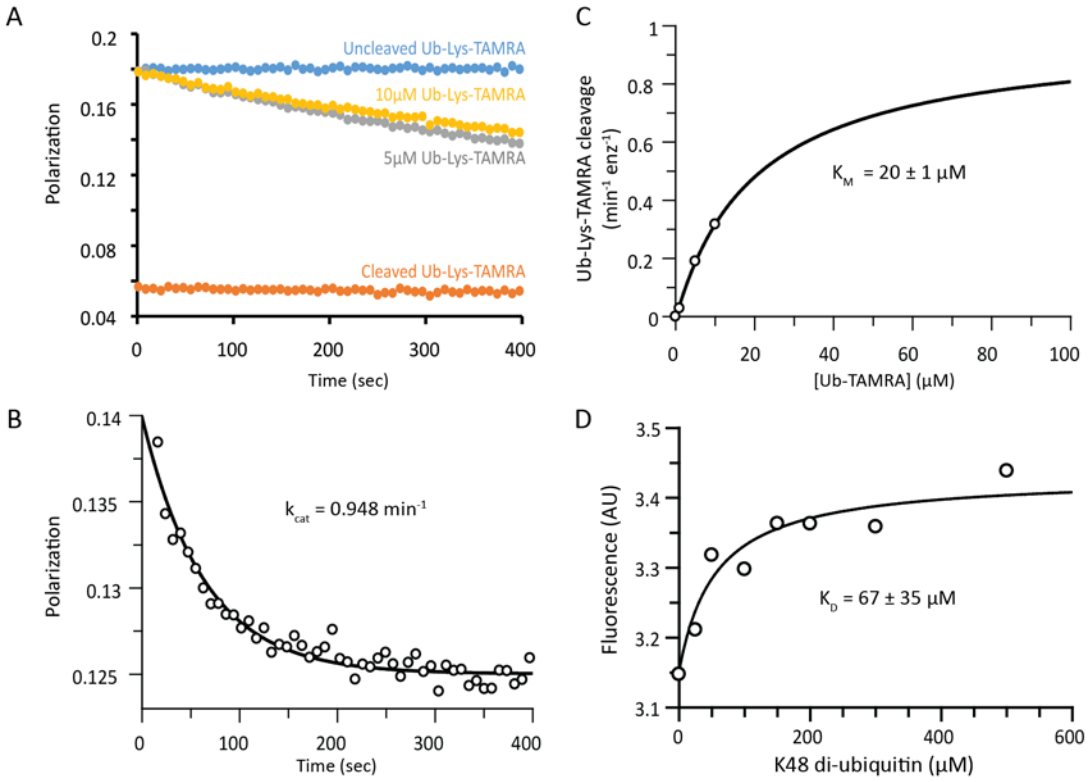

Figure 2.8: Fluorescence-based assays for Rpn11 ubiquitin binding and cleavage
(**A**) Example time-based polarization measurements of the cleavage of 5 and 10 μM Ub-Lys-TAMRA by 1.25 μM Rpn11-Rpn8. (**B**) Example single-turnover kinetics measurement for the cleavage of 100 nM Ub-Lys-TAMRA by 450 μM Rpn11-Rpn8. The data are fit by a single exponential, with a calculated k_{cat} = 0.95 min^{-1}. (**C**) Michaelis-Menten curve for Ub-Lys-TAMRA cleavage by Rpn11, where k_{cat} was constrained to the experimentally determined value in (**B**). Limitations in substrate solubility precluded using Ub-Lys-TAMRA at concentrations higher than K_M, so measurement of a complete curve was not possible. The estimated K_M for Ub-Lys-TAMRA cleavage by Rpn11 is 20 μM. (**D**) Tryptophan fluorescence-based assay of K48-linked di-ubiquitin binding to Rpn11^{V80A}. Tryptophan fluorescence of 5 μM Rpn11-Rpn8 heterodimers was measured in the presence of Lys48-linked di-ubiquitin at concentrations between 0 and 500 μM, as discussed in the methods. Triplicate fluorescence measurements were averaged and fit to a simple binding curve with a K_D of 67 μM.

does not discriminate the identity or folding state of the molecule on the proximal side of the scissile bond. This is in excellent agreement with Rpn11's promiscuous function in the proteasome context, in which it removes ubiquitin chains from highly variable protein substrates. Steric restrictions by the neighboring base N ring appear to preclude larger folded domains, including ubiquitin, from the proximal side of the scissile bond, such that Rpn11 is assumed to cleave only at the base of the ubiquitin chain, between the substrate lysine and the very first ubiquitin. The variable compactness of different ubiquitin chain types would therefore have no effect on the accessibility of the cleaved isopeptide bond and the rate of deubiquitination at the proteasome. Potential K_m differences that originate from different linkage types on the ubiquitin bound to the distal site of Rpn11 are also likely to be irrelevant because ubiquitin chains are tethered to intrinsic proteasome receptors with high affinity that substantially increase the local substrate concentration.

2.2.5 Flexible Ins-1 loop positions distal ubiquitin for cleavage

Our structural data suggest that Rpn11 binds its ubiquitin substrates exclusively by contacting the distal side of the isopeptide bond. Interestingly, the Ins-1 region of Rpn11 includes a prominent loop that sits over the ubiquitin-binding groove, approximately 12 Å away from the active site residues (Figure 2.7C). This loop has high *B* factors, indicating that it has some level of intrinsic flexibility. The position of the Ins-1 loop over the catalytic groove could suggest that it blocks access for the ubiquitin C terminus and thereby fulfills an auto-inhibitory function to reduce spurious isopeptide cleavage, similarly to a mechanism proposed for Csn5 in the COP9 signalosome(Echalier et al. 2013). On the basis of this model, deletion of residues from the Rpn11 Ins-1 loop should increase isopeptide-cleavage activity by exposing the catalytic groove for ubiquitin binding. However, we found that deletion of the highly conserved residues 78–81 in the Rpn11(Δ78–81) mutant completely abolished DUB activity (Table 2.2). Similarly, a mutant with residues 78–81 replaced by alanines lacked detectable activity, thus ruling out that the defects observed for the loop truncation were simply caused by a strained conformation with a distorted active site. Consequently, the Ins-1 loop of Rpn11 does not act in an inhibitory fashion but rather seems to be required for catalysis.

To determine whether interactions of this loop with ubiquitin contribute primarily to K_m or k_{cat}, we individually mutated residues 78–81 to alanine and measured the cleavage of Lys48-linked diubiquitin (Table 2.2). Rpn11(V78A) did not considerably differ from the wild-type enzyme, whereas Rpn11(S79A) and Rpn11(E81A) showed an ∼1.8- and ∼4.3-fold increase in K_m, respectively, and a ∼2.2- and ∼2.6-fold decrease in k_{cat}, respectively. Importantly, the V80A mutation completely eliminated diubiquitin cleavage. Using a tryptophan fluorescence–based ubiquitin binding assay, we found that the K_d of Rpn11(V80A) is similar to or even slightly lower than the K_m of wild-type Rpn11 (Table 2.2 and Figure 2.8D). This indicates that the observed lack of cleavage activity for this mutant originates from a severe defect in k_{cat}. The Ins-1 loop may thus have an important role in positioning the C terminus of the distal ubiquitin for isopeptide-bond cleavage.

The corresponding Ins-1 region in AMSH-LP does not adopt a loop conformation but forms a short two-stranded β-sheet in the absence of ubiquitin. This β-sheet defines one edge of the catalytic groove and stabilizes a bound substrate for cleavage by forming a three-stranded sheet with the C terminus of the distal ubiquitin. Because Rpn11 and AMSH-LP appear to bind the distal ubiquitin in a similar orientation, we superimposed their crystal structures to generate a model for ubiquitin-bound Rpn11 (Figure 2.7A). On the basis of this simple model, the Ins-1 loop of Rpn11 folds over the unstructured ubiquitin C terminus, in a similar area to that where AMSH-LP forms the three-stranded sheet. Rpn11 and AMSH-LP thus seem to use the same portions of their Ins-1 regions but very distinct strategies to interact with and stabilize the ubiquitin C terminus in the catalytic groove.

Comparison of our cryo-EM reconstructions for the substrate-free and stalled substrate-bound proteasome revealed that the engagement of ubiquitinated substrate leads to the appearance of a bridging density over the ubiquitin-binding groove of Rpn11 (Lander et al. 2012; Matyskiela et al. 2013) (Figure 2.9A–C). Docking the Rpn11 crystal structure into the EM maps allowed us to unambiguously assign this bridging density to the Ins-1 loop, which is lifted out of the catalytic groove by ∼2.0 Å (Figure 2.9C). Additionally, the EM density of the Ins-1 loop did not agree with the formation of a β-sheet that is seen for AMSH-

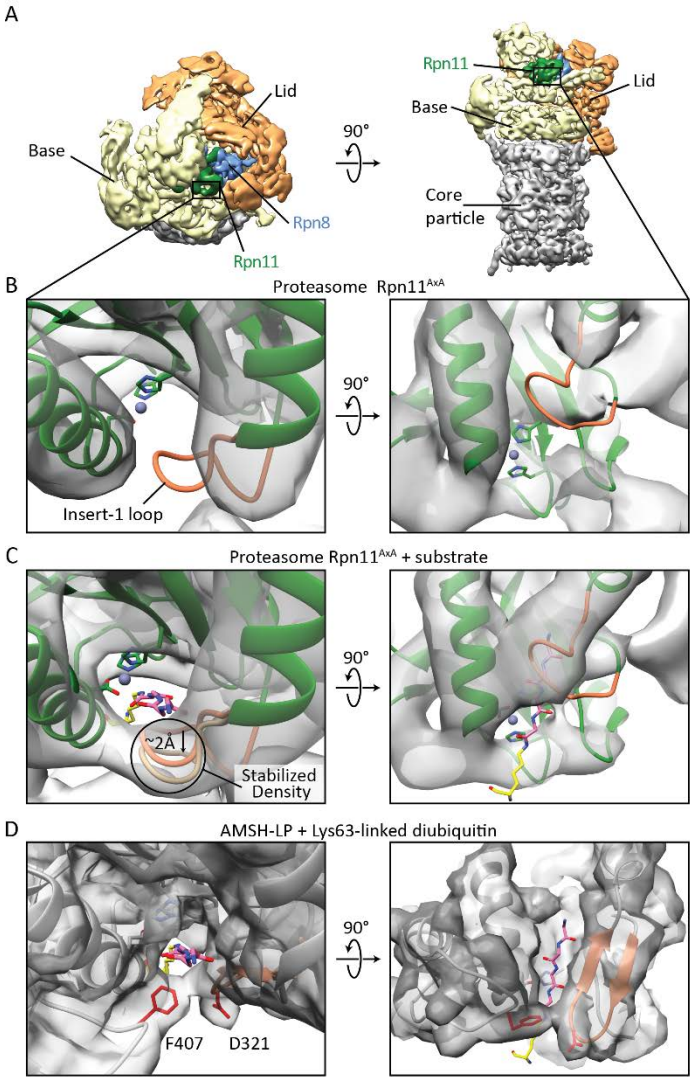

Figure 2.9: The Ins-1 loop of Rpn11 acts as a flap to fold over the ubiquitin C terminus
(**A**) EM three-dimensional reconstruction of the proteasome holoenzyme as shown from the top (left) and front (right). Rpn11 and Rpn8 are shown in green and blue. The lid, base and core-particle subcomplexes are shown in orange, tan and gray, respectively. (**B**) Close-up views of the crystal structure of Rpn11 docked into the EM reconstruction of substrate-free yeast proteasomes with catalytically dead Rpn11 (Rpn11AxA) as viewed from the top (left) and front (right). (**C**) Close-up views of the Rpn11 structure docked into the EM reconstruction of $Rpn11^{AxA}$-mutant proteasomes stalled on an ubiquitinated substrate, again viewed from the top and front. The backbone for the C-terminal portion of the distal ubiquitin (Leu-Arg-Gly-Gly; pink) and the side chain for the isopeptide-linked lysine (yellow), were docked on the basis of the ubiquitin-bound model of Rpn11 and are shown in stick representation. In addition to the rigid-body fit of the entire Rpn11, including the Ins-1 loop (orange), we manually docked the isolated loop (yellow) to fit even better into the observed EM density. (**D**) Close-up views of the ubiquitin-bound AMSH-LP crystal structure (PDB 2ZNV) with its simulated EM-density envelope and the C-terminal Leu-Arg-Gly-Gly-Lys peptide (pink and yellow sticks) are shown in orientations similar to those of Rpn11 in **B** and **C**. Residue Asp321 of Ins-1 and residue Phe407 of Ins-2 form a bridge over the active site and are depicted as red sticks.

LP. We had originally interpreted the appearance of this bridging density as the Ins-1 loop of Rpn11 folding over the C-terminus of a bound ubiquitin and stabilizing over the active site for efficient cleavage (Figure 2.7A, Figure 2.9C) (Worden et al. 2014). This interpretation

seemed consistent with the fact that a similar structural feature had been observed in AMSH-LP where Phe207 and Asp321 formed and active site enclosure by folding over the C terminus of a bound ubiquitin (Figure 2.9D) (Sato et al. 2008). Consistently with these architectural similarities, mutations of both the Ins-1 loop in Rpn11 and the Phe407 residue in AMSH-LP (Sato et al. 2008) lead to severe catalytic defects, probably by disrupting the stabilization of the ubiquitin C terminus in the catalytic groove. However, the crystal structure of Rpn11 bound to ubiquitin (Chapter 3) revealed that the Ins-1 loop of Rpn11 instead forms a β-sheet with the C terminus of ubiquitin.

2.2.6 Rpn11 has low catalytic efficiency

On the basis of our crystal structure of Rpn11 and the EM reconstruction of the proteasome holoenzyme, Rpn11 lacks important elements that could directly contact and stabilize the Gly-Gly-Lys isopeptide linkage in the active site (Figure 2.7A). In particular, we do not expect the Ins-1 loop to interact with the far C terminus of ubiquitin around the isopeptide bond, and Ins-2 is probably precluded from positioning the scissile bond, owing to its contacts with Rpn2. The observation that Rpn11 lacks those specific isopeptide-stabilizing interactions is corroborated by its very low k_{cat} of ~0.3–0.7 min^{-1} for diubiquitin and 1 min^{-1} for ubiquitin-lysine-TAMRA. Rpn11 cleaves Lys63-linked diubiquitin ~134 times more slowly than does AMSH-LP (Sato et al. 2008), which more strongly stabilizes the isopeptide bond for cleavage, for instance through an active site enclosure by the bridging residues Phe407 and Asp321 (Figure 2.9D).

Rpn11-mediated deubiquitination during substrate degradation by the proteasome has been shown to be strictly dependent on ATP hydrolysis by the base (Verma 2002; Yao & Cohen 2002). Interestingly, this degradation-coupled deubiquitination happens at the same rate as the cleavage of ubiquitin-lysine-TAMRA by isolated Rpn11 (1 min^{-1}; (Matyskiela et al. 2013) and this study), thus suggesting that deubiquitination by Rpn11 represents the rate-limiting step of proteasomal degradation. ATPase-driven polypeptide translocation into the base N ring, located below Rpn11, may pull the isopeptide bond at the base of an attached ubiquitin chain into the Rpn11 active site and thus overcome steric hindrances between the substrate and subunits surrounding Rpn11 in the proteasome context. The active site architecture of Rpn11 may have been optimized to accommodate highly divergent protein substrates *en route* to the central processing pore and to allow the removal of their ubiquitin modifications concomitantly with degradation, while non-engaged substrates are precluded from deubiquitination.

2.3 Conclusions

Our high-resolution crystal structure of the proteasome Rpn11–Rpn8 heterodimer provides critical insights into the architecture of MPN-domain dimers as well as the mechanisms of Rpn11-mediated substrate deubiquitination at the 26S proteasome. Various ubiquitin-interacting proteins bind to the hydrophobic patch around Ile44 of ubiquitin, and it has so far been assumed that Rpn11 interacts in a similar manner with this patch to bind its substrates for isopeptide cleavage. Remarkably, our crystal structure now reveals that the critical phenylalanine used by related DUBs to bind the ubiquitin Ile44 patch is instead used

by Rpn11 to stabilize the heterodimer interface with Rpn8, so that this phenylalanine is inaccessible for ubiquitin binding. It is not ruled out that Rpn11 uses a different, unidentified surface to interact with the Ile44 patch. However, the substantial gain in ubiquitin affinity upon introduction of a phenylalanine at the predicted Ile44-binding site suggests that Rpn11 interacts with ubiquitin in an orientation similar to that of related DUBs, such as AMSH-LP. Rpn11 may use the Ile44 patch of ubiquitin in a different manner resulting in lower affinity and therefore may rely to a larger extent on other conserved interfaces for binding. The original surface for Ile44-patch binding may have been repurposed to form stable interactions with Rpn8 when Rpn11 evolved to become incorporated into the 26S proteasome. These contacts with Rpn8 probably help position Rpn11 over the proteasome central pore and allow translocation-coupled substrate deubiquitination.

For deubiquitination during proteasome degradation, Rpn11 must be able to remove ubiquitin chains from the wide variety of substrates, irrespective of the amino acid sequences surrounding the ubiquitin-linked lysines in these proteins. During its evolution, the enzyme probably accomplished such high promiscuity by eliminating structures that stabilize the isopeptide bond in the direct vicinity of the proximal moiety, or even interact with the proximal moiety itself, and that therefore confer selectivity for certain ubiquitin linkages. In AMSH-LP for instance, the Ins-1 and Ins-2 regions stabilize the Gly-Gly-Lys isopeptide segment, but they also determine the Lys63-cleavage specificity, owing to their interactions with the proximal side of the linkage. However, the Ins-2 segment of Rpn11 is removed from the catalytic groove and interacts with Rpn2, which may additionally stabilize the DUB within the proteasome complex. Because Rpn11 is positioned directly above the N ring and even partially occludes the entrance to the central pore, this reduction of protruding structural elements on the proximal side of its catalytic groove probably also facilitates access of protein substrates to the base-translocation machinery and their ATPase-driven passage underneath Rpn11 while being scanned for ubiquitin modifications. In summary, fewer substrate-stabilizing interactions around the active site appear to make Rpn11 less efficient in isopeptide-bond cleavage but extremely promiscuous for the co-translocational deubiquitination of highly variable substrates at the proteasome.

2.4 Materials and methods

2.4.1 Expression and purification of Zn^{2+}-free Rpn11-Rpn8 heterodimers

The MPN domains of both *S. cerevisiae* Rpn11 (residues 2–239) and Rpn8 (residues 1–179) were cloned into the pETDuet-1 expression vector with PreScission cleavable N-terminal His_6 and C-terminal StrepII purification tags respectively to make the Rpn11-Rpn8 expression construct. BL21* (DE3) cells were transformed with the Rpn11-Rpn8 expression construct and grown in dYT medium at 37 °C to OD_{600} = 0.6–0.8. Protein expression was induced overnight at 18 °C with 1 mM isopropyl β-D-thiogalactopyranoside (IPTG). Cells were harvested by centrifugation at 6,000*g* for 25 min and resuspended in lysis buffer 1 (30 mM HEPES, pH 7.6, 100 mM NaCl, 100 mM KCl, 0.5 mM EDTA, 1 mM DTT, 10% glycerol and 20 mM imidazole) supplemented with 2 mg/mL lysozyme, benzonase (Novagen), and protease inhibitors (aprotinin, pepstatin, leupeptin and PMSF). All purification steps were

performed at 4 °C. Cells were lysed by sonication for 2 min and clarified by centrifugation at 15,000 r.p.m. for 30 min. Soluble cell extract was bound to Ni-NTA agarose resin (Qiagen) and washed with lysis buffer for ~30 column volumes. The bound protein was eluted with a buffer containing 60 mM HEPES, pH 7.6, 100 mM NaCl, 100 mM KCl, 0.5 mM EDTA, 1 mM DTT, 10% glycerol, and 250 mM imidazole. The His_6 and StrepII purification tags were removed by dialysis into PreScission cleavage buffer (50 mM Tris-HCl, pH 7.6, 150 mM NaCl, 1 mM EDTA, and 1 mM DTT) with PreScission protease for 2 h. Uncleaved protein was removed by passage over Ni-NTA agarose. Protein in the flow through was concentrated with a 10K MWCO Amicon Ultra spin filter (Millipore) and purified further by size-exclusion chromatography on a HiLoad 16/60 Superdex 200 pg column (GE Life Sciences) in GF buffer (50 mM HEPES, pH 7.5, 50 mM NaCl, 50 mM KCl, 0.5 mM EDTA, 1 mM DTT, and 10% glycerol). The purified protein was flash frozen with liquid nitrogen and stored at −80 °C.

2.4.2 Purification of Zn^{2+}-bound Rpn11-Rpn8 heterodimers

Cloning and protein expression of the active Rpn11–Rpn8 heterodimer was the same as for the Zn^{2+}-free Rpn11–Rpn8 heterodimer, except that growth medium was supplemented with 150 μM $ZnCl_2$. Cells were harvested by centrifugation at 6,000*g* for 25 min and resuspended in lysis buffer 2 (60 mM HEPES, pH 8.0, 100 mM NaCl, 100 mM KCl, and 10% glycerol) supplemented with 2 mg/mL lysozyme, benzonase (Novagen), and protease inhibitors (aprotinin, pepstatin, leupeptin and PMSF). All purification steps were performed at 4 °C. Cells were lysed by sonication for 1 min and clarified by centrifugation at 15,000 r.p.m. The soluble extract was then bound to Strep-Tactin Superflow Plus resin (Qiagen) and washed with lysis buffer 2 for ~30 column volumes. Protein was eluted with elution buffer 2 containing 60 mM HEPES, pH 8.0, 100 mM NaCl, 100 mM KCl, 10% glycerol and 2.5 mM desthiobiotin. The His_6 and StrepII purification tags were removed by cleavage with PreScission protease for 2.5 h in the elution buffer. After cleavage, the protein was concentrated and further purified by size-exclusion chromatography on a HiLoad 16/60 Superdex 200 pg column (GE Life Sciences) in lysis buffer 2. Fractions containing the purified protein were concentrated, flash frozen in liquid nitrogen and stored at −80 °C.

2.4.3 Ubiquitin expression and purification

Rosetta II (DE3) pLysS *Escherichia coli* cells were transformed with a pET28a vector containing the ubiquitin gene from *S. cerevisiae* under control of a T7 promoter. Cells were grown in Terrific Broth supplemented with 1% glycerol at 37 °C until OD_{600} = 1.5–2.0 and were induced with 0.5 mM IPTG overnight at 18 °C. Cells were harvested by centrifugation, and pellets were frozen at −80 °C. Purification was carried out as described previously (Pickart & Raasi 2005), but scaled up with minor modifications. The lysis buffer contained 50 mM Tris-HCl, pH 7.6, 0.02% NP-40, 2 mg/mL lysozyme, benzonase (Novagen), and protease inhibitors (aprotinin, pepstatin, leupeptin and PMSF). Cells were lysed by sonication and 20 min incubation at room temperature. 60% perchloric acid was added to a final concentration of 0.5%, and the solution was stirred on ice for a total of 20 min. A 5-mL

HiTrap SP FF column (GE Life Sciences) was used for cation-exchange chromatography, and ubiquitin fractions were pooled and exchanged into Ub storage buffer (20 mM Tris-HCl, pH 7.6, and 150 mM NaCl) by repeated dilution and concentration in Amicon Ultra 3000 MWCO spin concentrators (Millipore).

2.4.4 Purification of E1 and E2 enzymes for in vitro ubiquitination

Plasmids containing the Ube1, Cdc34, UbcH13, Uev1A, and Ube2S were gifts from the Morgan laboratory. Ube1 was cloned into pET28a, expressed in *E. coli* and purified with ubiquitin-agarose as described (Ciechanover et al. 1982). Cdc34 was cloned into pET28a with an N-terminal His_{10} affinity tag, and UbcH13, Uev1A, and Ube2S were cloned into pET28a vectors with C-terminal His_6 affinity tags. All polyhistidine-tagged constructs were grown in dYT at 37 °C to OD_{600} of 0.6–0.8 and were induced overnight at 18 °C with 0.5 mM IPTG. Cells were harvested and resuspended in lysis buffer 3 (50 mM Tris-HCl, pH 8.0, 500 mM NaCl, 20 mM imidazole, and 10% glycerol) supplemented with 2 mg/mL lysozyme, benzonase (Novagen), and protease inhibitors (aprotinin, pepstatin, leupeptin and PMSF) at a ratio of 1:3 cell mass (g)/buffer (mL). Cells were lysed by sonication for 2 min at 4 °C, the lysate was clarified by centrifugation at 15,000 rpm for 30 min, and the soluble extract was bound to Ni-NTA agarose resin (Qiagen) and washed with lysis buffer 3. The bound protein was eluted with lysis buffer 3 plus 250 mM imidazole (500 mM imidazole for His_{10}-Cdc34). The eluate was further purified by size-exclusion chromatography on a HiLoad 16/160 Superdex 75 pg column (GE Life Sciences) in E2 storage buffer (20 mM Tris-HCl, pH 7.5, 150 mM NaCl, 1 mM DTT, and 10% glycerol). UbcH13 and Uev1A Ni-NTA eluates were combined before SEC and eluted as a heterodimer. Concentrations of purified proteins were determined by UV absorbance at 280 nm, and proteins were stored at −80 °C.
Ubiquitin dimers were synthesized and purified as described previously (Dong et al. 2011).

2.4.5 Kinetic analysis of Rpn11 DUB activity

All diubiquitin cleavage experiments were performed at 30°C in buffer containing 60 mM HEPES, pH 8.0, 100 mM NaCl, 100 mM KCl and 10% glycerol. The concentration of Zn^{2+}-bound Rpn11–Rpn8 heterodimer was 5 μM for all variants. Initial cleavage rates were measured for eight concentrations of diubiquitin, ranging from 15 to 500 μM (for Rpn11 wild type, D85V, A89F, V78A, S79A, V80A, E81A, Δ78–81, and 78–81A) or from 30 to 700 μM (for Rpn11 E81A and L132A). Cleavage reactions were stopped with 2× SDS-PAGE sample buffer to a final concentration of 3% SDS. Time points for each substrate concentration were analyzed by SDS-PAGE gels stained with SYPRO Ruby (Invitrogen). Monomeric ubiquitin was loaded alongside the cleavage experiments for quantification, and an internal control of single-chain ClpX hexamer was used to normalize for differences in Rpn11 concentration and staining across multiple gels. Gels were imaged on a Typhoon Variable Mode Imager (Amersham Biosciences), with a pixel density of 50 μm/pixel. Monomeric ubiquitin-band intensity was quantified with ImageQuant (GE). Cleavage reactions were repeated three times, and initial rates were fit directly to the Michaelis–Menten equation with nonlinear regression.

Cleavage of ubiquitin-lysine-TAMRA (Boston Biochem) was followed by fluorescence polarization (FP) in buffer containing 50 mM HEPES, pH 8.0, 100 mM NaCl and 100 mM KCl (FP buffer) at 30°C. Concentrated Rpn11–Rpn8 was buffer-exchanged from lysis buffer 2 into FP buffer with a Micro Bio-Spin 6 chromatography column (Bio-Rad). FP was monitored at an excitation wavelength of 544 nm and an emission wavelength of 574 nm. The concentration of ubiquitin-lysine-TAMRA precluded the measurement of a complete Michaelis–Menten curve. k_{cat} and K_m were therefore determined by measurements under single-turnover conditions and multiple turnover at ubiquitin-lysine-TAMRA concentrations in the low-micromolar range. For the single-turnover k_{cat} measurement, FP of 100 nM ubiquitin-lysine-TAMRA in the presence of 450 μM wild-type Rpn11–Rpn8 was monitored over 400 s and fitted to a single exponential (Grafit data analysis, Erithacus). Multiple-turnover measurements of ubiquitin-lysine-TAMRA cleavage were conducted in triplicate with 250 nM or 1,250 nM wild-type Rpn11–Rpn8 at 1 μM, 5 μM, and 10 μM ubiquitin-lysine-TAMRA. Cleavage velocities were calculated with an FP endpoint for completely cleaved ubiquitin-lysine-TAMRA determined after 10-min incubation with 100 nM of the DUB Yuh1. The K_m for Rpn11 cleavage of ubiquitin-lysine-TAMRA was calculated by fitting of the 1 μM, 5 μM, and 10 μM multiple-turnover velocities to a Michaelis–Menten equation and constraining V_{max} (k_{cat}) to the value measured in single-turnover experiments.

2.4.6 Crystal-structure determination of the Rpn11-Rpn8 heterodimer

Zinc-free Rpn11–Rpn8 heterodimer was buffer-exchanged into a buffer containing 60 mM HEPES, pH 7.6, 100 mM NaCl and 1 mM TCEP with a Micro Bio-Spin 6 chromatography column (Bio-Rad). Initial crystallization experiments were performed at 18 °C with the hanging-drop diffusion method. A Mosquito liquid-handling robot (TTP Labtech) was used to set about 360 conditions from sparse matrix crystal screens JCSG+ (Qiagen), Wizard I and II (Emerald Bio), Index I and II (Hampton Research) and Crystal Screen I and II (Hampton Research). After optimization of our initial hits, the best crystals of the Zn^{2+}-free Rpn11–Rpn8 complex were obtained from 4-μl hanging drops, for which 2 μl of 5 mg/ml Rpn11–Rpn8 heterodimer was mixed with 2 μl of precipitant solution containing 15% PEG 8000, 12% ethylene glycol and 100 mM HEPES, pH 7.5. The hanging drops were allowed to equilibrate with a 500-μl reservoir of precipitant solution for 4 d at 18 °C. Crystals were soaked for 5 min in a cryoprotectant solution containing 15% PEG 8000, 30% ethylene glycol, and 100 mM HEPES, pH 7.5 before freezing. Crystals of the Zn^{2+}-bound Rpn11–Rpn8 complex were prepared in the same way as for the Zn^{2+}-free crystals, except that the crystals were soaked for 40 min in a cryoprotectant solution containing 15% PEG 8000, 30% ethylene glycol, 100 mM HEPES, pH 7.5 and 500 μM $ZnCl_2$.

Diffraction data for the Zn^{2+}-free crystals were collected at a wavelength of 1.075 Å at the NSLS beamline X29A (Brookhaven National Laboratory), and data for the Zn^{2+}-bound crystals were collected at a wavelength of 1.11587 Å at the ALS beamline 8.3.1 (Lawrence Berkeley National Laboratory), both at a temperature of ~100 K. Data were processed with HKL2000 (HKL Research). The structure of the Zn^{2+}-free Rpn11–Rpn8 dimer was solved by molecular replacement with the Phenix suite (Adams et al. 2010), with structures of Csn5 (PDB 4F7O) and Mov34 (PDB 2O95) as search models. The structures of Csn5 and Mov34

were modified before molecular replacement with Sculptor. The structure of the Zn^{2+}-bound Rpn11–Rpn8 complex was solved by molecular replacement with the Zn^{2+}-free structure as a search model. Iterative refinement, manual model correction and model building were accomplished with Phenix and Coot[39]. The final molecular models have very good stereochemistry (98% Ramachandran favored for both structures, and 0.3% Ramachandran outliers for the Zn^{2+}-free structure) and rotamer orientations, except for the side chain of Rpn11 R100, which, however, was fit into clear electron density. The Zn^{2+}-free complex was refined to an R_{free} of 0.2094, and the Zn^{2+}-bound structure was refined to an R_{free} of 0.1951. Both the Zn^{2+}-free and Zn^{2+}-bound crystals are in the $P4_32_12$ space group with unit-cell dimensions of a = b = 70.405 and c = 198.887, and a = b = 70.296 and c = 198.912, respectively.

3. Proteasome substrate deubiquitination is controlled by conformational switching of Rpn11's insert-1 loop

3.1 Introduction

Selective protein degradation in eukaryotic cells is accomplished by the ubiquitin proteasome system. In this process, proteins destined for degradation are labeled with Lys11- or Lys48-linked poly-ubiquitin chains that direct the condemned substrate proteins to the 26S proteasome for degradation. The 26S proteasome is a very large (2.5MDa) molecular machine assembled from three subcomplexes with distinct functions called the core particle, base and lid. The proteolytic activity of the proteasome resides in the core particle. The core particle is composed of 4 stacked α and β heptameric rings that surround an axially gated proteolytic chamber, which is inaccessible to folded proteins. Substrate proteins are directed into the core particle through the action of the base, which docks onto the core particle to unfold and translocate proteins into the central degradation chamber. The lid binds to the side and top of the base and contains the subunit Rpn11 which is responsible for removing the ubiquitin chains that direct substrates to the proteasome.

Here we report the crystal structure of Rpn11 bound to mono-ubiquitin. Our structure reveals that, upon ubiquitin binding, Rpn11's Insert-1 loop changes conformation from an auto-inhibited state, where it blocks the enzyme's catalytic groove, to an active state where the Ins-1 loop forms a β-sheet with the C-terminus of ubiquitin. Mutations that affect the switching behavior of the Ins-1 loop revealed that the conformational change from the inhibited the active state is rate limiting for isopeptide cleavage. Finally, proteasome degradation experiments showed that isopeptide bond cleavage by Rpn11 is not the rate limiting step of degradation by the proteasome and that translocation by the base may potentiate formation of the active conformation of the Ins-1 loop and thereby activate Rpn11 in a translocation-dependent manner.

3.2 Results

3.2.1 Structure of the Rpn11-Rpn8 dimer bound to ubiquitin

We previously reported a crystal structure of the Rpn11-Rpn8 heterodimer in the absence of ubiquitin (Worden et al. 2014). To optimize the Rpn11-Rpn8 heterodimer for co-crystallization with ubiquitin we used our previously published structure as a guide to remove disordered sequences, which interfered with crystallization (Figure 3.1A). Rpn11's N terminus and Ins-2 make contacts with Rpn2 in the proteasome context, but are unstructured because these are contacts missing in the isolated heterodimer (Worden et al. 2014). Additionally, the C-terminal helices of Rpn11 and Rpn8 are part of the helical bundle, where they associate with all other lid subunits, but in the isolated Rpn11-Rpn8 heterodimer they are unstructured. We therefore prepared C-terminally truncated variants of the Rpn11-Rpn8 heterodimer that also had Rpn11's N terminus (residues 1-23) removed and the Ins-2 (residues 160-192) replaced with a short glycine-serine linker. The truncated Rpn11-Rpn8

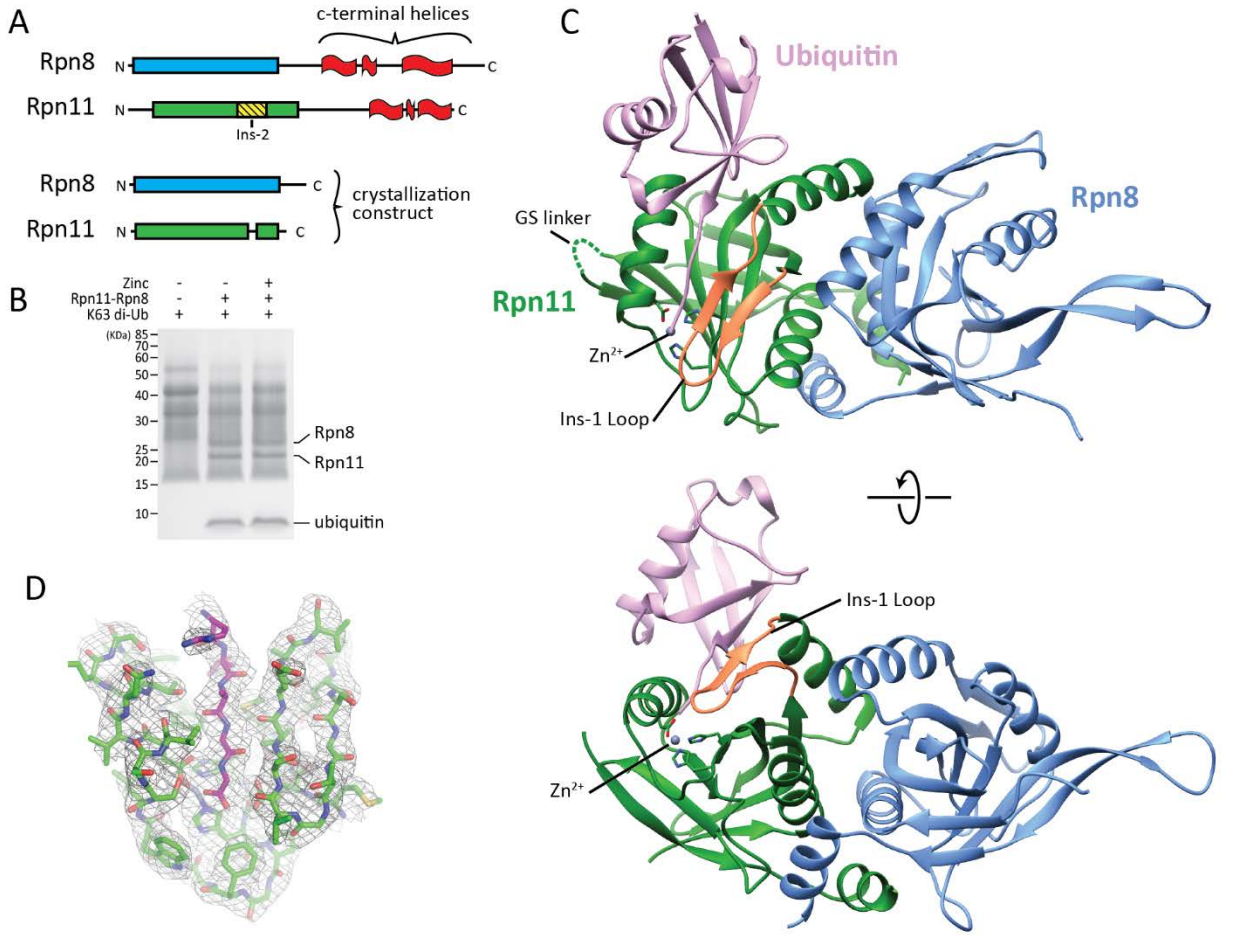

Figure 3.1: Crystal structure of the Rpn11·Ubiquitin-Rpn8 complex
(**A**) Top, Rpn11 and Rpn8 domain architecture. Rpn11 and Rpn8 have N-terminal MPN domains followed by C-terminal helices that are important for lid assembly. Bottom, the crystallization construct of the Rpn11 Rpn8 heterodimer was truncated to remove the C-terminal helices and the Rpn11 sequences N-terminal to the MPN domain and Ins-2. (**B**) lysine-63 linked diubiquitin cleavage experiment showing that the crystallization construct is fully active. (**C**) Crystal structure of the Rpn11 Ubiquitin·Rpn8 complex. Rpn8 is depicted in blue, Rpn11 is depicted in green, and Ubiquitin is depicted in pink. The Ins-1 loop of Rpn11 forms a β-sheet with the C terminus of Ubiquitin and is colored in orange. The catalytic residues which chelate the Zn^{2+} cofactor are shown in stick representation. (**D**) 2|Fo|-|Fc| electron density map of the Rpn11 active site contoured at 1σ with a carve of 1.6Å from the atoms. Density can clearly be seen for the C-terminus of Ubiquitin (pink sticks) forming β-sheet interactions with Rpn11's Ins-1 loop (green sticks).

heterodimer exhibited robust di-ubiquitin cleavage activity that did not increase with the addition of excess $ZnCl_2$ (Figure 3.1B), indicating that this short form of Rpn11 was well folded and its active site was fully occupied with Zn^{2+}. The final crystallization construct consisted of Rpn11(24-160-GGSGSG-192-221) and Rpn8(1-179).

Crystals of the Rpn11·Ubiquitin-Rpn8 complex were obtained (see methods) and the structure of the complex was solved by molecular replacement using coordinates of the *S. cerevisiae* Rpn11-Rpn8 heterodimer (PDB:4O8X) with its insert-1 loop removed and a poly-alanine model of *M. musculus* ubiquitin (PDB: 2ZNV, chain B) that was truncated to residues 1-72 (Table 3.1). The crystal contained one Rpn11·Ubiquitin-Rpn8 complex per asymmetric

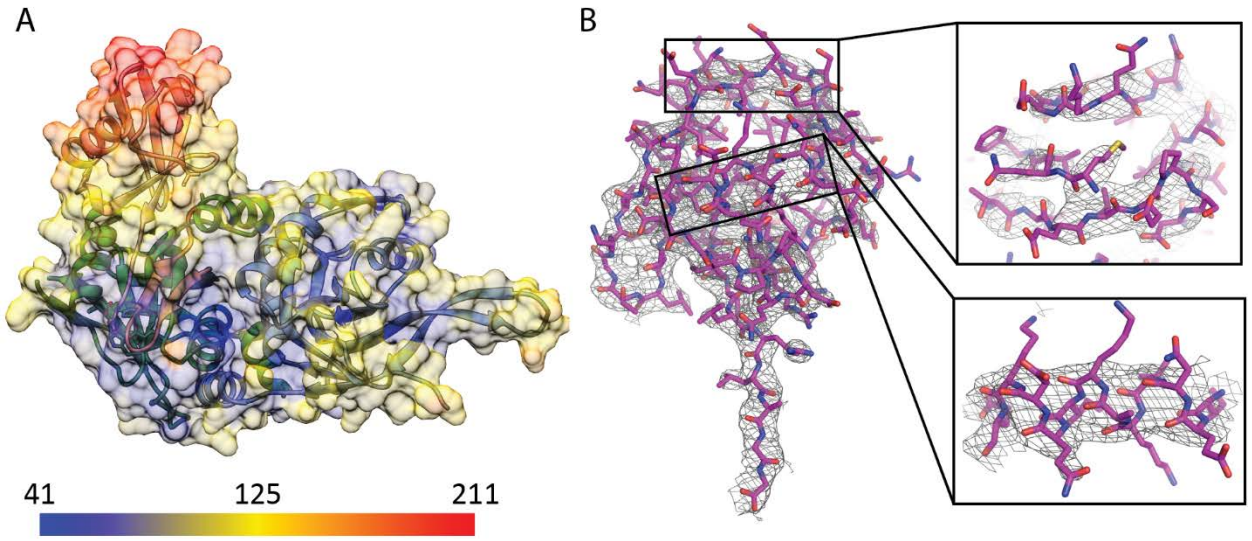

Figure 3.2: B-factors and representative density for ubiquitin suggests high mobility
(**A**) The Rpn11·Ubiquitin-Rpn8 complex is depicted with a semi-transparent surface colored according to atomic B-factors ranging from 41-211. The Rpn11-Rpn8 heterodimer has relatively low B-factors compared to ubiquitin, which has increasingly elevated B-factors farther away from the Rpn11 interaction surface. (**B**) 2|Fo|-|Fc| electron density map surrounding ubiquitin contoured at 1σ with a carve of 1.6Å. Sections of ubiquitin density surrounding Met1 (top right) and the crossover helix (bottom right) are shown in detail.

unit (Figure 3.1C) and was packed in such a way that the folded domain of ubiquitin is oriented toward a large solvent channel. A consequence of this arrangement is that the folded domain of ubiquitin does not make any significant contacts with neighboring asymmetric units and is likely very mobile. Thus, the portions of ubiquitin farthest away from its interaction with Rpn11 are poorly resolved and are modeled with highly elevated B-factors (Figure 3.2). However, at its interface with Rpn11, backbone and sidechain density for ubiquitin is clearly evident and the B-factors are similar to surrounding atoms in Rpn11 (Figure 3.1D, 3.2).

The folded domain of ubiquitin binds within a cleft formed by helix 2 and helix 3 of Rpn11 and ubiquitin's C terminus projects down the catalytic groove formed by Rpn11's helix 3 and insert-1 loop (Figure 3.3A). The very C-terminal carboxy-anion group of ubiquitin Gly76 coordinates the catalytic Zn^{2+} in Rpn11's active site and replaces the catalytic water, similar to the organization of ubiquitin-bound AMSH (Figure 3.3B) (Shrestha et al. 2014). Ile44 of ubiquitin interacts directly with Rpn11 Ala89 (Figure 3.3C), but this interaction surface is much smaller than the interaction between ubiquitin and AMSH-LP, which has a phenylalanine at the same position (Sato et al. 2008). The small interaction surface between Rpn11 Ala89 and Ile44 of ubiquitin explains the significant gain of affinity observed for the Rpn11 A89F mutant designed to mimic the AMSH-LP binding surface (Worden et al. 2014).

3.2.2 Rpn11's Ins-1 loop changes conformation upon ubiquitin binding

Binding of ubiquitin to the Rpn11-Rpn8 heterodimer does not cause any global changes in the structure of either Rpn11 or Rpn8. In fact, the structure of the ubiquitin-free Rpn11-

Rpn8 dimer can be overlaid almost exactly (RMSD = 0.47Å) with the structure of the ubiquitin bound dimer. However, comparison of the ubiquitin-free and ubiquitin-bound Rpn11 structures reveals a striking conformational change in Rpn11's Ins-1 loop that occurs upon ubiquitin binding (Figure 3.4). In the ubiquitin-free state the Ins-1 loop of Rpn11 is flexibly folded over the catalytic groove in an auto inhibitory state (Figure 3.4A) (Worden et al. 2014; Dambacher et al. 2016). However in the ubiquitin-bound state the Ins-1 loop changes conformation to form a 3 stranded β-sheet with the four most C terminal residues of ubiquitin (Figure 3.4B). In this conformational change the Ins-1 loop residues Gly77 and Val78 fold out and down toward the Rpn11 active site to form the hairpin turn at the end of the Ins-1 β-sheet (Figure 3.4B). Interestingly, in the ubiquitin-free state, Val78 associates with a small hydrophobic pocket on the surface of Rpn11 formed by Met50 and the aliphatic sidechain of the catalytic residue Glu48 (Figure 3.4A). However, in the ubiquitin-bound state, this hydrophobic pocket is instead occupied by Val80 (Figure 3.4B). Upon ubiquitin binding Val80 moves from its highly exposed position pointing into the ubiquitin binding cleft to the small hydrophobic pocket, switching places with Val78.

Table 3.1: Data collection and refinement statistics

	Rpn11·Ubiquitin-Rpn8 complex
Data collection	
Wavelength (Å)	1.116
Space group	$P6_522$
Cell dimensions	
a, *b*, *c* (Å)	125.92, 125.92, 140.08
α, β, γ (°)	90 90 120
Resolution (Å)	46.82-2.7 (2.797 – 2.7)*
CC1/2	0.999 (0.364)
$I / \sigma I$	16.58 (1.05)
Completeness (%)	99.99 (100.00)
Redundancy	15.5 (15.9)
Refinement	
Resolution (Å)	48.23 - 1.991
No. reflections	18586
R_{work} / R_{free}	0.2118 / 0.2498
No. atoms	3238
Protein	3237
Ligand/ion	1
Water	0
B-factors	
Protein	91.00
Ligand/ion	108.9
R.m.s. deviations	
Bond lengths (Å)	0.007
Bond angles (°)	1.39

*Values in parentheses correspond to the highest resolution shell

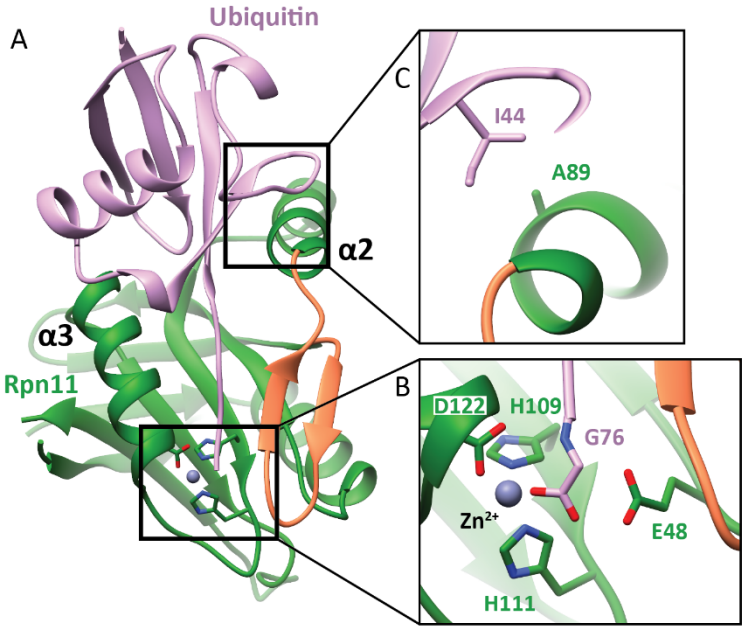

Figure 3 3: Rpn11 interaction with Ubiquitin
(A) Close view of the Rpn11-Ubiquitin interaction. Rpn11 and Ubiquitin are colored as in Figure 3.1 and Rpn8 is hidden for clarity. Ubiquitin binds to Rpn11 within the cleft formed by α2 and α3 of Rpn11. (B) The C-terminal carboxy-anion of ubiquitin Gly76 coordinates the Zn^{2+} in Rpn11's active site. Gly76 of ubiquitin is shown in pink stick representation, and Rpn11's catalytic residues are depicted as green sticks. (C) Close up of the binding interaction between Rpn11 Ala89 and the Ile44 patch of ubiquitin.

3.2.3 Conformation of Rpn11's Ins-1 loop controls its activity

In the ubiquitin-bound state very few contacts are made between the Ins-1 β-sheet and the folded body of Rpn11. In fact the only contact made between a sidechain of the Ins-1 loop and the folded domain of Rpn11 is though Val80 (Figure 3.4B). Thus, it seems that Val80 may act as a tether to stabilize the Ins-1 loop in its β-sheet conformation. This is supported by our previous observation that Rpn11-Rpn8 heterodimers with the Rpn11(V80A) mutation were completely deficient in diubiquitin cleavage activity (Worden et al. 2014). The Rpn11(V80A) mutation probably inhibits Rpn11 activity by reducing its contact surface with the hydrophobic pocket, making the β-sheet conformation unstable even in the presence of ubiquitin. It is likely that the β-sheet conformation of the Ins-1 loop is unstable in the absence of ubiquitin because the interaction mediated by Val80 is not sufficient to lock the Ins-1 loop in a β-sheet, instead the Ins-1 loop needs the extra interactions contributed by folded domain and C-terminus of ubiquitin.

Since it seems that the Rpn11(V80A) mutation effects the activity of Rpn11 by inhibiting the conformational change of the Ins-1 loop from the ubiquitin-free state to the ubiquitin-bound state, we sought to engineer an Rpn11 mutation that stabilizes the Ins-1 loop in the β-sheet state. Close inspection of the ubiquitin-free and ubiquitin-bound state of Rpn11 revealed that in the ubiquitin-free state Gly77 has phi and psi angles in a region of the Ramachandran plot only accessible to glycine (Figure 3.5A). However, in the ubiquitin-bound state Gly77 adopts phi and psi angles that are accessible to any amino acid and are specifically favorable for proline (Figure 3.5B). Indeed, comparison of the ubiquitin-bound

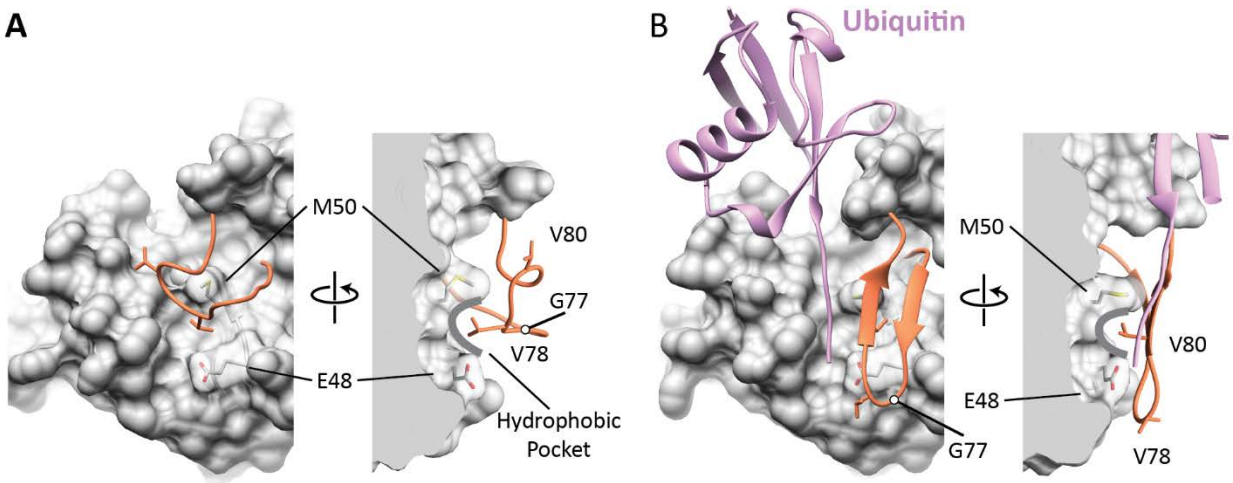

Figure 3.4: Rpn11's Ins-1 loop changes conformation upon Ubiquitin binding
(**A**) Crystal structure of the Rpn11-Rpn8 dimer in the absence of Ubiquitin (PDB 4O8X). The MPN domain of Rpn11 is shown as a gray surface and the Ins-1 loop is shown as an orange ribbon. Met50 and the aliphatic sidechain of Glu48 make a hydrophobic pocket visible through a transparent region of the Rpn11 surface. In the Ubiquitin-free state the sidechain of Val 78 associates within the hydrophobic pocket produced by Met50 and Glu48 and stabilized the Ins-1 loop in the inhibited state. (**B**) Crystal structure of the Ubiquitin-bound Rpn11-Rpn8 complex depicted as in **A**. The Ins-1 loop transitions into a β-sheet in the presence of ubiquitin the sidechain of Val80 replaces Val78 in the hydrophobic pocket. Val78 and Gly77 move down toward the Rpn11 active site and the hairpin turn of the β-sheet.

state of Rpn11 with AMSH-LP shows that AMSH-LP contains a proline at the same position as Gly77 in Rpn11 (Figure 3.5C). Importantly, the Ins-1 loop of AMSH-LP is always a β-sheet even in the absence of ubiquitin. We therefore reasoned that Gly77 might serve as a switch to control the conformation of the Ins-1 loop and allow the enzyme to sense and respond to the presence of a bound ubiquitin. Furthermore, if the dihedral angles occupied by Gly77 control the conformation of the Ins-1 loop, mutating Gly77 to proline would bias the Ins-1 loop to the ubiquitin-bound state by precluding formation of the ubiquitin-free state and stabilizing the conformation of the ubiquitin-bound state.

Initial ubiquitin-AMC (Ub-AMC) cleavage assays revealed that the Rpn11(G77P) mutant was at least 10 fold more active than the WT enzyme (Figure 3.6A). However, limitations in the concentration of commercially available Ub-AMC precluded full titration and determination of the kinetic constants for ubiquitin cleavage. To get around this problem, we engineered a synthetic ubiquitin DUB substrate that could be prepared to very high concentration using traditional biochemical and molecular biology techniques. Our substrate consists of WT ubiquitin with an engineered N terminal tryptophan for quantitation and a C terminal Gly-Cys dipeptide extension. Preparation of the substrate is accomplished by labeling the C terminal cysteine of ubiquitin with tetramethylrhodamine(TAMRA)-maleimide, and DUB activity is monitored through the loss TAMRA polarization due to the cleavage of the peptide bond between Gly76 of ubiquitin and Gly77 in the Gly-Cys C-terminal extension (Figure 3.6B). Although our ubiquitin-GC-TAMRA substrate contains a peptide bond instead of an isopeptide bond, we have previously shown that Rpn11 does not interact with structures on the proximal side of the scissile bond

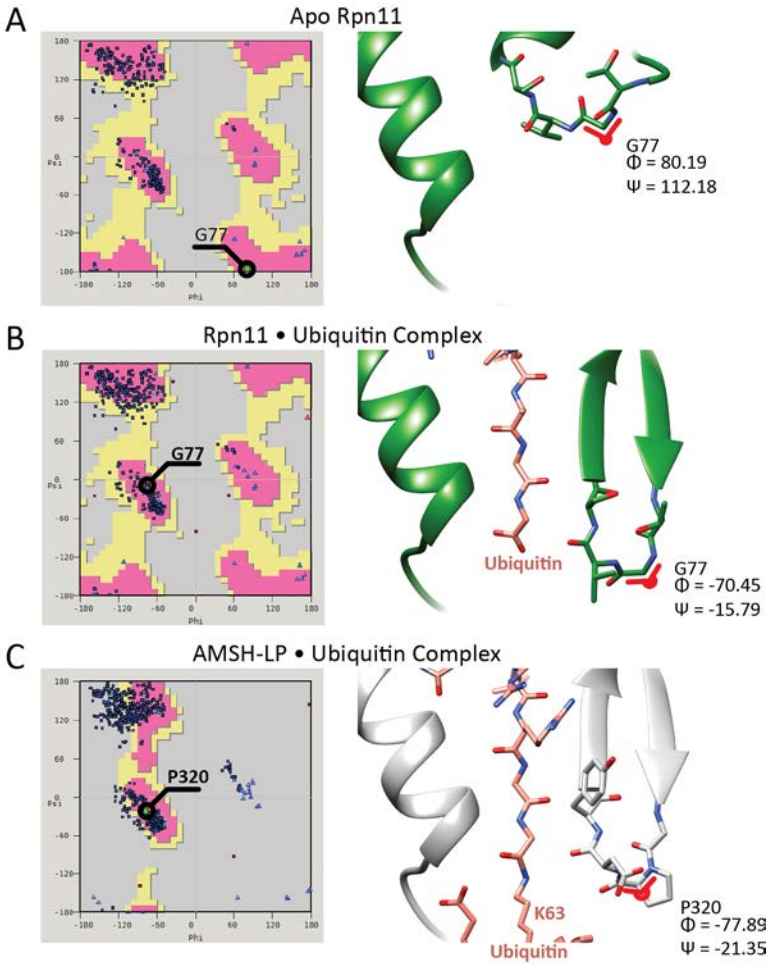

Figure 3.5: The conformation of the Ins-1 loop is controlled by Rpn11 Gly77
(A) Close up view of Rpn11 with its Ins-1 loop it the ubiquitin free state (PDB 4O8X) is shown on the right. A Ramachandran plot the Rpn11 dihedral angels is shown on the left. In the ubiquitin-free state, Rpn11 Gly77 has dihedral angles accessible only to Glycine. (B) Ramachandran plot and close up view of Rpn11's active site depicted as in A, but with the Ins-1 loop in the ubiquitin bound state. The four most C-terminal residues of ubiquitin are colored pink and shown in stick representation. In the ubiquitin-bound state, Gly 77 adopts dihedral angles that would be favorable to proline. (C) The active site of AMSH-LP bound to Lys63-linked diubiquitin (PDB 2ZNV) depicted as in A and B. AMSH-LP Pro320 is in the same position as Rpn11 G77 and also has similar phi and psi angles.

(Worden et al. 2014) and it has been previously shown that Rpn11 is able to remove linear ubiquitin fusions from proteasome substrates (Yao & Cohen 2002).

Using our synthetic DUB substrate, we found that the increase in activity in the Rpn11(G77P) mutant was exclusively due to a 10 fold enhancement in k_{cat} with no change in K_m (Figure 3.6C). The increase in activity of the Rpn11(G77P) mutant was not exclusive to the isolated dimer as lid subcomplexes containing the Rpn11(G77P) were also stimulated by 10 fold over WT lid (Figure 3.6D). Additionally the activity of the Rpn11(G77P) mutant was sensitive to the zinc chelator o-phenanthroline, indicating that the large increase in activity was not due to some other contaminating DUB (data not shown). It therefore seems that the Rpn11(G77P) mutant activates the enzyme by biasing the Ins-1 loop into the active, β-sheet state in the absence of ubiquitin. Our observation that the enhancement in activity in the

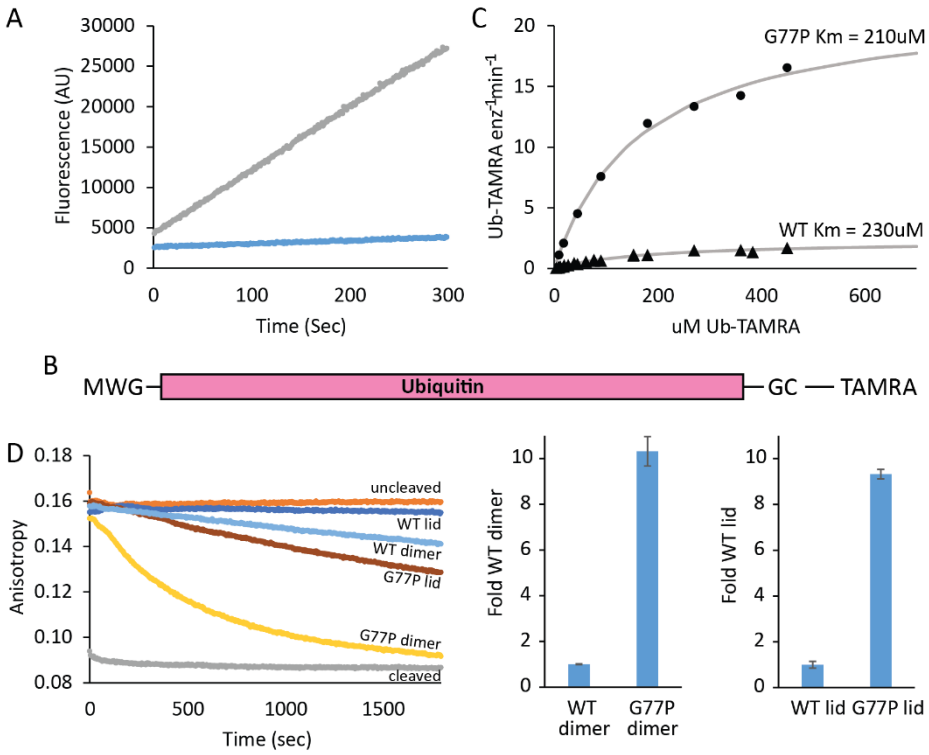

Figure 3.6: Ins-1 loop switching is the rate limiting step for isopeptide bond hydrolysis
(**A**) Ubiquitin-AMC hydrolysis assay showing that the Rpn11(G77P) mutant (gray line) has increased activity over WT Rpn11 (blue line). (**B**) Schematic of the synthetic DUB substrate prepared for Rpn11 titration. An N-terminal Trp was engineered for better protein quantitation by absorbance at 280nm. Rpn11 cleaves the peptide bond between the C terminus of ubiquitin and the Gly-Cys dipeptide extension, releasing the TAMRA dye. (**C**) Michaelis-Menten substrate titrations of WT Rpn11 (black triangles) and Rpn11(G77P) (black circles). WT Rpn11 cleaved the synthetic DUB substrate with a K_m of 230 μM and a k_{cat} of ~3min^{-1}. Rpn11(G77P) cleaved the synthetic substrate with a K_m of 210μM and a k_{cat} of ~30min^{-1}. (**D**) Deubiquitination experiment using the synthetic DUB substrate showing relative rates of cleavage for WT Rpn11 in the heterodimer and the lid and Rpn11(G77P) in the heterodimer and lid (left). Quantification of the data on the left is shown in the bar graphs on the right. Rpn11 containing the G77P mutation is 10 times faster than WT Rpn11 in all complexes tested. Error bars correspond to 1 standard deviation of the data calculated from the average of 3 technical replicates.

Rpn11(G77P) mutant is entirely derived from an increase in k_{cat} with no change in K_m suggests a mechanism where Ins-1 loop switching from the ubiquitin-free state to the ubiquitin-bound state is the rate limiting step in isopeptide bond cleavage. A conformational capture model of ubiquitin binding to Rpn11 is not likely because in this mechanism ubiquitin binding would depend on the Ins-1 loop forming a β-sheet and mutants that stabilize the Ins-1 loop in the β-sheet state would be expected to primarily exhibit effects in K_m. We therefore favor an induced fit mechanism where, in the absence of substrate, Rpn11 exists primarily in the autoinhibited state and ubiquitin binding induces a conformational change to the active, β-sheet state. Importantly, in this model ubiquitin can bind to Rpn11 in either state, but catalysis is limited by the rate of switching from the inhibited to active form (Figure 3.7). This model is in agreement with our observation that the Rpn11(V80A) mutant can still bind to ubiquitin, even though switching to the active state is presumably inhibited

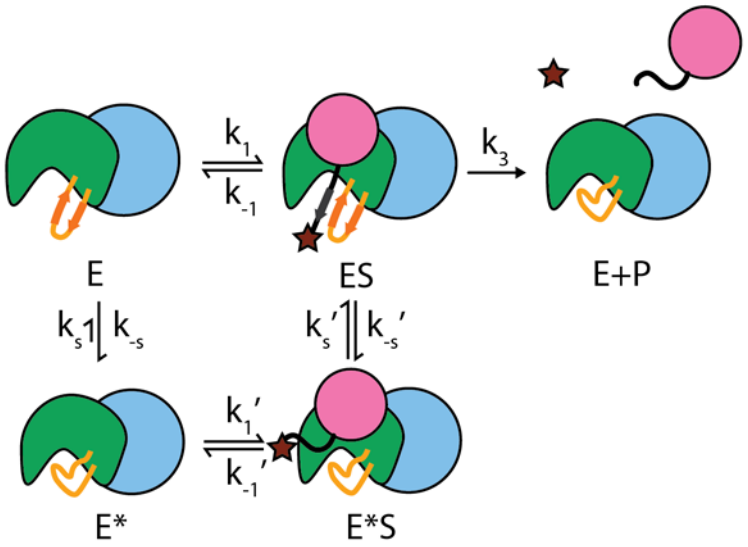

Figure 3.7: Induced fit model of Rpn11 isopeptide bond cleavage
The Rpn11-Rpn8 dimer is depicted as the green and blue cartoon. Ubiquitin is shown as a pink circle and the star represents a moiety on the proximal side of the isopeptide bond. Rpn11 can exist in either the inhibited state (E*) or the active state (E). Ins-1 loop switching between E* and E is slow it the absence of ubiquitin (denoted by the short arrow k_s). Ubiquitin can bind to Rpn11 in either the E* or E states, and ubiquitin binding to the E* state biases Rpn11 to switch into the E (denoted with the longer arrow k_s') state where catalysis occurs.

(Worden et al. 2014) and that biasing the Ins-1 loop toward the active, β-sheet, state in the Rpn11(G77P) mutant accelerated k_{cat}, but did not affect K_m.

Together these data suggest that the activity of Rpn11 toward ubiquitin substrates is directly controlled by the switching behavior of the Ins-1 loop between inhibited and active states.

3.2.4 Substrate deubiquitination is not the rate limiting step of proteasomal degradation

Because the very slow k_{cat} of Rpn11 seems to correlate well with *in vitro* proteasome degradation rates, we had previously suggested that deubiquitination by Rpn11 may be the rate limiting step of substrate degradation by the 26S proteasome (Worden et al. 2014). However, because mutant proteasomes deficient in Rpn11 deubiquitination activity do not degrade substrates we could not directly test if deubiquitination by Rpn11 was rate limiting. Identification of the highly activating Rpn11(G77P) mutation provided an experimental basis to probe Rpn11's kinetic contributions to degradation by the proteasome.

If deubiquitination by Rpn11 is rate limiting for degradation by the proteasome, increasing the rate of deubiquitination would be expected to increase the rate of degradation. Using a GFP substrate with only a single lysine sidechain we found that proteasomes reconstituted with mutant Rpn11(G77P) lid did not degrade GFP faster than WT proteasomes (Figure 3.8A). In fact Rpn11(G77P) proteasomes seemed to exhibit a small degradation defect relative to WT. Many proteasome substrates are ubiquitinated at multiple lysines and thus contain multiple ubiquitin chains that must be removed by Rpn11 before

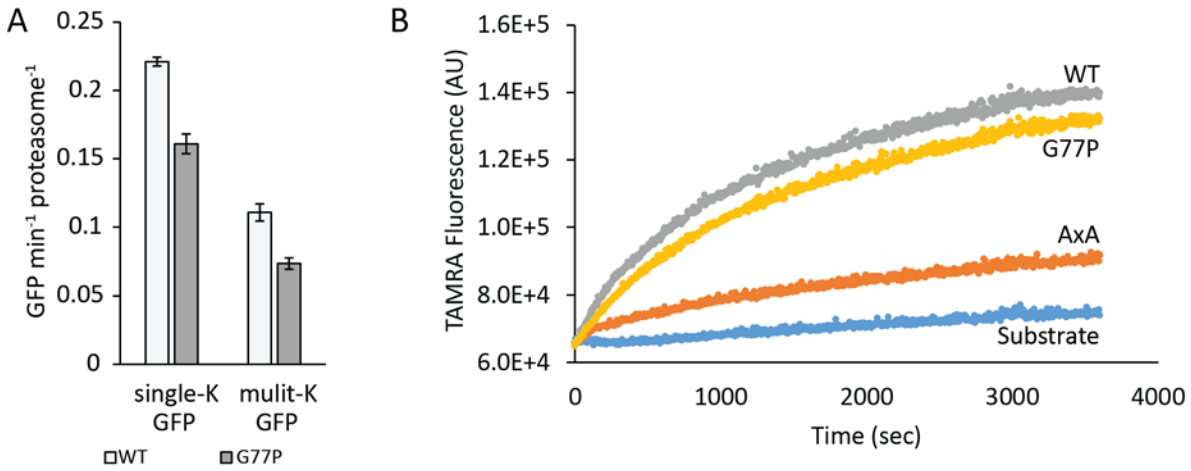

Figure 3.8: Deubiquitination by Rpn11 is not the rate liming step of degradation
(**A**) Single lysine and multiple lysine proteasome degradation assay conducted under saturating substrate concentration. Proteasomes reconstituted with the Rpn11(G77P) mutation do not degrade substrates faster than WT. Error bars correspond to on standard deviation of the data (n=3) (**B**) FRET-based G3P substrate degradation experiment where deubiquitination was monitored by the increase of fluorescence of the substrate-labeled TAMRA donor dye over time. No difference is apparent between WT and Rpn11(G77P) proteasomes. Proteasomes lacking DUB activity due to a catalytically dead Rpn11 (AxA) were used as a control.

complete degradation. Therefore, it is possible that deubiquitination by Rpn11 may not be rate limiting in degradation of substrates with only a single ubiquitin chain, but could become rate limiting if the enzyme must go through multiple rounds of deubiquitination. To test if deubiquitination is rate limiting for the degradation of substrates with multiple ubiquitin chains, we reconstituted Rpn11(G77P) and WT proteasomes and degraded a GFP substrate that contained many lysines and multiple ubiquitin chains. The multiple chain GFP substrate was degraded more slowly than the single chain version, but as with the single chain GFP substrate, we observed no increase in degradation rate in the Rpn11(G77P) mutant proteasomes (Figure 3.8A).

To eliminate any effects that may be unique to our GFP substrates or that arise as a result of monitoring GFP unfolding as a proxy for degradation, we assessed the degradation of a small model substrate constructed from the N terminal domain of the gene 3 protein (G3P) using a direct FRET-based assay for deubiquitination by Rpn11 (Bashore et al. 2015). Rpn11(G77P) proteasomes did not deubiquitinate the G3P substrate faster than WT, even though the Rpn11(G77P) mutation has a 10 fold higher catalytic rate in isolation (Figure 3.8B). Our biochemical data thus show that, at least for substrates with few ubiquitin chains attached, deubiquitination by Rpn11 in the proteasome context is not rate limiting for protein degradation.

3.2.5 Rpn11 activation is coupled to translocation

Measured rates of deubiquitination by Rpn11 range between 0.3-1.0 min^{-1} and are similar to measured rates of *in vitro* degradation by the proteasome (Worden et al. 2014). The similarity between the rate Rpn11 isopeptide bond cleavage and proteasome degradation is what originally led us to believe that deubiquitination was the rate limiting

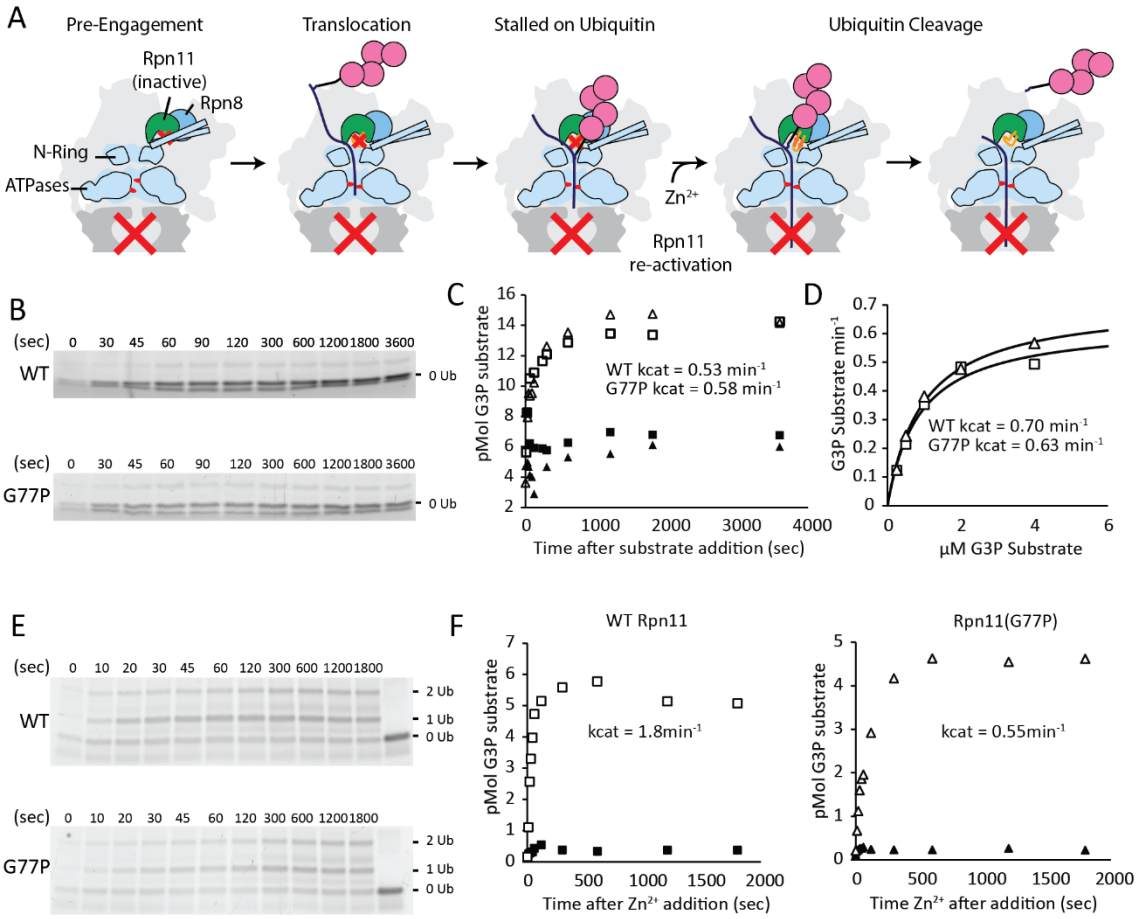

Figure 3 9: Co-translocational deubiquitination by Rpn11
(**A**) Experimental protocol for monitoring the co-translocational DUB activity of Rpn11. Proteasomes were reconstituted with the core particle and Rpn11 inhibited (red x). Substrates were incubated with the inhibited proteasomes and stalled on the ubiquitin chain. Synchronous initiation of deubiquitination by Rpn11 was accomplished by adding Zn^{2+} to the stalled proteasomes and accumulation of deubiquitinated substrate was monitored by SDS-PAGE. (**B**) Fluorescence scan of a single turnover reaction with a TAMRA-labeled G3P substrate as depicted in **A**, but where Rpn11 was reactivated prior to the addition of substrate so no stalled complex was formed. Deubiquitinated substrate can be seen accumulating over time. (**C**) Quantified data in **B** and fit to a single exponential. WT proteasomes deubiquitinated the substrate with a rate constant of $0.53min^{-1}$ (white squares) and Rpn11 G77P proteasomes deubiquitinated substrate with a rate constant of $0.58min^{-1}$ (white triangle). Mock experiments where no Zn^{2+} was added did not accumulate deubiquitinated substrate (WT = black square, G77P =black triangle). (**D**) Michaelis-Menten titration of WT and Rpn11(G77P) proteasomes using the same substrate as in **B** and **C**. Values for k_{cat} agree well with the rate constants calculated in **C**. Rates of degradation were calculated by the loss of fluorescence polarization of the substrate-label TAMRA dye. (**E**) Fluorescence scan of the TAMRA-labeled substrate as in **B**, but where a ubiquitin substrate was stalled as depicted in **A**. Mono- and di-ubiquitin species of the substrate accumulate over time after the synchronous initiation of Rpn11 DUB cleavage. (**F**) Quantified data for the mono-ubiquitinated species in **E**. Substrate accumulation was fit to a single exponential. WT proteasomes (white squares) deubiquitinated the G3P substrate with a rate constant of $1.8min^{-1}$ and Rpn11(G77P) proteasomes (white triangles) deubiquitinated the substrate with a rate constant of $0.55min^{-1}$. Mock experiments did not accumulate any deubiquitinated substrate (black squares and black triangles).

step of degradation. However, our observation that deubiquitination is not the rate limiting step raises the interesting prospect that the rate of isopeptide bond cleavage during

substrate degradation in the proteasome may be significantly accelerated. To assess the rate of Rpn11 activity in the context of a translocating polypeptide it is necessary to isolate the deubiquitination step of substrate degradation from other slower steps. To accomplish this, we developed a protocol to reversibly inhibit and reactivate Rpn11 in the proteasome context using the zinc chelator o-phenantroline and $ZnCl_2$, respectively (Figure 3.9A). With Rpn11 inhibited, the ubiquitin chain on a translocating substrate cannot be removed and translocation of the substrate stalls. Proteasomes with the substrate stalled on the ubiquitin chain have already progressed through substrate binding, engagement and translocation, and have the isopeptide bond positioned in front of Rpn11 ready for cleavage. Thus, substrates accumulate at the point of deubiquitination and are ready for action by Rpn11. The rate of deubiquitination by Rpn11 can then be determined by adding Zn^{2+}, releasing o-phenantholine from the Rpn11 active site, and quantifying the exponential appearance of deubiquitinated substrate.

To assess the rate of Rpn11 cleavage on a translocating proteasome substrate, we reconstituted WT and Rpn11(G77P) proteasomes with epoxomicin-treated core particle. Epoxomicin treatment allows deubiquitinated substrates to pass through the proteasome without being degraded, and can then be analyzed by SDS-PAGE (Verma 2002). Single turnover deubiquitination of a TAMRA-labeled G3P substrate that was never stalled by inhibition of Rpn11 showed the accumulation of deubiquitinated substrate which appeared with a rate constant of k = 0.6-0.5min^{-1} in both WT and mutant proteasomes (Figure 3.9B, C). The rate of 0.6-0.5min^{-1} agrees very well with the k_{cat} of degradation measured for the same substrate in multiple turnover conditions (Figure 3.9D). However, substrates that were pre-stalled by o-phenanthroline showed very little accumulation of completely deubiquitinated substrate after reactivation of Rpn11. Instead, a ladder of mono-ubiquitinated and diubiquitinated products accumulated, indicating that during the incubation period the base ATPases were able to unfold the first and to a lesser degree, the second ubiquitin, allowing Rpn11 to cut the isopeptide bond between ubiquitins in a chain (Figure 3.9E). Quantification of the appearance of mono-ubiquitinated substrate species yielded rate constants of 1.8min^{-1} and 0.55min^{-1} for WT and Rpn11(G77P) proteasomes respectively. The deubiquitination rate of 1.8min^{-1} seen for WT Rpn11 is significantly faster than rates of 1.0-0.3min^{-1} usually seen for free Rpn11, indicating that the proteasome is likely able to significantly accelerate the DUB cleavage rate of Rpn11 (Figure 3.9F). Additionally, because the mono-ubiquitinated substrate arises from non-ideal cleavage between the first and second ubiquitin in a chain, the 1.8min^{-1} cleavage rate probably represents a lower bound of the rate of co-translocational deubiquitination by Rpn11. The slower rate observed for Rpn11(G77P) proteasomes is puzzling, but it may indicate that efficient Rpn11 activation by the proteasome requires that the ubiquitin chain must first encounter Rpn11 with its Ins-1 loop in the auto inhibited state, which is strongly stabilized when the proteasome engages a substrate (Matyskiela et al. 2013) and strongly precluded in the G77P mutant.

How does the proteasome activate Rpn11 for isopeptide bond cleavage? The position of Rpn11 in the proteasome directly over the central translocation channel with its Ins-1 loop in the inhibited state suggests that translocation by the base may have some effect. We envision that when a ubiquitin chain attached to a translocating substrate encounters Rpn11,

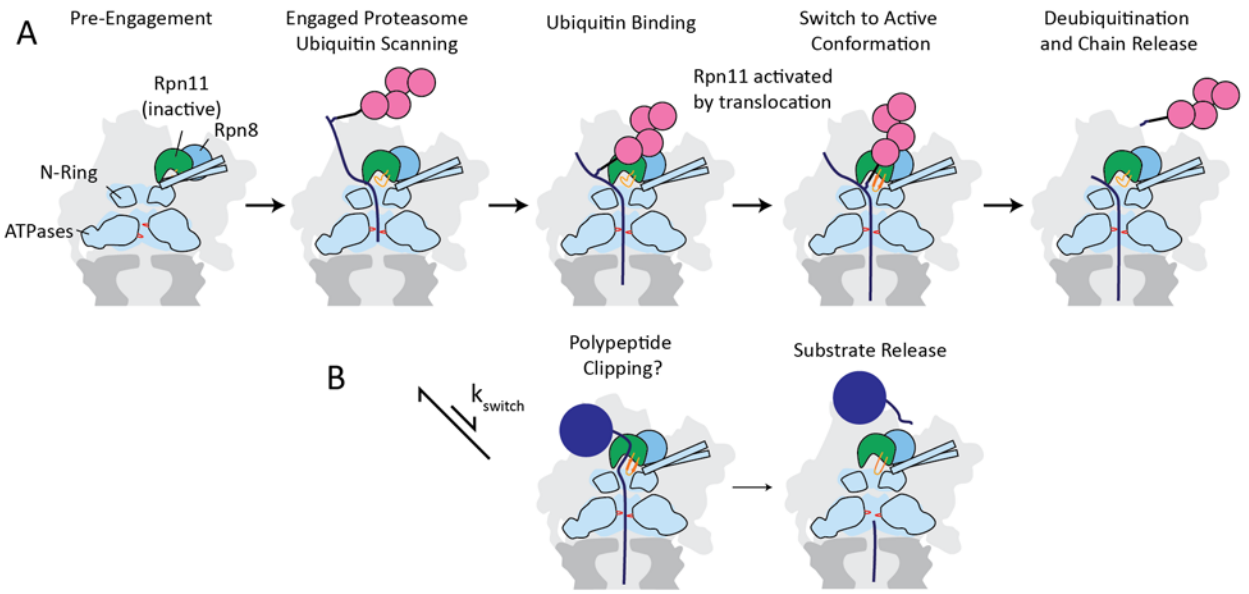

Figure 3.10: Model for co-translocational deubiquitination by Rpn11
(**A**) Model for substrate deubiquitination in the proteasome context. During degradation a ubiquitin is pulled toward Rpn11, which has its Ins-1 loop in the auto inhibited conformation. When ubiquitin binds to Rpn11, translocation by the base can accelerate the transition of the Ins-1 loop from the inhibited to the active state, thereby activating Rpn11 for cleavage. (**B**) Premature activation of Rpn11 my lead to polypeptide chain clipping and premature substrate release.

the first ubiquitin in the chain binds within Rpn11's ubiquitin binding cleft while the Ins-1 loop is in the auto inhibited state (Figure 3.10A). The geometry of a ubiquitin-bound Rpn11 with its Ins-1 loop in the inhibited state would be ideal to link translocation by the base to isopeptide bond cleavage by Rpn11. Because the rate limiting step of isopeptide bond cleavage by Rpn11 is the conformational switch of the Ins-1 loop from the inhibited state to the β-sheet state, translocation by the base would pull the C terminus of an Rpn11-bound ubiquitin downward toward the active site. This downward pulling by the base likely accelerates Ins-1 switching from the inhibited state to the active state, thereby accelerating Rpn11 cleavage activity.

3.3 Conclusions

Our structural and biochemical data have revealed that isopeptide bond cleavage by Rpn11 is a highly regulated process. Rpn11's Ins-1 loop changes conformation from an auto inhibited state where it blocks the catalytic groove of Rpn11 to an active state where it forms a β-sheet with the C terminus of a bound ubiquitin. The conformational change from the inhibited to active state is the rate limiting step in deubiquitination by Rpn11 and mutations within the Ins-1 loop that greatly affect the activity of Rpn11 likely do so by either accelerating or slowing down the rate of switching from one state to the other. Additionally it appears that translocation by the base ATPases may accelerate deubiquitination by physically pulling the substrate-attached ubiquitin C-terminus against the Ins-1 loop and accelerating its transition to the active state. It is still puzzling why the Ins-1 loop of Rpn11 is stabilized in the inhibited state when the proteasome is actively degrading a substrate,

because Rpn11's position within the proteasome should limit off pathway deubiquitination and one would expect Rpn11 to have maximal activity when it is scanning for ubiquitin modifications on a substrate. It is tempting to speculate that having Rpn11 inhibited when the proteasome engages substrate may act as a mechanism to reduce cleavage of the translocating polypeptide chain (Figure 3.10B). It has been known for many years that Rpn11 can cut peptide bonds (Yao & Cohen 2002) and we have shown previously that Rpn11 is promiscuous in its isopeptide bond cleavage (Worden et al. 2014). Furthermore, Rpn11's position above the translocation channel is optimal not only for ubiquitin removal, but also for hydrolysis of translocating peptides. Thus, if Rpn11 was not inhibited, it could constitute a seventh protease site in the proteasome whose activity would lead to substrate clipping and premature termination of degradation. It therefore seems that the gymnastics executed by Rpn11 during substrate deubiquitination allow the enzyme to be exquisitely sensitive to the presence of ubiquitin that is attached to a translocating substrate. The enzyme then, only becomes fully active at the exact moment of deubiquitination.

3.4 Materials and methods

3.4.1 Protein purification

Preparation of the Rpn11-Rpn8 crystallization construct. Rpn8(1-179) was cloned into the second MCS of pETDuet-1 using NdeI and AatII and PreScission-Rpn11(24-160-GGSGSG-192-221) was cloned, in frame, behind the His tag of the first MCS of the plasmid containing Rpn8(1-179) using BamHI and SacI. The resulting construct (pEW106) contained IPTG inducible genes for 6xHis-PreScission-Rpn11(24-160-GGSGSG-192-221) and Rpn8(1-179). For protein expression Bl21-star (DE3) E. coli cells (thermofisher) containing the plasmid were grown in 3L of Terrific Broth at 37°C. When the cell density reached OD=1.5 the groth temperature was reduced to 18°C and at OD=2.0 1mM IPTG was added and protein expression carried out overnight. The next day cells were harvested by centrifugation and resuspended in 20 ml of lysis buffer per liter of culture (60mM HEPES pH8.0, 100mM NaCl, 100mM KCl, 10mM MgCl2, 25mM Imidazole, 10% glycerol). After resuspension, 2mg/ml lysozyme, protease inhibitors (PMSF, Leupeptin, Pepstatin) and benzonase DNAse were added and the cell pellet was frozen at -80°C. On the day of the purification the resuspended pellet was thawed at 25°C. All subsequent purification steps were performed at 4°C. The thawed lysate was sonicated on ice and clarified by centrifugation at 16,000 rpm in a Sorvall SA-600 rotor. Clarified lysate was bound in batch for 45 min to 8ml of Ni-NTA affinity resin that was pre-equilibrated with lysis buffer. The resin was then washed 3 times with 50 ml of lysis buffer and then applied to a gravity flow column where it was washed with another 70 ml of lysis buffer. Protein was eluted in 20 ml of lysis buffer + 250mM imidazole and 40µl of 1M DTT was added directly to the eluate. The N terminal his tag on Rpn11 was removed by reaction with PreScission protease overnight at 4°C. The next day the eluate was concentrated to 2 ml in a 30,000 MWCO Amicon Ultra spin concentrator (Millipore). The concentrated eluate was filtered through a 0.22µm spin filter and injected onto a Superdex 200 16/60 that was pre-equilibrated with GF buffer (60mM HEPES pH8.0, 100mM NaCl, 100mM KCl, 10% glycerol) + 0.5mM DTT for size exclusion (GE). Peak fractions were

concentrated to ~1mM in a 30,000 MWCO spin concentrator and the concentration was determined by absorbance at 280nM. The concentrated protein was then aliquoted, flash frozen in LN2 stored at -80°C.

Purification of the Rpn11-Rpn8 heterodimer used for biochemical assays. Purification of the Rpn11-Rpn8 dimer that contained Ins-2 and the N-terminus of Rpn11 was conducted as described previously (Worden et al. 2014).

Purification of core particle. Purification of core particle was conducted as described previously (Li et al. 2015) with some modifications. Yeast strain yAM16 (PRE1-3XFLAG-6xHis) was grown in 6L of YPD for 3 days or until saturation. Cells were pelleted, weighed and resuspended in a small amount of CP lysis buffer (60mM HEPES pH 7.6, 500mM NaCl, 100mM KCl, 0.05% NP-40). After lysis by cryogrinding, the cell powder was thawed at RT and 25°C yeast buffer was added, bringing the volume of buffer up to 1.5 ml of buffer per gram of cell paste. Thawed lysate was clarified by centrifugation at 16,000 rmp in a SA-600 rotor (Sorvall) and the supernatant was bound in batch to 5ml of M2 anti-FLAG affinity resin (Sigma). After binding, flag resin was washed in batch 2x times with 50ml CP lysis buffer and then applied to a gravity flow column and washed with approximately 5 CV of CP buffer (60mM HEPES pH 7.6, 500mM NaCl, 100mM KCl). Core was eluted with 10mlof CP buffer + 0.15mg/ml 3xFLAG peptide. 10µl of 1M DTT was added directly to the eluate and stored overnight on ice. The next day the DTT was removed by repeated concentration and dilution in CP buffer and any contaminating DUBs were inhibited by reacting the concentrated FLAG elution with 5uM ubiquitin vinyl sulfone at 25°C for 3 hours. After DUB inhibition, the core elution was concentrated to 500µl and injected onto a superose 6 size exclusion column (GE) pre-equilibrated with GF buffer. Peak fractions were pooled and concentrated in a 100K MWCO Amicon Ultra concentrator (Millipore) and the concentration of core was determined by absorbance at 280nm. The concentrated core was then aliquoted, flash frozen in LN2 and stored at -80°C.

Purification of other proteins. Purification of the heterologous base and multiple lysine GFP proteasome substrate (Beckwith et al. 2013), heterologous lid and Rpn10 (Lander et al. 2012), single lysine GFP and G3P proteasome substrates (Bashore et al. 2015), ubiquitin and ubiquitin variants (Worden et al. 2014) were all conducted as previously described.

3.4.2 Preparation of the synthetic ubiquitin substrate

The synthetic ubiquitin substrate was cloned into pET28a (pEW145), expressed and purified following the same protocol described previously for WT ubiquitin (Worden et al. 2014). However, during expression approximately one third of the ubiquitin substrate has its C terminal Gly-Cys dipeptide removed by a cryptic *E. coli* protease. Isolation of the full length protein was accomplished by utilizing the C terminal cysteine residue for covalent chromatography on activated thiol sepharose 4B resin (GE) following the manufacturer's instructions. Mass spec confirmed the removal of the truncated species. The purified ubiquitin substrate was buffer exchanged into labeling buffer (50mM HEPES pH7, 150mM NaCl, 1mM TCEP) by repeated concentration and dilution and labeled for three hours at 25°C with tetramethylrhodamine-5(and-6) C2 maleimide (Anaspec) in a 5-to-1 molar ratio of dye-to-protein. The reaction was quenched by the addition of 50mM DTT and the excess dye was

separated from the ubiquitin by size exclusion on a superdex 75 16/60 (GE) pre-equilibrated with GF buffer. Peak fractions of labeled ubiquitin were concentrated, aliquoted, flash-frozen in liquid Nitrogen and stored at -80°C. The concentration of the substrate was determined using a quantitative peptide analysis service provided by Alphalyse (Palo Alto). Mass spec on the final labeled protein confirmed >95% labeling efficiency.

3.4.3 Rpn11 fluorescence polarization deubiquitination assays

Michaelis-Meten titrations of Rpn11-containing complexes. 2x stocks of WT Rpn11-Rpn8 (1μM) and Rpn11(G77P)-Rpn8 (500nM) were prepared in GF buffer + 0.5mM TCEP. 2x stocks of each concentration (5-500μM) of ubiquitin-GC-TAMRA were prepared in GF buffer + TCEP. Reactions were initiated by mixing 5μl of the 2x enzyme stock with 5μl of the 2x substrate stocks in a 384 well flat bottom, low volume, microplate (Corning). The change in polarization was measured at 30°C over the course of an hour in a Synergy NEO2 multimode plate reader (Biotek). Rates of cleavage by Rpn11 were determined using the change in FP for each substrate concentration calculated from the difference between the uncleaved substrate and an endpoint for completely cleaved ubiquitin-GC-TAMRA determined after 20-min incubation with 100 nM of the DUB Yuh1. *Km* and k_{cat} values were determined by fitting the initial rates of cleavage directly to the Michaelis-Menten equation (Matlab).

3.4.4 Proteasome degradation assays

Degradation of GFP substrates. 12μl of 200nM doubly-capped proteasome reactions were prepared at 25°C using 200nM core particle, 500nM heterologous base, 1μM heterologous lid and 1.5μM Rpn10 in reconstitution buffer (60mM HEPES pH 7.6, 100mM NaCl, 100mM KCl, 10mM $MgCl_2$, 1mM TCEP, 1mM ATP) supplemented with an ATP regeneration system (creatine phosphate + creatine kinase). Reactions were initiated by the addition of 2μM ubiquitinated GFP substrate and 10μl of the reaction was added to a 384 well flat bottom, low volume, microplate (Corning) and degradation was read out over the course of an hour by the loss of GFP fluorescence over time using a Synergy NEO2 multimode plate reader (Biotek).

FRET-based G3P substrate deubiquitination/degradation assay. 12μl of 100nM doubly-capped proteasome reactions were prepared at 25°C using 100nM core particle, 500nM heterologous base, 1μM heterologous lid and 1.5μM Rpn10 in reconstitution buffer supplemented with an ATP regeneration system (creatine phosphate + creatine kinase). Reactions were initiated by the addition of 1.5uM TAMRA-labeled G3P substrate that was ubiquitinated with Cy5-ubiquitin that was labeled on an engineered N terminal cysteine with Cy5-maleimide. The close proximity of the TAMRA-dye on the G3P substrate to the Cy5-labeled ubiquitin chain allowed FRET between the TAMRA and Cy5. Removal of the ubiquitin chain by Rpn11 could be monitored as an increase in TAMRA donor dye fluorescence. Reactions were added to a 384 well flat bottom, low volume, microplate (Corning) and deubiquitination was read out over the course of an hour at 30°C by the increase of TAMRA fluorescence over time using a Synergy NEO2 multimode plate reader (Biotek). Rates of

ubiquitin removal were determined using an estimate of the endpoint after the one hour degradation.

Fluorescence polarization based G3P substrate titration. 2x stocks of 100nM doubly-capped reconstituted proteasome were prepared at 25°C by mixing 100nM core particle, 500nM heterologous base, 750nM heterologous lid and 1μM Rpn10 in reconstitution buffer supplemented with a 2x concentration of an ATP regeneration system (creatine phosphate + creatine kinase). 2x stocks of TAMRA-labeled G3P substrate (8μM, 4μM, 2μM, 1μM, 0.5μM) ubiquitinated with WT ubiquitin were prepared. Degradation was initiated by mixing 5μl of the 2x proteasome and 5μl of the 2x substrate in a 384 well flat bottom, low volume, microplate (Corning). Degradation was monitored at 25°C by the loss of polarization of the TAMRA dye over time. Rates of degradation were determined using the change in FP calculated from the difference between the undegraded substrate and an endpoint for completely degraded substrate determined after a 2hour Incubation with 100nM WT proteasome. K_m and k_{cat} values were determined by fitting the initial rates of degradation directly to the Michaelis-Menten equation (Matlab).

3.4.5 Co-translocational deubiquitination assay

All reactions were done at 25°C. 750nM doubly-capped proteasome reactions were reconstituted by mixing 750nM epoxomicin treated core, 1.5μM base, 1.5μM lid and 1.5μM Rpn10 in reconstitution buffer supplemented with an ATP regeneration system (creatine phosphate + creatine kinase). Reversible inhibition of Rpn11 was achieved by the addition of 3mM o-phenanthroline. For the control reaction where substrate was not stalled, Rpn11 was reactivated prior to substrate addition by the adding 1mM ZnCl2. Mock treatment consisted of adding buffer containing no zinc. After Rpn11 was reactivated, 150nM TAMRA-labeled G3P substrate was added and 1.8μl timepoints were taken for SDS-PAGE analysis. For the reactions where substrates were stalled prior to Rpn11 activation, 150nM substrate was added to the phenanthroline inhibited proteasome and incubated for 30min. After the 30min incubation either 1mM $ZnCl_2$ was added (for the test) or buffer was added (for the mock treatment). After the addition of $ZnCl_2$, 1.8μl timepoints were taken for SDS-PAGE analysis. Samples were separated on AnyKD™ precast polyacrylamide gels (Bio-Rad) and imaged on a typhoon variable mode scanner (GE) using a pixel density of 100μm per pixel. Bands were quantified using ImageQuant (GE) and rate constants for appearance of deubiquitinated substrate were determined by fitting to a single exponential (matlab).

3.4.6 X-ray crystallography

The Rpn11(24-160-GGSGSG-192-221) Rpn8(1-179) heterodimer was buffer exchanged into crystallization buffer (10mM HEPES pH 7.6, 50mM NaCl, 1mM TCEP) using a Micro Bio-Spin 6 chromatography column (Bio-Rad). 5mg/ml Rpn11-Rpn8 dimer was mixed with ubiquitin at 1:1, 1:2 and 1:3 molar ratios. Initial crystallization screens were performed at 18°C with the sitting drop diffusion method using the Intelli-plate system (ARI). A Mosquito liquid-handling robot (TTP Labtech) was used to set 400nl crystallization drops using 200nl of protein and 200nl of precipitant from the sparse matrix crystal screens

JCSG+ (Qiagen), Wizard I and II (Emerald Bio), Index I and II (Hampton Research) and Crystal Screen I and II (Hampton Research). After 1 week crystals appeared in the Index I screen in a well containing 1.1M Ammonium Tartrate pH 7.0. Crystals were harvested directly from the sparse matrix screen using 2M ammonium Tartrate pH 7.0 as a cryo protectant and a 3.1 Å dataset was collected at the ALS beamline 8.3.1 (Lawrence Berkeley National Laboratory). Our initial hit was optimized in 96well intelli-plates at 18°C and ideal conditions for growth were found to be 400nl drops of 200nl 5mg/ml Rpn11-Rpn8 dimer in a 1:1.5 molar ratio with WT ubiquitin mixed with 200nl of 1.5M ammonium tartrate pH 6.8. A 2.7Å (CC1/2 = 0.15 at 2.7Å) dataset was collected at ALS beamline 8.3.1 using a wavelength of 1.1159Å from crystals grown in this condition using mother liquor + 30% ethylene glycol as a cryo protectant. The dataset was processed using XDS (Kabsch 2010) and solved by molecular replacement using Phenix (Adams et al. 2010). The structure the ubiquitin-free Rpn11-Rpn8 dimer (PDB:4O8X) was used as a search model for the ubiquitin-bound Rpn11-Rpn8 dimer. Because we anticipated some conformational rearrangement of the Ins-1 loop in the ubiquitin-bound state, the Ins-1 loop in the ubiquitin-free Rpn11 search model was removed. A poly alanine model of ubiquitin 1-72 was generated from PDB 2ZNV chain B and used as a search model for ubiquitin. Immediately after molecular replacement density for the ubiquitin C-terminus and the Ins-1 loop in a β-sheet conformation was clearly visible. After initial rigid body, group ADP and TLS refinement, the poly- alanine model of ubiquitin was replaced with the high resolution model of ubiquitin from PDB 2ZNV Chain B. Because the density for ubiquitin was poor, all subsequent refinements utilized the high resolution model of ubiquitin from 2ZNV as a reference model. The model of Rpn11·ubiquitin-Rpn8 was corrected and built in Coot (Emsley & Cowtan 2004) and refined to an R-free of 0.25. During refinement, we collected a higher resolution dataset (CC1/2 = 0.15 at 2.3Å) of the Rpn11·ubiquitin-Rpn8 crystal by using mother liquor + 20% ethylene glycol and 5% PEG 8k as a cryo protectant. R_{free} flags from our 2.7Å dataset were copied and extended to the higher resolution dataset and a resolution cutoff of 2.5Å (CC1/2 = 0.5) was chosen using the Phenix reflection file editor (Adams et al. 2010). We then used the Rpn11·ubiquitin-Rpn8 structure as a search model for the higher resolution dataset. To help de-bias our structural model, the first two rounds of refinement included simulated annealing in addition to individual ADP, TLS and minimization. To improve stereochemistry and clashscore, the model was refined using a riding hydrogen model (Adams et al. 2010). Our final model exhibits good stereo chemistry and was refined to an R_{free} = 0.235.

4. Structure of the proteasome lid reveals the mechanism of Rpn11 inhibition

A portion of the work presented in this chapter has been previously published as part of the following paper: Dambacher, C.M., Worden, E.J., Herzik, M.A., Martin, A. and Lander, G.C. Atomic structure of the 26S proteasome lid reveals the mechanism of deubiquitinase inhibition. Elife. 5:1-17, 2016.

4.1 Introduction

The eukaryotic 26S proteasome is a large multi-enzyme complex that functions as the primary degradation machinery for the selective turnover of aberrant or unneeded proteins within the cell. Proteins targeted for degradation are covalently labeled with polyubiquitin chains, which are recognized and removed by the proteasome(Finley 2009). The barrel-shaped core peptidase complex of the proteasome, which sequesters the proteolytic active sites in an internal chamber(Groll et al. 1997), is capped on one or both ends by a regulatory particle that acts as a discriminating gateway for targeted protein substrates(Saeki et al. 2012). The regulatory particle consists of two sub-complexes, known as the 'base' and the 'lid' (Glickman et al. 1998). The base sub-complex contains the AAA+ ATPases Rpt1-Rpt6, which form a heterohexameric ring that drives the mechanical substrate unfolding and translocation of the unstructured polypeptides into the degradation chamber of the core peptidase. Docked on one side of the base is the lid subcomplex, which contains the deubiquitinating enzyme (DUB) Rpn11 that cleaves polyubiquitin chains from targeted substrates as an essential step in proteasomal substrate processing(Boehringer et al. 2012).

The lid is an asymmetric, ~370 kDa complex that consists of 9 unique subunits (Rpn3, 5, 6, 7, 8, 9, 11, 12, Sem1) and exhibits a characteristic hand-shaped organization similar to that of the eukaryotic initiation factor 3 (eIF3) and the COP9 signalosome (CSN) (Lander et al. 2012; Lingaraju et al. 2014; des Georges et al. 2015). At the center of the lid, six **P**roteasome-**C**SN-e**I**F3 (PCI)-domain containing subunits (Rpn3, 5, 6, 7, 9, 12) interact via their winged-helix motifs to form a horseshoe-shaped scaffold. The amino-terminal domains of these 6 subunits extend radially like fingers from the central PCI horseshoe. The essential deubiquitinase Rpn11 is positioned in the 'palm' of the hand-shaped lid. Rpn11 is an (MPN)-domain containing metalloprotease of the JAMM family and forms a heterodimer with an enzymatically inactive MPN-subunit, Rpn8. With the exception of Sem1, a small 87-residue subunit located at the interface of the N-terminal domains of Rpn3 and Rpn7 (Bohn et al. 2013), all lid subunits contain conserved C-terminal helices that assemble into a large bundle positioned next to the MPN heterodimer of Rpn11/Rpn8 in the palm of the complex (Beck et al. 2012).

Previous crystallographic and biochemical studies have focused on the mechanism of Rpn11, which acts as a highly promiscuous DUB to remove ubiquitins from the wide variety of substrates during their translocation into the proteasome, likely by cleaving the isopeptide bond between the substrate lysine and the first ubiquitin moiety of the attached ubiquitin chain (Worden et al. 2014; Pathare et al. 2014). The Rpn11/Rpn8 heterodimer is

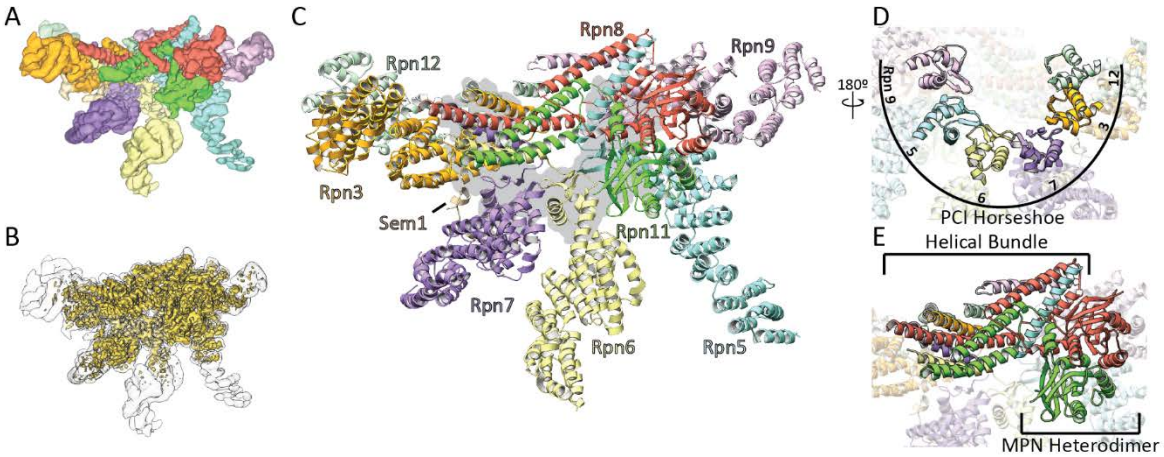

Figure 4.1: Architecture of the isolated proteasome lid sub-complex
(**A**) The segmented 3.5 Å resolution cryo-EM density is shown at a low isocontour level, with each subunit colored differently. Rpn3 is shown in orange, Rpn5 in light blue, Rpn6 in yellow, Rpn7 in purple, Rpn8 in red, Rpn9 in magenta, Rpn11 in green, Rpn12 in light green, and Sem1 in tan. This coloring scheme is maintained throughout all figures. (**B**) The unsegmented cryoEM density is shown at a higher isocontour level (in gold) to demonstrate the molecular details observable in the reconstruction (~3Å in certain regions). The lower isocontour level used for the segmented map is overlaid as a silhouette. (**C**) The atomic model of the proteasome lid is depicted using a ribbon representation, with each subunit colored according to the segmentation shown in A. The central location of the six PCI domains is illustrated by a gray shadow underneath the structure. (**D**) The PCI domains form a horseshoe, held together by an 18-stranded β-sheet. (**E**) Close-up of the helical bundle and the MPN heterodimer.

active in isolation (Worden et al. 2014), but is significantly inhibited in the context of the lid sub-complex and regains robust DUB activity in the assembled 26S proteasome (Verma 2002; Yao & Cohen 2002). The isolated Rpn11/Rpn8 heterodimer is not present at considerable levels in the cell, whereas the presence of the lid and its assembly intermediates containing Rpn11/Rpn8 have been previously observed and characterized (Tomko & Hochstrasser 2011). The inhibition of Rpn11 activity in the isolated lid and its assembly intermediates might therefore be important to prevent spurious deubiquitination of proteins in the cell, given the high promiscuity of this DUB. It has been suggested that interactions with Rpn5 are possibly involved in Rpn11 inhibition in the isolated lid (Lander et al. 2012), but the specifics of this regulation and the mechanism by which Rpn11 is activated upon incorporation into the holoenzyme remain elusive (Verma 2002; Yao & Cohen 2002; Lander et al. 2012).

Here, we present an atomic model of the isolated lid sub-complex of the yeast proteasome, as determined by cryo-electron microscopy (cryoEM) (Figure 4.1, Figure 4.2, Table 4.1), revealing the molecular mechanism for direct inhibition of the DUB active site, as well as Rpn11 activation through extensive conformational changes that occur during lid incorporation into the 26S holoenzyme.

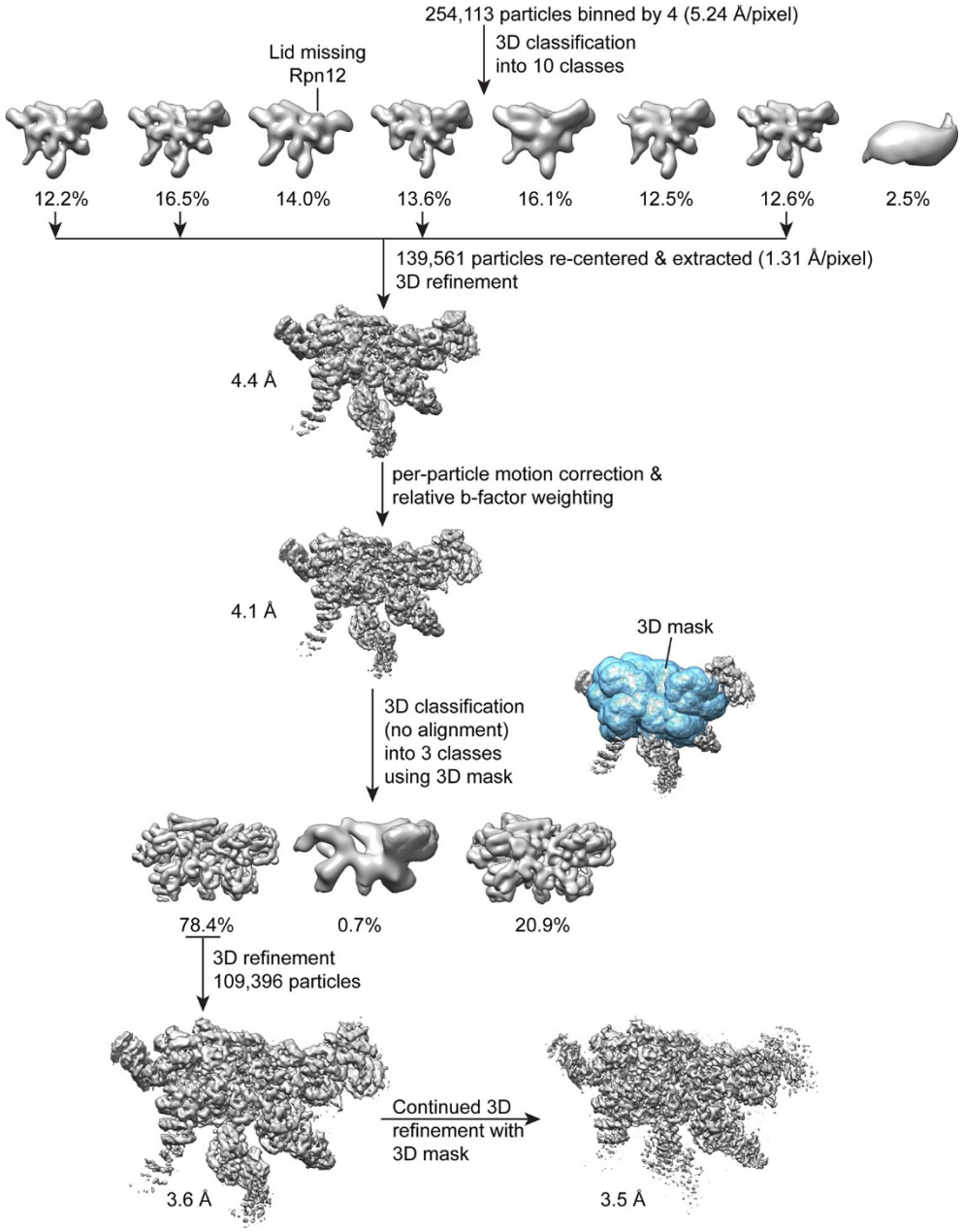

Figure 4.2: Single particle analysis of the lid complex
A total of 254,113 particles were extracted from micrographs, scaled by a factor of 0.25, and subjected to 3D classification into 8 classes in RELION. The particle coordinates corresponding to the four highest resolution classes that showed density for all lid components were re-centered, based on the translations determined from 3D classification. These coordinates were used to extract 139,561 unbinned particles for 3D refinement with RELION, which yielded a reconstruction of 4.4 Å. After correcting for particle motion and electron beam damage (particle polishing), the resolution was improved to 4.1 Å. A 3D mask surrounding the most structurally stable regions of the map (the PCI domains, the MPN heterodimer, and the helical bundle) was generated, and used in an alignment-free 3D classification of the data into 3 classes. The 109,396 particles contributing to the highest resolution 3D class were used for further 3D refinement in RELION without applying a mask, yielding a 3.6 Å structure. Continued refinement of these alignment parameters using the same 3D mask that was applied earlier improved the resolution of the central regions of the structure by 0.1 Å.

4.2 Results

4.2.1 Lid architecture

Our cryo-EM reconstruction of the isolated lid shows that the MPN heterodimer, PCI horseshoe, and helical bundle together comprise a rigid substructure that contains regions resolved to ~3 Å resolution (Figure 4.1B, Figure 4.3). The N-terminal portions of the PCI-domain containing subunits progressively decrease in resolution as they extend toward the periphery of the complex, likely due to intrinsic flexibility (Figure 4.3). The 3D reconstructions of the fully assembled lid and the lid lacking Rpn12 (Figure 4.2, top row, third reconstruction) show that the N-terminal portions of Rpn6 and Rpn5 are fully extended, and the MPN heterodimer and helical bundle adopt identical orientations in both structures. These findings contradict a recent crosslinking study (Tomko et al. 2015) suggesting that incorporation of Rpn12 during lid assembly induces a large-scale rearrangement of the MPN dimer and the transition of the N-terminal portion of Rpn6 from an inward-folded state to an extended conformation that allows binding to the base. Further structural studies will therefore be required to better understand how Rpn12 incorporation affects lid binding to the base and core subcomplexes.

We found that the six PCI winged-helix domains associate into a continuous 18-stranded β-sheet, forming an incomplete right-handed spiral at the center of the lid sub-complex (Figure 4.1D). This organization was also observed in the crystal structure of CSN, although the PCI horseshoe assembly of the isolated lid has a wider and steeper spiral (Figure 4.4). Recently, a similar succession of β-strands was shown for the PCI domains in eIF3 (des Georges et al. 2015), but its domain organization is significantly more open and deviates from the spiral configuration observed in the proteasome lid and CSN (Figure 4.4). The significant conformational differences between the horseshoes of the lid, CSN, and eIF3 indicate that the PCI-domain assembly allows for substantial flexibility, while simultaneously serving as an organizational scaffold at the center of the complex.

The C-terminal helices of all lid subunits (except Sem1) assemble into a well-defined helical bundle that is centrally positioned within the lid sub-complex, adjacent to the PCI horseshoe and the MPN heterodimer (Figure 4.1E). Our cryoEM reconstruction contains sufficient structural detail to generate a complete atomic model of this helical bundle, providing an accurate depiction of the extensive inter-helical interactions. Furthermore, we were able to precisely assign the register of several helices that could not be unambiguously positioned in earlier lower-resolution models of this bundle (Beck et al. 2012; Unverdorben et al. 2014; Estrin et al. 2013). Our structure shows that Rpn8 and Rpn11 are the only subunits that contribute multiple helices to the bundle and together contact all other subunits within the helical assembly. Notably, Rpn8 is the largest contributor to the bundle, which is consistent with previous biochemical work showing that the Rpn8 C-terminal helices are more critical for lid assembly than those of other subunits (Estrin et al. 2013). The PCI horseshoe and MPN heterodimer are individually tethered to the bundle via short loops, but make only few direct surface contacts with the bundle.

The cryoEM reconstruction of the isolated lid allowed us to examine the structural elements involved in regulating Rpn11 DUB activity. Notably, within the isolated lid, the

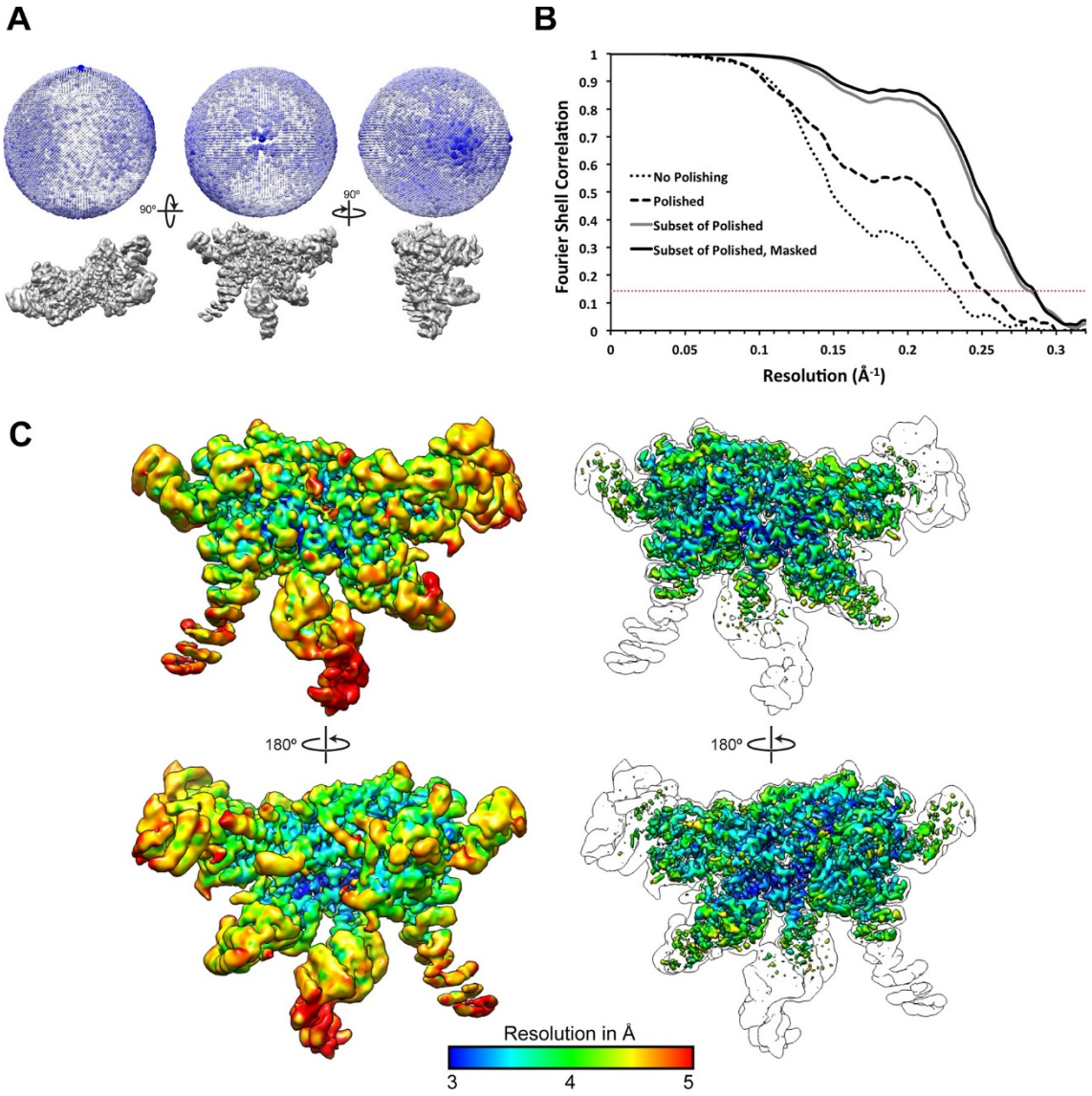

Figure 4 3: Resolution assessment of the reconstructions
(**A**) 3D angular distribution plot, shown from three orthogonal angles of the reconstruction. The diameter and color saturation of the spheres increases with occupancy of particles at a given Euler angle. (B) Fourier Shell Correlation plots of lid reconstructions at different stages of processing. (C) The final map is shown at two contour levels, colored according to a local resolution estimation using Bsoft. A lower contour level (left) shows the more disordered regions, while the higher contour level (right) shows that regions of the map were resolved to 3 Å resolution. An outline of the lower contour is overlaid on top of the images on the right for reference.

Rpn11/Rpn8 heterodimer is positioned in a previously unobserved orientation relative to the other subunits, stably associated within the palm of the hand-shaped complex via two primary interfaces with the TPR domain of Rpn5 and the α-solenoid of Rpn9 (Figure 4.5). The resulting organization produces the basis for Rpn11 DUB inhibition in the isolated lid.

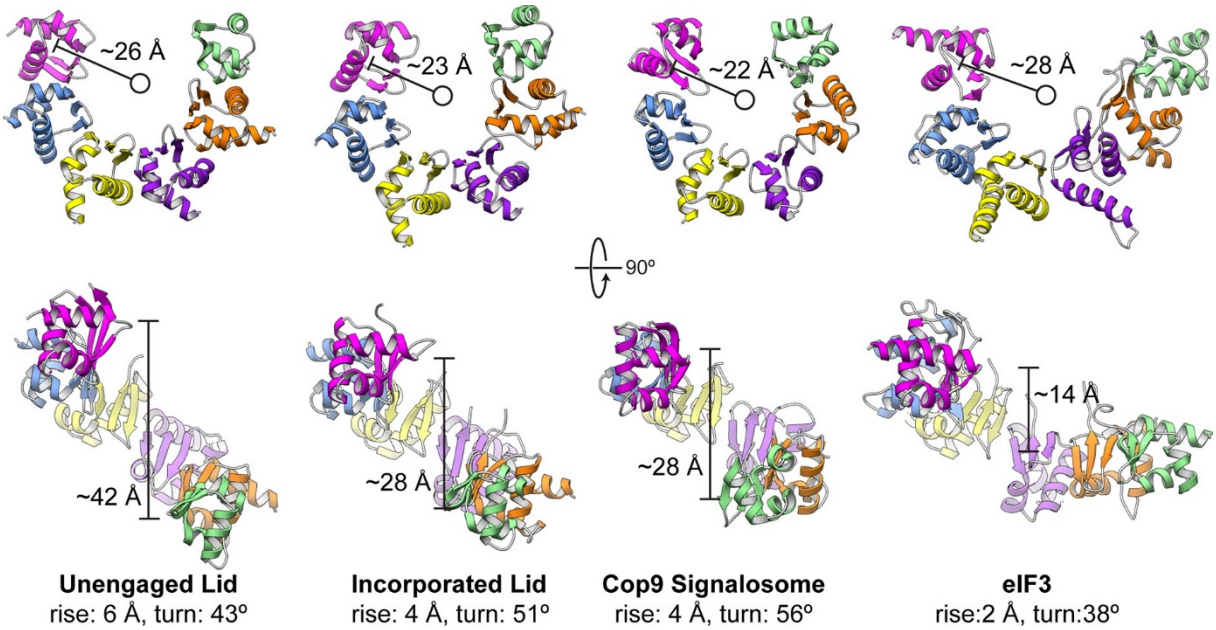

Figure 4.4: Comparison of PCI horseshoes in different complexes
Shown are ribbon representations of the PCI horseshoes of (from left to right) the unincorporated lid, the incorporated lid (PDB ID: 4CR2), the COP9 signalosome (PDB ID: 4D18), and eIF3 (PDB ID: 5A5T). The PCI horseshoes all adopt a staircase arrangement, and the pseudo-helical pitch for each horseshoe was determined, as well as the radius of the helix. The PCI horseshoe in the unincorporated lid complex (left) is more open, and less planar than that of the incorporated lid. The helical parameters and diameter of the PCI horseshoe in the incorporated lid closely resembles that of the COP9 Signalosome. Of the four PCI horseshoes, the arrangement of eIF3 is most open and least helical in arrangement.

4.2.2 Rpn5 occludes the Rpn11 active site

We first probed the contacts between Rpn11 and Rpn5 for their contributions to Rpn11 inhibition in the isolated lid, as this interface is more extensive (total buried surface area of ~630 Å^2) than all other subunit interactions with the MPN heterodimer. Importantly, the N-terminal region of α-helix 13 in Rpn5 (residues 275–285) is nestled against the end of Rpn11's catalytic groove, with several residues from Rpn5 directly contacting loops that surround Rpn11's catalytic Zn^{2+} ion (Figure 4.5C). To test the functional importance of these contacts, we generated Rpn5-mutated lid variants and compared their ubiquitin-7-amino-4-methylcoumarin (Ub-AMC) cleavage rate with that of wild-type lid and the isolated Rpn11/Rpn8 dimer. Under our assay conditions, Rpn11 activity within the isolated lid is 5-fold lower compared to the free Rpn11/Rpn8 dimer. In the loop preceding α-helix 13 of Rpn5, Tyr273 is in an orientation that enables hydrophobic interactions with Rpn11 Phe114, located in a loop near the active site (Figure 4.5C). Mutation of this Rpn5 residue (Y273A) increased Rpn11 activity to 61% of the isolated Rpn11/Rpn8 dimer (Figure 4.5D-E), suggesting that Tyr273 aids in stabilizing Rpn11 in its inhibited conformation.

Rpn5 residues His282 and Lys283 directly interact with the backbone atoms of two loops near the Rpn11 active site, and their substitution with alanine increased Rpn11 activity to 31% and 41% of the free MPN heterodimer, respectively (Figure 4.5C, E). The effects of these mutations were additive, as the Rpn5 (H282A,K283A) double-mutant lid exhibited

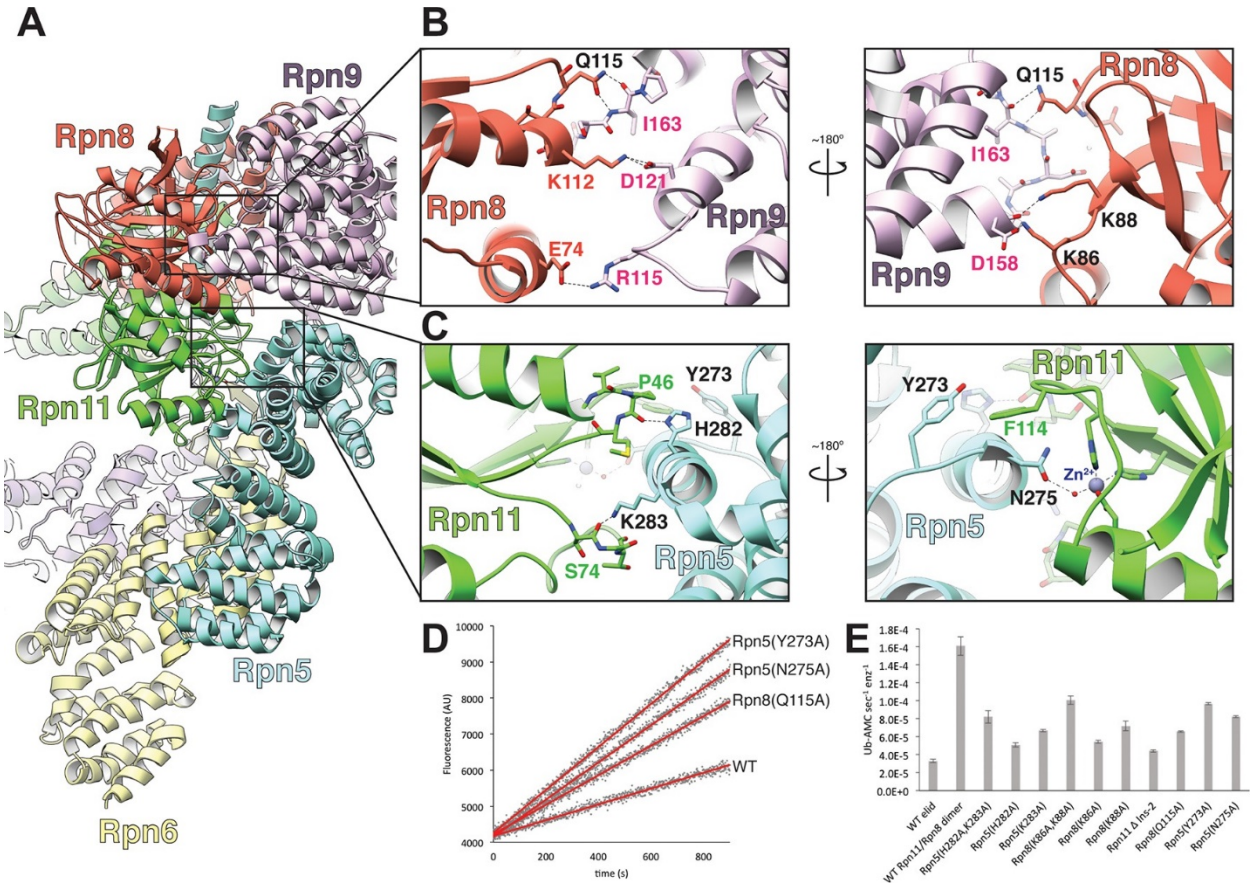

Figure 4 5: The MPN heterodimer interacts extensively with Rpn5 and Rpn9
(**A**) Side view of the lid sub-complex shows that the MPN heterodimer (Rpn8 in red, Rpn11 in green) interacts closely with the Rpn5 (blue) and Rpn9 (lavender) subunits. Side-chain interactions likely responsible for maintaining the MPN heterodimer in this configuration are shown in detail in panels (**B**) and (**C**). Residues that were mutated to alanine for deubiquitination assays are labeled in black. (**D**) Measurements of fluorescence increase upon Rpn11-mediated cleavage of ubiquitin-AMC are shown for three lid mutants relative to the wild-type lid. (**E**) Ubiquitin-AMC cleavage rates show activation of Rpn11 in the lid upon mutation of residues within Rpn5 and Rpn8.

51% DUB activity compared to the free MPN heterodimer (Figure 4.5E). Structural analysis of the lid containing the Rpn5 (Y273A) or the Rpn5 (H282A,K283A) double-mutant by negative-stain EM shows that the Rpn11/Rpn8 heterodimer is released from its inhibitory conformation, while the overall organization of the PCI-containing subunits is identical to that of the isolated wild-type lid complex (Figure 4.6). Together, these activating mutations support a model wherein Tyr273, His282, and Lys283 of Rpn5 all stabilize the association of α-helix 13 with the Rpn11 active site, generating a structural barrier that blocks substrates from accessing the catalytic groove.

In addition to preventing access to the Rpn11 active site by steric occlusion, the close proximity of Rpn5 in the isolated lid further blocks DUB activity through interaction with the catalytic Zn^{2+} (Figure 4.7). Two histidines (His109 and His111) and an aspartate (Asp112) coordinate the Zn^{2+} within the Rpn11 active site, a configuration that is preserved in all JAMM metalloenzymes (Komander et al. 2009). This geometry allows for interaction with a fourth ligand, as Zn^{2+} is usually tetrahedrally coordinated in proteins. Despite the close

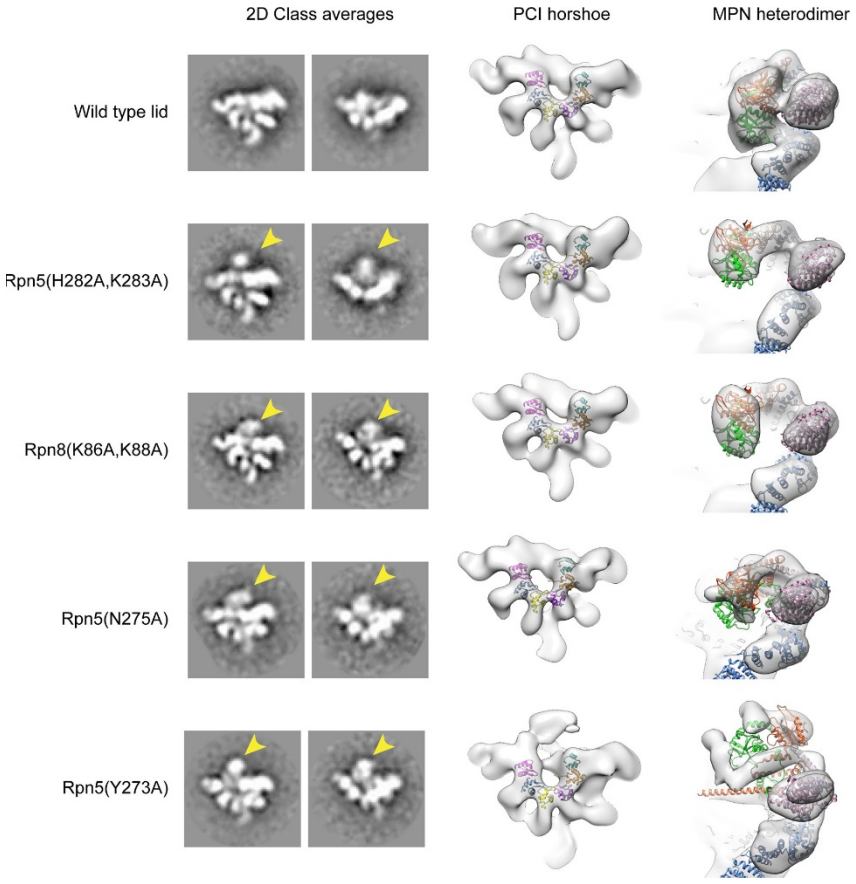

Figure 4.6 Mutations in Rpn5 and Rpn9 release the dimer from its inhibited state:
Negative stain EM analysis was performed on the lid mutants. On the left are 2D class averages depicting the canonical hand-shaped arrangement of the lid sub-complex from the front and top views. On the right are 3D reconstructions of the lid, showing the organization of the PCI horseshoe, as well as the position of the Rpn11/Rpn8 heterodimer (red and green) relative to Rpn9 (pink) and Rpn5 (blue). The 2D and 3D analyses of the wild type particles show that the MPN heterodimer is closely associated with the Rpn5 and Rpn9 subunits (top row). The mutants, however, show that the while overall organization of the PCI-containing subunits are preserved, the MPN dimer is released from its position in the palm of the lid sub-complex. In the 2D class averages, the detached MPN dimer can be identified as an additional density that is not observed in the WT class average (indicated by a yellow arrow). In the 3D reconstructions, the WT structure shows the MPN dimer (green and red) are connected to Rpn5 (blue) and Rpn9 (purple). The density corresponding to the dimer in all the mutants is clearly detached from Rpn5 and Rpn9. The MPN dimer within the Rpn5 (Y273A) (bottom row) had such an increased level of flexibility, that the dimer itself is poorly resolved.

proximity of Rpn5's α-helix 13 to the Rpn11 active site, intermolecular distances preclude direct interaction of any Rpn5 residues with the catalytic Zn^{2+}. The Rpn5 residue that is closest to the zinc is Asn275, which is notably oriented with its carboxamide group directed towards the Rpn11 active site. Mutation of Asn275 to alanine increases Rpn11 DUB activity in the isolated lid to 51% of the isolated MPN heterodimer (Figure 4.5E), and negative-stain EM of this lid mutant shows the Rpn11/Rpn8 heterodimer detached from its inhibited conformation (Figure 4.6).

Although Rpn5 Asn275 is not within range to directly bind the catalytic Zn^{2+}(~5 Å from the Zn^{2+} to Nδ1 of Asn275), the cryo-EM density in the Rpn11 active site shows connectivity

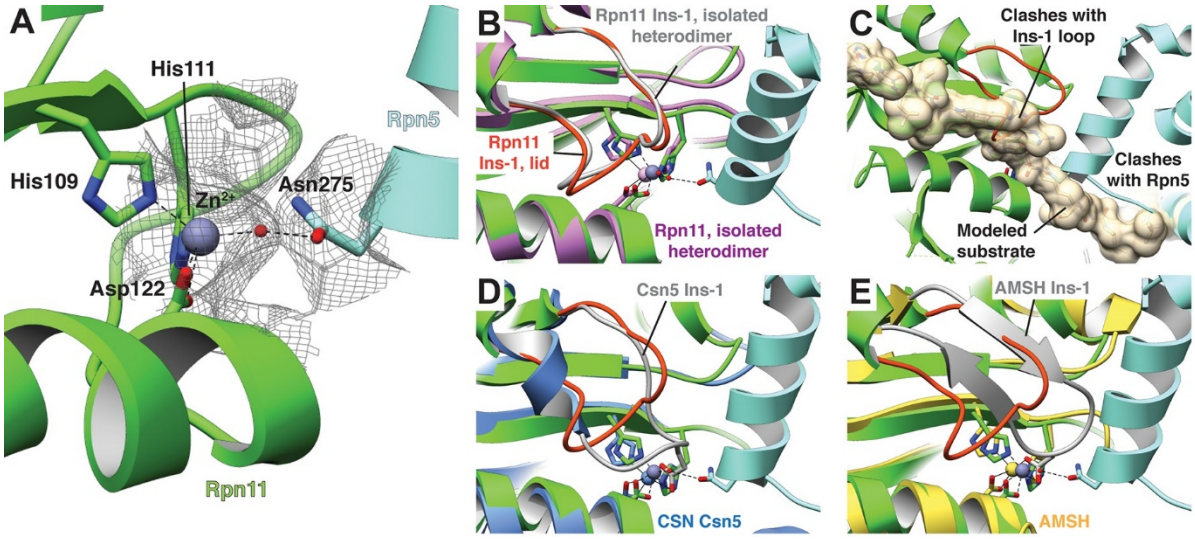

Figure 4.7: The Rpn11 active site is inhibited in the isolated lid
(**A**) The catalytic Zn^{2+} (gray sphere) within the Rpn11 active site (green ribbon) is coordinated by three residues from Rpn11, and a water molecule acts as a fourth ligand, likely mediated by Asn275 from the neighboring Rpn5 subunit (blue). The cryoEM density in this region is shown as a mesh. (**B**) Comparison of the Rpn11 active sites from the isolated Rpn11/Rpn8 heterodimer crystal structure (PDB ID: 4O8X, purple) and isolated lid (green) shows that the two structures are nearly superimposable. (**C**) A di-ubiquitin substrate (tan) was modeled into the active site and shown as a transparent surface rendering. The modeled substrate severely clashes with the locked Rpn11 Ins-1 loop and Rpn5. (**D**) In CSN, a Glu within the Ins-1 loop provides a fourth point of coordination for the Zn^{2+} ion. (**E**) Similar to CSN, an AMSH mutant utilizes an Asp from the Ins-1 loop to establish tetrahedral coordination of the catalytic Zn^{2+}.

between Asn275 and the catalytic Zn^{2+} (Figure 4.7A), potentially corresponding to a coordinated water molecule. Indeed, a Zn-associated water molecule is known to play a key role in the peptide hydrolysis mechanism of Zn-dependent proteases and has been observed in the crystal structures of Rpn11 (Worden et al. 2014; Pathare et al. 2014) and related DUBs of the JAMM family, such as AMSH (Shrestha et al. 2014; Davies et al. 2011). Furthermore, the co-crystal structure of the AMSH ortholog Sst2 bound to a post-cleavage ubiquitin fragment shows that the carboxylate of ubiquitin Gly76 forms a hydrogen bond with the catalytic water (Shrestha et al. 2014) in the same manner as Rpn5 Asn275 in the isolated lid. While the Sst2 structure presents a snapshot of the transient substrate cleavage product prior to its departure from the active site, the positioning of Rpn5 Asn275 establishes a stable tetrahedral coordination of the Zn^{2+} ion via this catalytic water molecule, inhibiting isopeptidase activity of Rpn11 in the isolated lid sub-complex.

4.2.3 Rpn9 stabilizes the inhibited MPN heterodimer

The other major interface involved in stabilizing the DUB-inhibited conformation of the isolated lid is found between Rpn8 and Rpn9, and involves a 5-residue loop connecting α-helix 8 (residues 143–159) and α-helix 9 (residues 165–182) of Rpn9. While the buried surface area of this interface (~450 $Å^2$) is smaller than the Rpn5-Rpn11 interface (Figure 4.5), mutagenesis of the interface residues shows that these contacts also contribute

significantly to maintaining the sequestered position of the MPN heterodimer within the palm of the isolated lid sub-complex.

Our atomic model suggests that Rpn8 Gln115 interacts with the backbone atoms of Rpn9 Ile163 (Figure 4.5), and upon mutation of Gln115 to alanine, we observed elevated Rpn11 activity that was 33% of isolated MPN levels. Furthermore, two lysine residues in Rpn8, Lys86 and Lys88, are likely involved in electrostatic interactions with Rpn9 Asp158, which is located at the C-terminal end of α-helix 8 (Figure 4.5B). Mutation of Lys86 and Lys88 to alanine in Rpn8 of the isolated lid increases Rpn11 activity to 33% and 45% of the free MPN-heterodimer levels, respectively. The double mutant Rpn8 (K86A,K88A) was additive, stimulating Rpn11 activity to about 60% of the isolated MPN heterodimer. As with the Rpn5 (H282A,K283A) double mutant lid, negative-stain analysis of the Rpn8 (K86A,K88A) double mutant revealed that disruption of the Rpn8-Rpn9 interface releases the MPN dimer from its inhibited conformation (Figure 4.6).

Combined with the structural data, our mutational analyses of the MPN-dimer contacts with Rpn5 and Rpn9 suggest that DUB inhibition requires establishment of a finely tuned network of interactions and perturbation of this system at any of the identified contact points disrupts the inhibitory conformation of the MPN dimer within the isolated lid sub-complex.

4.2.4 The Ins-1 loop is locked in an inhibited conformation

Common structural motifs present in many members of the MPN family are the two insertion loops, Ins-1 and Ins-2, which have been suggested to be involved in orienting ubiquitin chains for cleavage (Sato et al. 2008). In Rpn11, Ins-1 is required for catalysis and has been proposed to play a structural role in DUB activity by engaging and positioning the C-terminus of the ubiquitin substrate for hydrolysis (Worden et al. 2014). Flexibility of this loop suggests that it may regulate access to the DUB active site by switching between different conformational states. Upon ubiquitin binding to Rpn11, the Ins-1 loop may first open up to allow the ubiquitin C-terminus to enter the catalytic groove and then switch to a conformation that stabilizes the isopeptide bond for hydrolysis. Structures of the isolated Rpn11/Rpn8 dimer show the Ins-1 loop in a 'closed' conformation (Worden et al. 2014; Pathare et al. 2014), which is also observed in EM reconstructions of proteasomes that are actively processing a protein substrate (Unverdorben et al. 2014; Matyskiela et al. 2013). Interestingly, in the context of the isolated lid, the Ins-1 loop appears to be locked in this closed state through interactions with the neighboring Rpn5 subunit (Figure 4.5C, Figure 4.7B). In particular, the amino group of Rpn5 Lys283 interacts with the Ser74 carbonyl of Ins-1 (Figure 4.5C), and introducing the Rpn5 K283A mutation in the isolated lid results in a significant increase in Rpn11 DUB activity, as indicated above.

While the Ins-1 loop in the free Rpn11/Rpn8 heterodimer exhibited markedly elevated B-values (Worden et al. 2014; Pathare et al. 2014), the Rpn11 Ins-1 loop within the isolated lid has lower B-values than the average for all modeled Rpn11 atoms (Figure 4.8). These data suggest that the Ins-1 loop is locked in a closed conformation through contact with neighboring residues and is unable to switch to the 'open' state required for substrate access to the active site. The combined effects of the tetrahedral coordination of the catalytic Zn^{2+} by

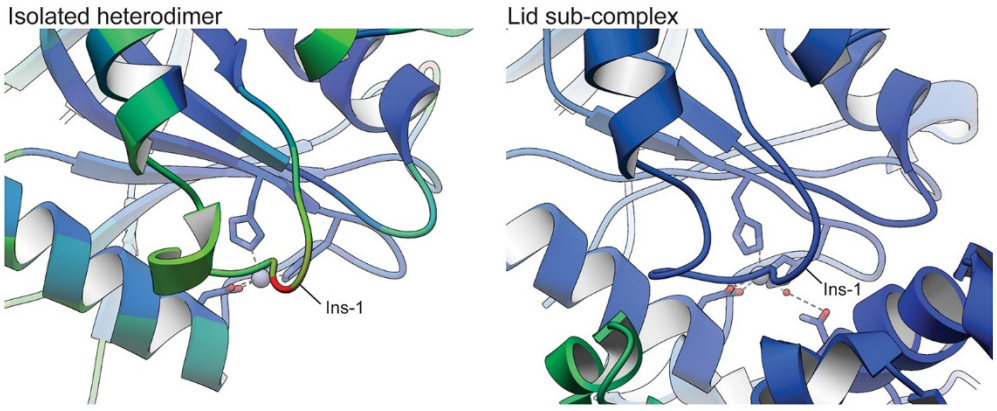

	Mean	Min	Max	Mean	Min	Max
Rpn11 B-factor (Å²)	36.0	17.4	100.0	91.8	64.5	127.0
Ins-1 Loop B-factor (Å²)	52.8	24.0	98.0	83.9	78.0	98.1

Figure 4.8: B-values of the Ins-1 loop in the heterodimer and lid sub-complex
A ribbon representation of the Rpn11 Ins-1 loop in the crystal structure of the isolated Rpn11/Rpn8 heterodimer and within the isolated lid sub-complex is colored according to the B-factor values (blue = low B-factor, red = high B-value). Notably, the Ins-1 loop in the isolated MPN heterodimer has significantly higher average B-values than the rest of Rpn11, while the B-values of the Ins-1 loop in the cryo-EM structure of the lid sub-complex are slightly lower than the average B-factor value of the Rpn11 subunit. This suggests that the Ins-1 loop is stabilized in this conformation within the lid assembly.

Asn275 (Figure 4.7), the steric hindrance imposed by Rpn5's α-helix 13 in the Rpn11 catalytic groove (Figure 4.5), and the obstruction of the DUB active site by the Ins-1 loop result in robust DUB inhibition.

Interestingly, the proposed mechanism for auto-inhibition of the catalytically active MPN subunit in CSN, Csn5, also involves tetrahedral coordination of the active-site Zn^{2+}. However, the fourth ligand in Csn5 is not provided by a neighboring subunit, but intramolecularly by the Ins-1 loop that thereby gets stabilized in a closed conformation (Lingaraju et al. 2014) (Figure 4.7D). A similar scenario is also observed for a mutant AMSH construct (PDB ID: 3RZV) that utilizes a nearby Asp within the Ins-1 loop to complete the tetrahedral geometry (Shrestha et al. 2014) (Figure4.7E).

4.2.5 Incorporation of the lid into the 26S holoenzyme

Upon incorporation into the 26S proteasome, the lid undergoes major conformational changes that involve the PCI-assembly, the helical bundle, and especially the MPN heterodimer. To visualize these rearrangements, we compared the atomic coordinates of the isolated lid sub-complex to the previously determined pseudo-atomic model of the lid in the context of the assembled proteasome (PDB ID: 4CR2) (Unverdorben et al. 2014) (Figure 4.9). Lid binding to the base and core sub-complexes causes the PCI horseshoe to constrict, decreasing in radius by ~3 Å, and adopt a more planar conformation that closely resembles the reported architecture of the CSN (Lingaraju et al. 2014) (Figure 4.9, Figure 4.4). As a result, Rpn3, Rpn7 and Rpn12, comprising one half of the PCI horseshoe, undergo considerable rotation toward the center of the regulatory particle, where Rpn3 and Rpn12 bind the scaffolding subunit Rpn2, while Rpn7 contacts the AAA+ ATPase subunits Rpt3 and

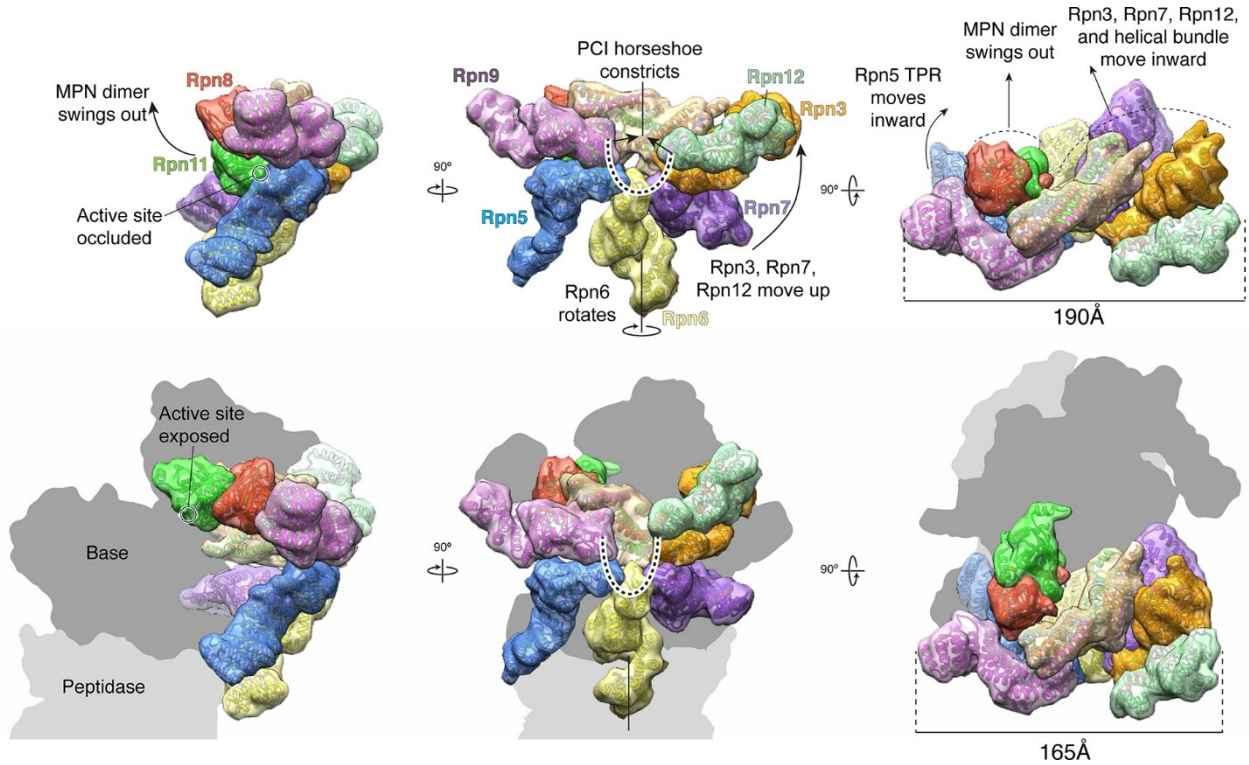

Figure 4.9: Rreorganization of the lid upon incorporation to the 26S holoenzyme
Motions associated with lid incorporation are shown from three orthogonal views. Top panels correspond to the isolated lid, while bottom panels represent the proteasome-incorporated lid. Atomic models of the lid subunits were used to generate semi-transparent Gaussian filtered surfaces for visualization. For clarity, the helical bundle, which moves as a rigid body, is shown as a single surface. Sem1 is not shown. The base and core peptidase components are depicted as shadows to not occlude details of the lid rearrangement. Notable rearrangements include: a 90° rotation of the MPN dimer away from the inhibited conformation, movement of Rpn3, 7, and 12 away from Rpn5, 6, and 9, constriction of the PCI horseshoe, and an overall closure of the lid sub-complex around the regulatory particle.

Rpt6. By comparison, the other half of the PCI horseshoe, consisting of Rpn9, Rpn5 and Rpn6, goes through a much less pronounced conformational change. The N-terminal α-solenoid domain of Rpn9 extends toward the N-terminal coiled coil of Rpt4 and Rpt5, generating the binding site for the ubiquitin receptor Rpn10, and the highly flexible TPR segment of Rpn5 becomes stabilized through contact with the ATPase ring and the core peptidase. The N-terminal α-solenoid domain of Rpn6 also accommodates interactions with the ATPase ring and core peptidase by rotating ~34° around its long axis.

The extensive rearrangements of the PCI-containing subunits upon interaction with base and core may also trigger movements of the helical bundle toward the ATPase ring of the base (Figure 4.9). Because the bundle is connected to the PCI horseshoe through flexible loops, it can move as a single unit, ultimately adopting an orientation in the 26S holoenzyme that is more perpendicular to the hand-shaped arrangement of the PCI subunits. Both in the isolated and incorporated lid, the helical bundle contacts the N-terminal domain of Rpn3, albeit through different interfaces. That the association between these two components is maintained during lid incorporation suggests that movement of the Rpn3/7/12 unit influences the positioning of the bundle (Figure 4.9).

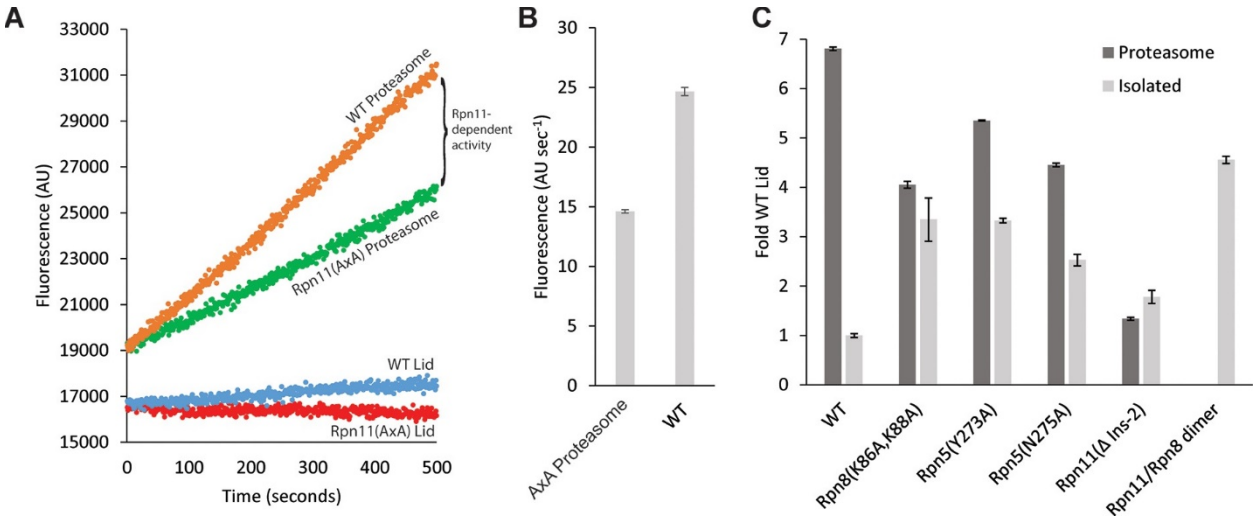

Figure 4 10: Lid incorporation activates Rpn11
(**A**) Rpn11 activation during proteasome incorporation monitored by ubiquitin-AMC hydrolysis. Fluorescence time courses for the isolated WT lid and Rpn11 (AxA) lid are shown in blue and red, respectively. Background DUB activity of proteasomes reconstituted with Rpn11 (AxA) lid is shown in green, and the activity of proteasomes reconstituted with WT lid is shown in orange. The difference between the time courses for proteasomes reconstituted with WT and Rpn11 (AxA) lid corresponds to Rpn11-dependent DUB activity. (**B**) Quantification of the ubiquitin-AMC cleavage activities for WT and Rpn11 (AxA) proteasomes shown in a. (**C**) Normalized Ubiquitin-AMC hydrolysis activity of Rpn11-containing complexes in isolation (grey bars) and background-corrected activity of Rpn11 in proteasomes reconstituted with different lid variants (dark grey bars). Error bars in b and c correspond to 1 standard deviation of the data (n = 3).

The most pronounced conformational rearrangement of the lid involves the Rpn11/Rpn8 MPN-domain heterodimer. Upon lid incorporation, the Rpn11/Rpn8 dimer undergoes a dramatic 90° rotation, moving from its inhibited state in the palm of the isolated lid to a highly extended conformation over the central substrate-translocation channel in the 26S holoenzyme (Figure 4.9). The inhibited conformation of the Rpn11/Rpn8 heterodimer in the isolated lid appears to be metastable, as mutations in either the Rpn5 or Rpn9 contact surfaces lead to release of the dimer. In fact, the extended conformation of the Rpn11/Rpn8 dimer in the proteasome is similar to its conformation in our DUB-activating lid mutants (Figure 4.6). During lid incorporation, it is likely that the conformational changes occurring in the PCI subunits upon their interactions with the core and base distort the Rpn11-Rpn5 and Rpn8-Rpn9 contact sites and release the Rpn11/Rpn8 dimer from its inhibited state. To assess the extent of Rpn11 activation upon lid incorporation, we compared Ub-AMC hydrolysis activity for Rpn11 in the isolated lid versus the assembled 26S proteasome (Figure 4.10). Incorporation of wild-type lid stimulated Rpn11 DUB activity to 150% of the isolated Rpn11/Rpn8 dimer levels. This hyperstimulation of Rpn11 in the proteasome may originate from an alternative Ins-1 loop conformation that is stabilized by the neighboring Rpt4/Rpt5 coiled coil. Rpn11 activity in lid sub-complexes that contain Rpn5 (Y273A), Rpn5 (N275A), or Rpn8 (K86A,K88A) mutations was also stimulated upon proteasome incorporation, although to a lower level than with the wild-type lid (Figure 4.10). None of the mutations are involved in interfaces between subunits in the proteasome holoenzyme, and we speculate that the slightly lower DUB activity of the reconstituted mutant proteasomes originates from an interference with normal lid incorporation due to a

prematurely released MPN dimer. Interestingly, lid sub-complexes where Rpn11 lacked Ins-2 were completely deficient in Rpn11 stimulation upon incorporation into holoenzyme (Figure 4.10), even though Rpn11 activity was unaffected by Ins-2 deletion in the isolated lid (Figure 4.5E). The Ins-2 region of Rpn11 is known to interact with the scaffolding subunit Rpn2 of the base and likely stabilizes the Rpn11/Rpn8 dimer in the extended conformation.

In summary, our structural and functional data suggest that during lid incorporation, the MPN-domain heterodimer loses its stabilizing interactions with Rpn5 and Rpn9, and extends out toward the center of the regulatory particle, leading to Rpn11 activation. This extended conformation enables the Rpn11 Ins-2 loop to interact with Rpn2, which likely aids in positioning the DUB active site above the entrance to the AAA+ ATPase ring for highly regulated deubiquitination of protein substrates during translocation.

4.3 Discussion

The primary function of the lid sub-complex is to house the isopeptidase Rpn11, an enzyme that is central to proteasomal substrate degradation. While earlier structural and biochemical work described the role of the lid scaffold in positioning Rpn11 and facilitating its activity in the context of the assembled proteasome holoenzyme, we illustrate here how interactions of the Rpn11/Rpn8 dimer with other lid subunits block premature DUB activity in the unincorporated lid assembly. Our atomic model of the isolated lid subcomplex showcases the dramatic conformational gymnastics undergone by this important component of the proteasome during incorporation into the regulatory particle and, while the molecular communication involved in promoting this massive reorganization is still an active area of structural and biochemical research, our work here has resolved an important mystery surrounding DUB inhibition and activation during proteasome assembly.

4.4 Materials and methods

4.4.1 Protein purification

Expression and purification of mutant and wild-type recombinant yeast proteasome lid complex was carried out in *E. coli* as described previously, with minor modifications (Lander et al. 2012). Briefly, *E. coli* BL21-star (DE3) cells containing the recombinant lid expression system (pETDuet-1 Rpn5, FLAG-Rpn6, Rpn8, Rpn9, 6xHis-Rpn11], pCOLADuet-1 [Rpn3, Rpn7, Rpn12] and pACYCDuet-1[Sem1, Hsp90) were grown at 37°C in 6 liters of terrific broth (Novagen) supplemented with 150μM $ZnCl_2$. At OD_{600} = 1.0, the temperature was reduced to 18°C and, at OD_{600} = 1.5 lid, expression was induced overnight with 1 mM isopropyl-β-D-thiogalactopyranoside. After centrifugation, cell pellets were re-suspended in lid buffer (60 mM HEPES, pH8.0, 100 mM NaCl, 100 mM KCl, 10% Glycerol, 1 mM DTT) supplemented with protease inhibitors (Aprotinin, Pepstatin, Leupeptin, PMSF), 2mg/ml lysozyme, and bezonase. All purification steps were performed at 4°C. Cells were lysed by sonication and clarified by centrifugation at 16,000g for 30 min. Clarified lysate was

incubated with anti-FLAG M2 resin (Sigma-Aldrich), washed with lid buffer and eluted with lid buffer supplemented with 0.15mg/ml 3x-FLAG peptide. FLAG eluate was concentrated to ~500 µl in a 30,000 MWCO spin concentrator (Amicon) and further purified by size-exclusion chromatography on a Superose 6 column (GE Healthcare) that was pre-equilibrated in lid buffer. Peak fractions were concentrated and stored at -80°C. Purification of core particle, Rpn10, Rpn11/Rpn8 MPN-domain dimer and recombinant base was performed as described previously (Lander et al. 2012; Worden et al. 2014; Beckwith et al. 2013).

4.4.2 Rpn11 activity assays

Rpn11 activity assay. All Ubiquitin-AMC cleavage experiments were performed at 30°C in lid buffer. Because Rpn11's Km for various ubiquitin substrates ranges from ~20 to ~300 µM, we assayed our WT and mutant lid variants at a constant, sub-Km Ubiquitin-AMC concentration. For all lid variants and the Rpn11/Rpn8 MPN-domain dimer, 500 nM enzyme was incubated with 2.5 µM Ubiquitin-AMC (Boston Biochem), and Rpn11-catalyzed ubiquitin cleavage was monitored by the increase in AMC fluorescence (Ex: 360 nm, Em: 435 nm) using a QuantaMaster spectrofluorometer (PTI). The slopes of individual time traces were translated to initial cleavage rates using a standard curve for ubiquitin-AMC (ranging from 0.5–2.5 µM) that had been completely cleaved by the DUB Yuh1. Ubiquitin-AMC cleavage rates for all variants were measured in triplicate except for WT lid, Rpn11/Rpn8 dimer, Rpn5 (H282A, K283A) and Rpn8 (Q115A), where n = 11, n = 6, n = 4, and n = 4, respectively.

Rpn11 activation upon lid incorporation. Proteasomes were reconstituted in vitro with lid as the limiting component by mixing 250 nM lid, 375 nM core particle, 750 nM base and 1 µM Rpn10 in reconstitution buffer (60 mM HEPES, pH7.6, 100 mM NaCl, 100 mM KCl, 10% glycerol, 10 mM $MgCl_2$, 1 mM DTT, 0.5 mM ATP) that contained an ATP-regeneration system (5 mM ATP, 16 mM creatine phosphate, 6 µg/ml creatine phosphokinase). Deubiquitination reactions were initiated by the addition of 2.5 µM ubiquitin-AMC and monitored by the increase in AMC fluorescence (Ex: 360 nm, Em: 435 nm) using a QuantaMaster spectrofluorometer (PTI). A low level background DUB activity co-purified with our yeast core particle. To subtract this background activity, we reconstituted proteasomes as described above, but with a lid variant containing Rpn11 active-site mutations that abolish zinc binding, Rpn11(AxA]). The background DUB activity of Rpn11(AxA) proteasomes was subtracted from the DUB activity of proteasomes reconstituted with WT Rpn11 to get the DUB activity that was specifically contributed by Rpn11. To directly compare the activity of proteasome-incorporated and unincorporated Rpn11, we monitored the ubiquitin-AMC hydrolysis activity of 250 nM lid and Rpn11/Rpn8 MPN-domain dimers in reconstitution buffer containing the ATP regeneration system but with core particle, base, and Rpn10 omitted.

4.4.3 Electron microscopy

Electron microscopy sample preparation. For negative stain analysis, purified lid samples were diluted to ~50 nM in FLAG buffer (50 mM HEPES, pH7.6, 100 mM NaCl,

100 mM KCl) and directly applied to plasma-activated (20 s; 95% Ar, 5% O_2) copper grids for staining with 2% uranyl formate. For analysis by cryoEM, samples were diluted to ~5 μM in FLAG buffer that contained 1.5 mM TCEP (G Biosciences) and 0.05% NP-40 (Sigma). 4 μl of each sample was then applied directly to holey carbon C-flat grids (Protochips, 400 mesh, 1.2 μm holes) that had been plasma-cleaned (Gatan Solarus, 6 s; 95% Ar, 5% O_2) for manual blotting and plunge-freezing in liquid ethane.

All imaging data was collected using automated Leginon imaging software (Suloway et al. 2005). Images of negatively stained samples of wild-type and mutant lid complexes were acquired on a Tecnai Spirit LaB_6 electron microscope operating at 120 keV, with a random defocus range of -0.5 μm to -1.5 μm and an electron dose of 20 $e^-/Å^2$. 331 images were acquired for wild-type lid, 433 images for the Rpn5 (H282A/K283A) double-mutant, 412 images for the Rpn8 (K86A/K88A) double mutant, 181 for the Rpn5 (N275A) mutant, and 204 for the Rpn5 (Y273A) mutant. Images were collected at a nominal magnification of 52,000 X on an F416 CMOS 4K X 4K camera (TVIPS) with a pixel size of 2.05 Å/pixel at the sample level.

Imaging of frozen hydrated samples was performed using a Titan Krios electron microscope operating at 300 keV, with a defocus range of -1.5 μm to -3.5 μm. A Gatan K2 Summit was used for counting individual electron events at a dose rate of 9.9e^-/pixel/s, using an exposure of 7.6 s consisting of 38 frames at 200 ms/frame. This resulted in a total electron dose of 43.8 $e^-/Å^2$, accounting for coincidence loss. A total of 3,432 images of wild-type lid were acquired at a nominal magnification of 22,500X, yielding a pixel size of 0.655 Å/pixel at the sample level when collected in super-resolution mode.

4.4.4 Image processing

Negative stain image processing. All image preprocessing was performed using the Appion image-processing pipeline (Lander et al. 2009). The contrast transfer function (CTF) was estimated using CTFFIND3 (Mindell & Grigorieff 2003). For negative stain data, particles were selected using a difference of gaussians (DoG) picking algorithm (Voss et al. 2009), and only micrographs having an overall CTF confidence of greater than 80% were used for subsequent processing. The phases of the micrograph images were corrected according to the estimated CTF, and the particles were extracted using a box size of 160 pixels, and pixel values were capped at 4.5 sigma above or below the mean. Boxed particles were binned by a factor of 2 for processing. Reference-free 2D class averages of the extracted particles were determined through five rounds of iterative multivariate statistical analysis and multi-reference alignment (Ogura et al. 2003). The results of the 2D analysis were used to remove damaged, aggregated, or falsely selected particles from the dataset used for 3D analysis.

All 3D analysis was performed with RELION v1.31 (Scheres 2012). Using a previously determined reconstruction of the wild type yeast proteasome lid as an initial model (EMD-1993) (Lander et al. 2012), a 3D refinement of 17,680 particles wild-type lid complex provided a reconstruction at 19.6 Å resolution, according to a Fourier Shell Correlation at 0.143 of two independently determined half-maps. This volume was used as the initial model for all 3D analysis of the mutant lid datasets. 3D classification was performed on each of the negative stain mutant lid datasets, and only 3D classes exhibiting well-ordered structural

details were selected and combined within each dataset for 3D refinement. 22,103 particles of the Rpn5 (H282A/K283A) mutant yielded a 25.2 Å reconstruction; 11,185 particles of the Rpn8 (K86A/K88A) mutant yielded a 27.3 Å reconstruction; 25,429 particles of the Rpn5 (N275A) mutant yielded a 23.4 Å reconstruction, and 44,272 particles of the Rpn5 (Y273A) mutant yielded a 21.8 Å reconstruction (Figure 4.6). UCSF Chimera (Goddard et al. 2007) was used to dock the atomic model model of the lid into the density.

Cryo-EM image processing. For cryo-EM image preprocessing, the super-resolution images were binned by a factor of two in reciprocal space, and motion-corrected using MotionCorr (Li et al. 2013). The aligned frames were summed and used for all subsequent processing steps. The CTF was estimated using CTFFIND3 (Mindell & Grigorieff 2003), and only micrographs having a CTF confidence value that was greater than 50% at 4Å resolution were used for further processing (Figure 4.2), resulting in a dataset of 3,365 micrographs. Particles were manually selected from the first 100 images, and the results of reference-free 2D analysis were used as templates for particle selection using FindEM (Roseman 2004). A random subset of 50,000 particles were extracted from the micrographs with a box size of 256 and used for reference-free 2D analysis in order to rapidly assess the quality of particle selection (Figure 4.2). Very few classes corresponding to damaged or aggregated particles were observed; so all particles were used for single particle analysis in RELION.

A total of 254,112 particles were extracted from the micrographs using a box size of 288 pixels, binned by a factor of 4, and classified into 8 3D classes over the course of 22 iterations in RELION. The particles from the 4 classes that showed evidence of conformational and compositional stability were selected from this initial classification, providing a total of 139,561 particles. The x and y coordinates corresponding to these particles were adjusted according to the final translational alignments from the 3D classification, and the centered particle coordinates were used to extract an unbinned particle dataset for 3D refinement in RELION.

3D refinement using the default RELION parameters yielded a 4.4 Å resolution structure after 22 iterations. These aligned particle parameters were used for the RELION 'particle polishing' method. Individual particle motion trajectories were estimated using a running average window of 7 frames and particle translations were limited using a prior with a standard deviation of 1. Particle movements were fit to a linear trajectory using a running average window of 7 frames, with an inter-particle distance contribution value set to 300 pixels. Per-frame B-factors and intercepts were estimated by comparing the reconstructed half-maps from individual frames to the full-frame half maps, and the spatial frequency contribution from each frame weighted according. A new stack of particles was generated from the translationally aligned particles extracted from the weighted frames, which provided a reconstruction at 4.1 Å resolution.

Due to the possibility that the flexible N-terminal domains of the PCI subunits were negatively influencing the particle alignment, a soft-edged 3D mask encompassing the PCI-domains, the helical bundle, and the MPN domains was generated (blue mask shown in Figure 4.2) and used for 3D classification of the particles into 3 classes. This 3D classification was performed using the alignments from the 3D refinement, without further alignment of particles. One of the 3D classes resulting from this analysis clearly exhibited

higher resolution details than the other two, and the 109,396 particles contained in this class were further refined (in the absence of a mask) to achieve a 3.6 Å structure. The same soft-edged 3D mask that was used for the previous 3D classification was then used for continued 3D refinement, which improved the structural details of the region contained within this mask, and increased the resolution to 3.5 Å resolution.

4.4.5 Modeling

Modeling and visualization of the lid was performed in COOT (Emsley & Cowtan 2004) using mostly the cryo-EM map that had been generated using a soft mask encompassing the PCI domains and the C-terminal helical bundle (deposited as EMD-6479), as this is the highest resolved region, and cross-validated using the unmasked map. Available structures and homology models generated using Modeller v9.15 (Eswar et al. 2007) were initially fit into the unmasked cryo-EM map using Chimera (Goddard et al. 2007). These included: 1) the crystal structure of *Drosophila melanogaster* Rpn6 (residues 50–390) homolog (PDB ID: 3TXN) (Pathare et al. 2012); 2) the crystal structure of the *Saccharomyces cerevisiae* Rpn11-Rpn8 heterodimer (residues 24–220 and 10–280, respectively; PDB ID: 4O8X) (Worden et al. 2014); 3) the NMR structures of the N-terminal (residues 4–140 (PDB ID: 2MQW) and C-terminal (residues 184–353 (PDB ID: 2MRI)) domains of *Saccharomyces cerevisiae* Rpn9 (Hu et al. 2015); and 4) the N-terminal domain of *Schizosaccharomyces pombe* Rpn12 homolog (residues 6–200, PDB ID: 4B0Z) (Boehringer et al. 2012). The most N-terminal helices of Rpn5 and Rpn6 were not modeled due to the limited resolution of these regions. Placement of the N-terminal helices of Rpn3 was possible, however the absolute sequence register could not be assigned and these helices were modeled as polyalanine.

Following each round of real space refinement in Phenix v1.10 (Adams et al. 2010), 100 models were generated in Rosetta (DiMaio et al. 2015), clustered, and scored. The top scoring structures were then used for the next round of manual model building and an aggregate model was used for refinement in Phenix. For the final round of refinement, the SHAKE protocol in Phenix was used to displace all atoms of the top 5 scoring models by 0.5 Å before refinement against one of the unmasked half-maps. An ensemble of these 5 models have been deposited in the PDB under ID: 3JCK.

4.4.6 Visualizing rearrangements involved in lid incorporation into the 26S

To visualize conformational changes undergone by the lid complex upon incorporation into the 26S proteasome, we first rigid-body fit individual components of the atomic model of our isolated lid (6 PCI domains, 6 N-terminal extensions, the MPN heterodimer, and the helical bundle) onto the pseudo-atomic model of the engaged lid (PDB-ID: 4CR2) (Unverdorben et al. 2014) using the 'MatchMaker' tool in Chimera. These overlaid models were then docked into the EM density of the 26S holoenzyme in the S1 state (Unverdorben et al. 2014). Overall, the secondary structure organization of the atomic models matched with high fidelity, although the register of the C-terminal helices of Rpn11 and the N-terminal helices of Rpn9 of the incorporated lid model were modified to correspond to the isolated lid model. The domain movements were visualized using the 'morph conformations' tool in

UCSF Chimera. The motion of Rpn6 was evaluated using the software DynDom (Hayward & Berendsen 1998).

5. References

Adams, P.D. et al., 2010. PHENIX: A comprehensive Python-based system for macromolecular structure solution. *Acta Crystallographica Section D: Biological Crystallography*, 66(2), pp.213–221.

Arif, S. et al., 2016. Short Article MINDY-1 Is a Member of an Evolutionarily Conserved and Structurally Distinct New Family of Deubiquitinating Enzymes Short Article MINDY-1 Is a Member of an Evolutionarily Conserved and Structurally Distinct New Family of Deubiquitinating Enz. *Molecular Cell*, pp.1–10.

Asquith, R., Otterburn, M. & Sinclair, W., 1974. Isopeptide crosslinks—their occurrence and importance in protein structure. *Angewandte Chemie (International ed. in English)*, 13(8), pp.514–520.

Aufderheide, A. et al., 2015. Structural characterization of the interaction of Ubp6 with the 26S proteasome. *Proceedings of the National Academy of Sciences of the United States of America*, 112(28), pp.8626–31.

Bashore, C. et al., 2015. Ubp6 deubiquitinase controls conformational dynamics and substrate degradation of the 26S proteasome. *Nature structural & molecular biology*, 22(August), pp.1–10.

Beck, F. et al., 2012. Near-atomic resolution structural model of the yeast 26S proteasome. *Proceedings of the National Academy of Sciences of the United States of America*, 109(37), pp.14870–5.

Beckwith, R. et al., 2013. Reconstitution of the 26S proteasome reveals functional asymmetries in its AAA+ unfoldase. *Nature structural & molecular biology*, 20(10), pp.1164–72.

Boehringer, J. et al., 2012. Structural and functional characterization of Rpn12 identifies residues required for Rpn10 proteasome incorporation. *The Biochemical journal*, 448(1), pp.55–65.

Bohn, S. et al., 2013. Localization of the regulatory particle subunit Sem1 in the 26S proteasome. *Biochemical and Biophysical Research Communications*, 435(2), pp.250–254.

Ciechanover, A. et al., 1982. "Covalent affinity" purification of ubiquitin-activating enzyme. *The Journal of biological chemistry*, 257(5), pp.2537–42.

Cooper, E.M. et al., 2009. K63-specific deubiquitination by two JAMM/MPN+ complexes: BRISC-associated Brcc36 and proteasomal Poh1. *Embo J*, 28(6), pp.621–631.

Cooper, E.M., Boeke, J.D. & Cohen, R.E., 2010. Specificity of the BRISC deubiquitinating enzyme is not due to selective binding to Lys63-linked polyubiquitin. *Journal of Biological Chemistry*, 285(14), pp.10344–10352.

Dambacher, C.M. et al., 2016. Atomic structure of the 26S proteasome lid reveals the mechanism of deubiquitinase inhibition. *eLife*, 5(January), pp.1–17.

Davies, C.W. et al., 2011. Structural and thermodynamic comparison of the catalytic domain of AMSH and AMSH-LP: Nearly identical fold but different stability. *Journal of Molecular Biology*, 413(2), pp.416–429.

Dikic, I., Wakatsuki, S. & Walters, K.J., 2009. Ubiquitin-binding domains - from structures to functions. *Nature reviews. Molecular cell biology*, 10(10), pp.659–671.

DiMaio, F. et al., 2015. Atomic-accuracy models from 4.5-Å cryo-electron microscopy data with density-guided iterative local refinement. *Nature methods*, 12(4), pp.361–5.

Available at: http://www.ncbi.nlm.nih.gov/pubmed/25707030.
Dong, K.C. et al., 2011. Preparation of distinct ubiquitin chain reagents of high purity and yield. *Structure*, 19(8), pp.1053–1063.
Echalier, A. et al., 2013. Insights into the regulation of the human COP9 signalosome catalytic subunit, CSN5/Jab1. *Proceedings of the National Academy of Sciences of the United States of America*, 110(4), pp.1273–8.
Emsley, P. & Cowtan, K., 2004. Coot: Model-building tools for molecular graphics. *Acta Crystallographica Section D: Biological Crystallography*, 60(12 I), pp.2126–2132.
Erales, J. et al., 2012. Functional Asymmetries of Proteasome Translocase Pore. *Journal of Biological Chemistry*, 287(22), pp.18535–18543.
Estrin, E. et al., 2013. Formation of an intricate helical bundle dictates the assembly of the 26S proteasome Lid. *Structure*, 21(9), pp.1624–1635.
Eswar, N. et al., 2007. *Comparative protein structure modeling using MODELLER.*
Finley, D., 2009. Recognition and processing of ubiquitin-protein conjugates by the proteasome. *Annual review of biochemistry*, 78, pp.477–513.
Fishbain, S. et al., 2015. Sequence composition of disordered regions fine-tunes protein half-life. *Nature Structural & Molecular Biology*, 22(3), pp.214–221.
des Georges, A. et al., 2015. Structure of mammalian eIF3 in the context of the 43S preinitiation complex. *Nature*, 525(7570), pp.491–5.
Glickman, M.H. et al., 1998. The regulatory particle of the Saccharomyces cerevisiae proteasome. *Molecular and cellular biology*, 18(6), pp.3149–62.
Glickman, M.H. & Ciechanover, A., 2002. The Ubiquitin-Proteasome Proteolytic Pathway: Destruction for the Sake of Construction. *Physiological Reviews*, 82(2), pp.373–428.
Goddard, T.D., Huang, C.C. & Ferrin, T.E., 2007. Visualizing density maps with UCSF Chimera. *Journal of Structural Biology*, 157(1), pp.281–287.
Groll, M. et al., 2000. A gated channel into the proteasome core particle. *Nature structural biology*, 7(11), pp.1062–7.
Groll, M. et al., 1997. Structure of 20S proteasome from yeast at 2.4 A resolution. *Nature*, 386(6624), pp.463–471.
Hayward, S. & Berendsen, H.J.C., 1998. Systematic analysis of domain motions in proteins from conformational change: New results on citrate synthase and T4 lysozyme. *Proteins: Structure, Function and Genetics*, 30(2), pp.144–154.
Hershko, A. et al., 1980. Proposed role of ATP in protein breakdown: conjugation of protein with multiple chains of the polypeptide of ATP-dependent proteolysis. *Proceedings of the National Academy of Sciences of the United States of America*, 77(4), pp.1783–6.
Hicke, L., 2001. Protein regulation by monoubiquitin. *Nature reviews. Molecular cell biology*, 2(3), pp.195–201.
Hofmann, K. & Bucher, P., 1998. The PCI domain: A common theme in three multiprotein complexes. *Trends in Biochemical Sciences*, 23(6), pp.204–205.
Hu, Y. et al., 2015. Solution structure of yeast Rpn9: Insights into proteasome lid assembly. *Journal of Biological Chemistry*, 290(11), pp.6878–6889.
Husnjak, K. et al., 2008. Proteasome subunit Rpn13 is a novel ubiquitin receptor. *Nature*, 453(7194), pp.481–8.
Ikeda, F., Crosetto, N. & Dikic, I., 2010. What determines the specificity and outcomes of Ubiquitin signaling? *Cell*, 143(5), pp.677–681.
Inobe, T. et al., 2011. Defining the geometry of the two-component proteasome degron.

Nature Chemical Biology, 7(3), pp.161–167.
Kabsch, W., 2010. Xds. *Acta Crystallographica Section D: Biological Crystallography*, 66(2), pp.125–132.
Komander, D., Clague, M.J. & Urbé, S., 2009. Breaking the chains: structure and function of the deubiquitinases. *Nature reviews. Molecular cell biology*, 10(8), pp.550–563.
Komander, D. & Rape, M., 2012. The Ubiquitin Code. *Annual Review of Biochemistry*, 81(1), pp.203–229.
Lander, G.C. et al., 2009. Appion: An integrated, database-driven pipeline to facilitate EM image processing. *Journal of Structural Biology*, 166(1), pp.95–102.
Lander, G.C. et al., 2012. Complete subunit architecture of the proteasome regulatory particle. *Nature*, 6(7384), pp.6–13.
Li, X. et al., 2013. Electron counting and beam-induced motion correction enable near-atomic-resolution single-particle cryo-EM. *Nature methods*, 10(6), pp.584–90.
Li, Y., Tomko, R.J. & Hochstrasser, M., 2015. Proteasomes: Isolation and activity assays. *Current Protocols in Cell Biology*, 2015(June), pp.3.43.1–3.43.20.
Lingaraju, G.M. et al., 2014. Crystal structure of the human COP9 signalosome. *Nature*, 512(7513), pp.161–5.
Lupas, A., Van Dyke, M. & Stock, J., 1991. Predicting coiled coils from protein sequences. *Science*, 252(5009), pp.1162–1164.
Martin, A., Baker, T.A. & Sauer, R.T., 2008. Pore loops of the AAA+ ClpX machine grip substrates to drive translocation and unfolding. *Nature structural & molecular biology*, 15(11), pp.1147–1151.
Matyskiela, M.E., Lander, G.C. & Martin, A., 2013. Conformational switching of the 26S proteasome enables substrate degradation. *Nature structural & molecular biology*, 20(7), pp.781–8..
Matyskiela, M.E. & Martin, A., 2013. Design principles of a universal protein degradation machine. *Journal of Molecular Biology*, 425(2), pp.199–213.
Mindell, J.A. & Grigorieff, N., 2003. Accurate determination of local defocus and specimen tilt in electron microscopy. *Journal of Structural Biology*, 142(3), pp.334–347.
Ogura, T., Iwasaki, K. & Sato, C., 2003. Topology representing network enables highly accurate classification of protein images taken by cryo electron-microscope without masking. *Journal of Structural Biology*, 143(3), pp.185–200.
Pathare, G.R. et al., 2014. Crystal structure of the proteasomal deubiquitylation module Rpn8-Rpn11. *Proceedings of the National Academy of Sciences of the United States of America*, 111(8), pp.2984–9.
Pathare, G.R. et al., 2012. The proteasomal subunit Rpn6 is a molecular clamp holding the core and regulatory subcomplexes together. *Proceedings of the National Academy of Sciences*, 109(1), pp.149–154.
Peth, A., Nathan, J.A. & Goldberg, A.L., 2013. The ATP costs and time required to degrade ubiquitinated proteins by the 26 S proteasome. *Journal of Biological Chemistry*, 288(40), pp.29215–29222.
Pickart, C.M., 2001. Mechanisms nderlying biquitination. *Annual Review of Biochemistry*, 70, pp.503–533.
Pickart, C.M. & Raasi, S., 2005. Controlled Synthesis of Polyubiquitin Chains. In *Methods in Enzymology*. pp. 21–36.
Prakash, S. et al., 2004. An unstructured initiation site is required for efficient proteasome-

mediated degradation. *Nature structural & molecular biology*, 11(9), pp.830–837.
Rabl, J. et al., 2008. Mechanism of Gate Opening in the 20S Proteasome by the Proteasomal ATPases. *Molecular Cell*, 30(3), pp.360–368.
Roseman, A.M., 2004. FindEM - A fast, efficient program for automatic selection of particles from electron micrographs. *Journal of Structural Biology*, 145(1-2), pp.91–99.
Ross, C.A. & Poirier, M.A., 2004. Protein aggregation and neurodegenerative disease. *Nature Medicine*, 10(July), pp.S10–S17.
Sadowski, M. et al., 2012. Protein monoubiquitination and polyubiquitination generate structural diversity to control distinct biological processes. *IUBMB Life*, 64(2), pp.136–142.
Saeki, Y. et al., 2009. Lysine 63-linked polyubiquitin chain may serve as a targeting signal for the 26S proteasome. *The EMBO journal*, 28(4), pp.359–71.
Saeki, Y. et al., 2012. Ubiquitin Family Modifiers and the Proteasome. *Methods in Molecular Biology*, 832, pp.423–432.
Sanches, M. et al., 2007. The Crystal Structure of the Human Mov34 MPN Domain Reveals a Metal-free Dimer. *Journal of Molecular Biology*, 370(5), pp.846–855.
Sato, Y. et al., 2008. Structural basis for specific cleavage of Lys[thinsp]63-linked polyubiquitin chains. *Nature*, 455(7211), pp.358–362.
Scheres, S.H.W., 2012. RELION: Implementation of a Bayesian approach to cryo-EM structure determination. *Journal of Structural Biology*, 180(3), pp.519–530.
Schreiner, P. et al., 2008. Ubiquitin docking at the proteasome through a novel pleckstrin-homology domain interaction. *Nature*, 453(7194), pp.548–552.
Shi, Y. et al., 2016. Rpn1 provides adjacent receptor sites for substrate binding and deubiquitination by the proteasome. *Science*, 351(6275), p.aad9421.
Shrestha, R.K. et al., 2014. Deubiquitinases from Cocrystal Structures of the Enzyme with the.
Smith, D.M. et al., 2007. Docking of the Proteasomal ATPases' Carboxyl Termini in the 20S Proteasome's α Ring Opens the Gate for Substrate Entry. *Molecular Cell*, 27(5), pp.731–744.
Sobhian, B. et al., 2007. RAP80 Targets BRCA1 to Specific Ubiquitin Structures at DNA Damage Sites. *Science*, 316(5828), pp.1198–1202.
Suloway, C. et al., 2005. Automated molecular microscopy: The new Leginon system. *Journal of Structural Biology*, 151(1), pp.41–60.
Thrower, J.S. et al., 2000. Recognition of the polyubiquitin proteolytic signal. *The EMBO journal*, 19(1), pp.94–102.
Tomko, R.J. et al., 2015. A Single α Helix Drives Extensive Remodeling of the Proteasome Lid and Completion of Regulatory Particle Assembly. *Cell*, 163(2), pp.432–444.
Tomko, R.J. & Hochstrasser, M., 2011. Incorporation of the Rpn12 Subunit Couples Completion of Proteasome Regulatory Particle Lid Assembly to Lid-Base Joining. *Molecular Cell*, 44(6), pp.907–917.
Unverdorben, P. et al., 2014. Deep classification of a large cryo-EM dataset defines the conformational landscape of the 26S proteasome. *Proceedings of the National Academy of Sciences*, 111(15), pp.5544–5549.
Verma, R., 2002. Role of Rpn11 Metalloprotease in Deubiquitination and Degradation by the 26 S Proteasome. , 611(2002).
Voss, N.R. et al., 2009. DoG Picker and TiltPicker: Software tools to facilitate particle selection in single particle electron microscopy. *Journal of Structural Biology*, 166(2), pp.205–213.

Wang, B. et al., 2007. Abraxas and RAP80 Form a BRCA1 Protein Complex Required for the DNA Damage Response. *Science*, 316(5828), pp.1194–1198.
Wang, Q., Young, P. & Walters, K.J., 2005. Structure of S5a bound to monoubiquitin provides a model for polyubiquitin recognition. *Journal of Molecular Biology*, 348(3), pp.727–739.
Wertz, I.E. et al., 2004. De-ubiquitination and ubiquitin ligase domains of A20 downregulate NF-kB signalling. *Nature*, 430(7000), pp.694–699.
Worden, E.J., Padovani, C. & Martin, A., 2014. Structure of the Rpn11-Rpn8 dimer reveals mechanisms of substrate deubiquitination during proteasomal degradation. *Nature structural & molecular biology*, 21(3), pp.220–7.
Xu, P. et al., 2009. Quantitative Proteomics Reveals the Function of Unconventional Ubiquitin Chains in Proteasomal Degradation. *Cell*, 137(1), pp.133–145.
Yao, T. & Cohen, R.E., 2002. A cryptic protease couples deubiquitination and degradation by the proteasome. *Nature*, 419(6905), pp.403–407.
Ye, Y. et al., 2012. Ubiquitin chain conformation regulates recognition and activity of interacting proteins. *Nature*, 492(7428), pp.266–70.
Zeqiraj, E. et al., 2015. Higher-Order Assembly of BRCC36–KIAA0157 Is Required for DUB Activity and Biological Function. *Molecular Cell*, pp.970–983.
Zhang, F., Wu, Z., et al., 2009. Mechanism of Substrate Unfolding and Translocation by the Regulatory Particle of the Proteasome from Methanocaldococcus jannaschii. *Molecular Cell*, 34(4), pp.485–496.
Zhang, F., Zhang, F., et al., 2009. Structural insights into the regulatory particle of the proteasome from Methanocaldococcus jannaschii. *Molecular cell*, 34(4), pp.473–84.